Thin-film Bulk Acoustic Resonators on Integrated Circuits for Physical Sensing Applications

Matthew Leigh Johnston

Submitted in partial fulfillment of the

requirements for the degree

of Doctor of Philosophy

in the Graduate School of Arts and Sciences

COLUMBIA UNIVERSITY

2012

Abstract

Thin-film Bulk Acoustic Resonators on Integrated Circuits for Physical Sensing Applications

Matthew Leigh Johnston

Merging chemical and biomolecular sensors with silicon integrated circuits has the potential to push complex electronics into a low-cost, portable platform, greatly simplifying system-level instrumentation and extending the reach and functionality of point of use technologies. One such class of sensor, the thin-film bulk acoustic resonator (FBAR), has a micron-scale size and low gigahertz frequency range that is ideally matched with modern complementary metal-oxide-semiconductor (CMOS) technologies. An FBAR sensor can enable label-free detection of analytes in real time, and CMOS integration can overcome the measurement complexity and equipment cost normally required for detection with acoustic resonators.

This thesis describes a body of work conducted to integrate an array of FBAR sensors with an active CMOS substrate. A monolithic fabrication method is developed, which allows for FBAR devices to be built directly on the top surface of the CMOS chip through post-processing. A custom substrate is designed and fabricated in 0.18 μm CMOS to support oscillation and frequency measurement for each sensor site in a 6×4 array. The fabrication of 0.8-1.5 GHz FBAR devices is validated for both off-chip and on-chip devices, and the integrated system is characterized for sensitivity and limit of detection. On-chip, parallel measurement of multiple sensors in real time is demonstrated for a quantitative vapor sensing application, and the limit of detection is below 50 ppm. This sensor platform could be used for a broad scope of label-free detection applications in chemistry, biology, and medicine, and it demonstrates potential for enabling a low-cost, point of use instrument.

Contents

List of Figures

List of Tables

Acknowledgments

Many people have made this work possible. Foremost among these is my adviser, Professor Kenneth Shepard, who brought me to Columbia, and who has been a boundless source of technical, professional, and personal guidance. Ken is an outstanding teacher and engineer, and his infectious enthusiasm, diverse curiosity, and far-reaching creativity have been tremendous assets. Ken's support and encouragement also enabled both my entrepreneurial hiatus from graduate school and my return to academia. I am immensely grateful for his countless contributions to this work and to my own development.

I would also like to thank Professor Ioannis "John" Kymissis, with whom I've worked closely and regularly over the past several years, and who also served on my thesis committee. John has been a tremendous well of experience from which to draw. He has taught me a lot about science, technology, and life, and I am grateful for our frequent and wide-ranging discussions. We never had a meeting that ended on time.

I have had the privilege to work with many talented people on this effort, and in particular I would like to thank Hassan Edrees, Dan Fainstein, Brian Tull, Ping Gong, Michael Khalil, Anusha Dachepally, and Srikanth Viswanathan for their contributions.

Columbia University has been an extraordinary source of friends and colleagues. I would like to thank Simeon Realov, Ryan Field, and Neal Chapman for their close friendship and countless hours of technical and non-technical discussions over the years. Ryan, along with Erik Young, also graciously helped edit this dissertation. I owe special thanks to my cohort members in the Bioelectronic Systems Lab, including Sebastian Sorgenfrei, Inanc Meric, and Omar Ahmad, who taught me a lot and continue to be great friends. I would

also like to thank Vincent Lee, Bill McLaughlin, Jared Roseman, Jacob Rosenstein, Noah Sturcken, Michael Lekas, Cory Dean, Siddarth Ramakrishnan, and Paul Pan for their help, support, and friendship.

I would like to thank my thesis committee members for their time, comments and contributions; Professors Wen Wang, Samuel Sia, and James Hone.

I would like to thank Thucydides "Duke" Xanthopoulos and Scott Meninger, with whom I worked closely during my internship at Cavium Networks. They gave me a wealth of design experience in a very short amount of time, and they made my few months in Boston both rewarding and memorable.

I would like to thank Professor Axel Scherer at Caltech and David Vallancourt at Columbia for providing key guidance at crucial moments along the way.

During my time away from Columbia, I was fortunate to work with many accomplished individuals. I would like to specifically acknowledge Xing Yang, Arkadiy Silbergleit, and George Maltezos. I learned a great deal about business, technology, biology, and life from Xing and Ark, and Xing has continued to be an invaluable source of support and advice. George and I worked together from California to New York to Thailand, and his singular drive and enthusiasm have been inspiring. We have had a long and productive partnership and friendship.

I also thank those who have supported me through the years and made sure that I got out of the lab, at least once in awhile:

My longtime friend and co-conspirator, David McKinney.

My fellow travelers and friends Peter Samuelson, Jared Gabor, and Kevin Duncklee.

My family, who have been vocal and steadfast in their support.

And, finally, Manisha Lotlikar, for her daily and determined support, care, distraction, and companionship, despite the 3,880 miles between us.

Chapter 1

Introduction

> *"You've got to listen to the silicon, because it's always trying to tell you what it can do."* - Carver Mead, *Los Angeles Times*, May 21, 1989

It is hardly an exaggeration to say that silicon integrated circuits have defined our era. In the last 50 years, integrated circuit technology has scaled exponentially to enable mass-production of incredibly powerful and low-cost devices; advances in complementary metal-oxide-semiconductor (CMOS) technology have allowed transistor density to double every year since 1959 [1]. This has fueled an unparalleled industrial growth driven by low-cost, high-density computation and imaging. In the next 50 years, we may see this technology infrastructure applied to a broad scope of emerging, non-computational applications in chemistry, biology, and medicine.

Integration of CMOS circuits with chemical and biomolecular sensors has the potential to push complex electronics into a low-cost, portable platform, greatly simplifying system-level instrumentation and extending the reach and functionality of point of use technologies. This has most recently been demonstrated by the commercialization of disposable CMOS cartridges for high-throughput genetic sequencing [2].

A multitude of sensing mechanisms have already been developed that are the right size, signal level, and frequency range for interfacing with modern integrated circuit technologies. This dissertation describes a body of work undertaken to advance one of these

technologies, acoustic resonators, to a CMOS-integrated platform for the demonstration of this very real potential.

The thin-film bulk acoustic resonator (FBAR) is made from a thin layer of piezoelectric material, sandwiched between two electrodes. The devices are nominally 100 μm on a side and 1-2 μm thick, and they exhibit a fundamental resonance frequency in the low gigahertz range. When a layer of material adsorbs or is bound to the top surface of this structure, the resonant frequency shifts down, slightly. Through integration with CMOS electronics, an array of monolithic sensors is constructed that are measured continuously and in parallel without the need for complex, external instrumentation. This functionality is experimentally demonstrated through the detection and quantification of organic vapor concentration.

The FBAR-CMOS sensor platform enables sensitive, real-time, label-free detection in a small and portable form factor. It is broadly applicable to applications in which molecules can be selectively bound. This has significant potential utility in the measurement of proteins, nucleic acids, and contaminants in air and water.

1.1 Thesis outline

Chapter 2 compares traditional and emerging detection techniques, and it reviews the current state of the art for label-free and real-time detection methods. A particular emphasis is given to acoustic resonators, and the interface between an acoustic resonator and a CMOS integrated circuit platform is described. The remaining bulk of this dissertation is divided into three main sections. These describe the resonant sensor, the CMOS platform, and an experimental demonstration of the integrated system.

Chapter 3 provides the background necessary to understand the design and function of acoustic resonator devices, and it describes the design, fabrication, and characterization of zinc oxide FBAR structures. These are built on glass and silicon substrates and exhibit electrical and mechanical resonances between 800 MHz and 1.5 GHz.

Chapter 4 reports the circuit and system requirements for the implementation of

CMOS oscillators built around monolithic FBAR devices. The design, implementation, and characterization of an integrated circuit design for support and measurement of an FBAR oscillator array is presented. This chip is fabricated in a 0.18 μm CMOS technology, and it enables a 6×4 array of on-chip oscillators and frequency counters.

Chapter 5 describes a series of experiments in which the integrated FBAR-CMOS sensor platform is used for the detection and quantification of volatile organic compounds. A thin polymer layer is employed as a semi-selective gas absorbing substrate, and a method is developed for the application of such layers to individual sensors in a dense array. Frequency shift is measured in real time in response to vapor exposure. Concentration series data are presented, and the limit of detection for the sensor system is analyzed.

Chapter 6 summarizes the original contributions this body of work has made to the fields of acoustic resonators, CMOS-integrated sensors, and portable detection electronics.

Chapter 2

Background and review

2.1 Introduction

Traditional chemical and biological sensing technologies can be broadly divided into laboratory and point of use techniques. The former comprise quantitative, sensitive, and typically complex methods that form the standard against which new technologies are measured. The latter prioritize cost and portability over performance and functionality to address a limited set of measurement applications. A broad range of new technologies aim to bridge this gap, bringing increased sensitivity and functionality to portable, low-cost applications.

This chapter introduces both traditional and emerging detection techniques, with a special emphasis on the advantages of real-time and label-free detection methods for point of use applications. One of these methods, acoustic resonators, is reviewed in detail for application to chemical and biological applications. This class of sensors can be enabled for portable applications by interfacing with silicon integrated circuits. The current state of the art for this combination is reviewed, and a new platform for portable, sensitive detection is proposed. The development and demonstration of this platform will be described in Chapters 3-5.

2.2 Traditional detection methods

A consistent driver of cost and complexity in chemical and biological detection is the use of labels for quantitative measurement. Alternatively, most laboratory systems for label-free quantification, such as mass spectrometry, require even greater capital investment and user training. This section uses two application examples to describe current methods for both laboratory-based and point of use detection.

2.2.1 Biomolecular detection

Laboratory methods

An immunoassay is a biomolecular technique for identifying antibodies or antigens in an unknown sample mixture. Immunoassays are employed in medicine for many diagnostic purposes, including the identification of viral or bacterial infection, autoimmune condition, acute cardiac illness, pregnancy, and blood type [3]. As a laboratory method, this assay is employed in many variants of an enzyme-linked immunosorbent assay (ELISA), the basic steps of which are illustrated in Figure 2.1 for indirect antigen detection.

A generic indirect ELISA protocol proceeds as follows: A prepared test sample is incubated in a plastic well plate, where antigens bind non-specifically to the surface. A wash step removes unbound sample mixture, and an antigen-specific detection antibody is incubated in the wells. The antibody binds to present antigen, and a wash step removes unbound antibody. For read-out, a secondary antibody that has been conjugated to an enzyme tag is incubated in the test well. The secondary antibody binds to collocated detection antibody, and unbound secondary antibody is removed. Finally, a detection substrate solution is added to the well. The enzyme label catalyzes a color-changing reaction, with color density proportional to secondary antibody concentration.

The ELISA process is very robust in the hands of a trained practitioner, and a large well plate allows for testing several samples or several antigens in parallel. As can be seen in Figure 2.1, however, the process has many steps, each of which introduces error and loss.

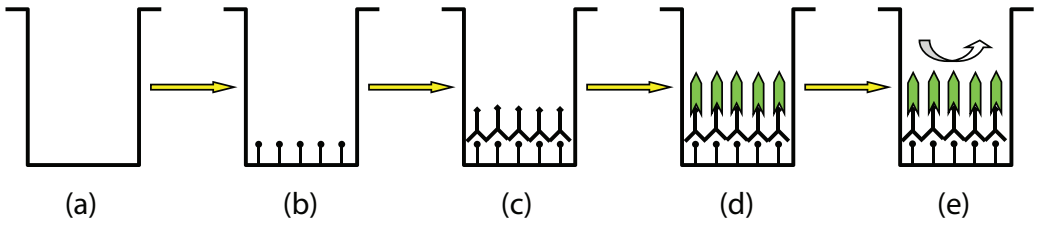

Figure 2.1: Illustration of the steps required for a basic enzyme-linked immunosorbent assay (ELISA). An empty well (a) is incubated with a patient sample, and antigens bind to the surface (b). After washing, detection antibodies are incubated and bind (c), followed by another wash and the introduction of enzyme-linked secondary antibodies (d). The linked enzyme catalyzes a color change in a substrate solution (e) that can be read by eye or quantified with an optical scanner.

Additionally, the color change reaction must be quantified with an optical scanner, which is relegated to a bench-top instrument by the size and weight required for illumination and sensitive, uniform detection. The ELISA process can also be ported to a robotic test setup, which mitigates experimenter error but adds significant cost and complexity to the technique [4].

Point of use methods

For point of use applications, the canonical immunoassay is the lateral flow assay (LFA). This method is illustrated in Figure 2.2. A strip of nitrocellulose is functionalized with labeled detection antibodies (conjugate pad) and capture antibodies (detection line) and lyophilized. At the time of use, a patient sample in buffer is introduced at the sample pad, and it wicks through the membrane. Detection antibodies are picked up by the flow and bind to present antigen. Further down the strip, a capture antibody binds the same antigen-antibody conjugate at a different epitope, and unbound labeled antibody continues through the membrane. The label catalyzes a color-change reaction at the capture site, and the test can be read by eye or quantified with an optical reader.

The LFA device has found widespread use in the testing of pregnancy, influenza, and HIV infection, along with dozens of other diagnostic applications [3]. It is cheap, sensitive, disposable, straightforward to use, and for non-quantitative applications requires

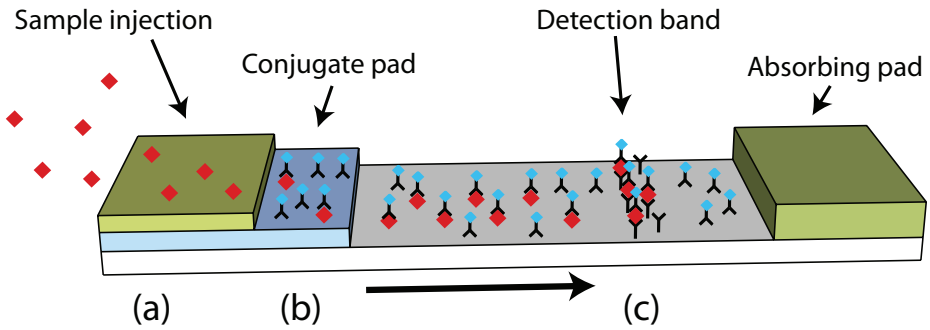

Figure 2.2: Illustration of the lateral flow assay device. Sample is introduce at the absorbent pad (a) and flows in the direction of the arrow. Antigen in the sample binds to labeled antibodies in the conjugate pad (b), and bound and unbound analytes flow through the nitrocellulose membrane. Immobilized antibodies at the detection band (c) capture analyte-antibody conjugates, and a local color change is catalyzed. Unbound molecules continue to flow toward the absorbing pad.

no additional hardware. The limitations of LFA lie in its inability to test for more than one or two analytes in parallel, its requirement of additional optical hardware for quantification of the bound labels, and the limit of its application to end-point testing.

2.2.2 Air quality testing

Both indoor and outdoor air contain quantifiable concentrations of hazardous volatile organic compounds whose emission stems from natural and anthropogenic sources [5]. There exist both laboratory-based and point of use testing methods for the measurement of such compounds in air samples, and similar techniques are applied for detection of aqueous organic compounds.

Laboratory methods

For laboratory testing, samples are collected in the field using glass tubes containing charcoal or similar media, which adsorb ambient compounds for transport to a testing facility [6]. After relocation, the compounds are desorbed from the sample tube, and a gas chromatograph is used for identification and quantification. This technique mixes the volatilized compound with a carrier gas and passes it through a column containing media or liquid

phase coating [7]. Compounds will move through the column at a rate depending on their relative affinities for the material in the column, and the time at which each emerges can be used for identification. Quantification is accomplished with several detection methods, the most accurate (and complex) of which is mass spectrometry. A more detailed analysis of this method is found in [7]. The chromatograph and mass spectrometer require extensive capital investment and highly trained operators, and the results produced by each are not always comparable across laboratories [5]. Additionally, these methods are not portable and cannot be employed for the continuous measurement of ambient air.

Point of use methods

For point of use applications, many sensor technologies have been commercialized for portable gas and vapor detection, including galvanic, catalytic, infrared, and and electrochemical mechanisms [8]. These devices can detect gas concentrations below one part per million (ppm) for organic compounds, toxic gases, and combustible vapors. However, these devices are severely limited in detection specificity, and they are applicable only to the quantification of categories of gases or the confirmation or exclusion of a particular contaminant.

2.2.3 Toward improved point of use detection

Label-free detection methods remove multiple intermediaries from a testing process. These can include chemical labels, optical illumination sources, optical sensors, and many other indirect paths that add complexity, loss, and noise to a measurement. For medical applications, optical systems and complex sample preparation have continued to serve as barriers to the adoption of modern molecular diagnostic technologies around the world.

Adaptation of a new, quantitative label-free sensing technology to a portable platform has the potential to overcome the limitations of current LFA tests and bring the performance of a laboratory ELISA to a low-cost, easy to use, disposable format. Real-time and label-free detection also enables continuous sample interrogation. This is especially

useful for monitoring air and water for contaminants, and it has significant potential for continuous monitoring in medical, industrial, and agricultural applications.

2.3 Label-free and real-time detection

Many emerging technologies that provide label-free detection have the potential to enable robust, quantitative measurement without capital-intensive equipment, extensive sample preparation, or highly trained operators. This section will review several prominent label-free detection techniques for chemical and biological analytes, including acoustic wave resonators, cantilevers, electrochemical methods, and surface plasmon resonance.

2.3.1 Acoustic wave resonators

Acoustic wave resonators have been employed as sensors since 1960, after pioneering work by Günter Sauerbrey in 1959 demonstrated both experimental evidence and an analytical framework for measuring a frequency shift in resonant quartz crystal oscillators as a function of material adsorption [9]. Previously, quartz crystal oscillators had been developed as radio frequency references for the National Bureau of Standards by the Naval Research Laboratory and Bell Labs, with temperature-controlled, 100 kHz references in use by 1929 [10]. In 1964, William King demonstrated quantifiable detection of xylene adsorption on a resonant quartz plate [11], and in the near half century since the basic quartz crystal microbalance (QCM) has been applied to the detection of vapors, inorganic thin-films, proteins, nucleic acids, and whole cells [12–16]. Today, commercially available QCM systems are available for biomolecular detection and quantification [17].

A detailed discussion of the operation of an acoustic resonator will be found in Chapter 3, but its basic use as a sensor relies on the shift of a stable resonance frequency in response to the attachment of material to the sensor surface. This is illustrated in Figure 2.3. In this manner, detection proceeds without the use of a chemical labeling species, and quantification may occur in real time if the frequency is monitored continuously. This has led to the significant body of work mentioned previously to apply acoustic resonators to

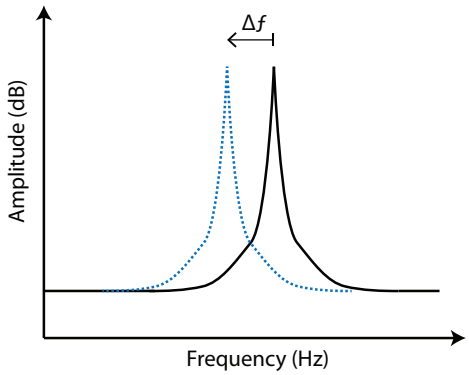

Figure 2.3: For a resonant acoustic sensor, the resonant frequency decreases in response to attached material on the sensor surface. This shift is typically small compared to the resonance frequency, on the order of 1-100 ppm.

sensing applications.

For a QCM, the resonator is formed by a thin, macroscopic disc of crystalline quartz, and the resonant frequency lies in the 1 MHz to 20 MHz range [18]. The basic frequency shift relation was first described by Sauerbrey in his 1959 paper [9], and it will be analyzed in Chapter 5. Briefly, it defines the frequency sensitivity to the mass of an attached analyte layer as

$$\frac{\Delta f}{\Delta m} = -\frac{f_\circ^2}{A \cdot N} \tag{2.1}$$

where Δf is the shift in resonant frequency, Δm is the mass of the attached layer, $f_\circ$ is the resonant frequency of the quartz disc, A is the disc surface area, and N is a sensitivity constant derived from the quartz material. Importantly, the sensitivity increases with the square of the resonant frequency $f_\circ$. Frequency increase is accomplished for the quartz crystal by making the disc thinner, but at some finite thickness (and megahertz frequency) the disc is too fragile to be used.

To further increase sensitivity, fabrication techniques developed for integrated circuits and early micro-electromechanical-systems (MEMS) devices have been employed to build acoustic resonators with ever-increasing resonance frequency [19]. These include surface-wave, bulk-wave, and contour mode resonators. A review of the state of the art for each of these techniques, as applied to sensing applications, is included in the following

sections.

Resonant quartz crystals are still employed for chemical and biological detection, and in many applications they rival the state of the art. For biological detection, Kim *et al.* have recently demonstrated a QCM-based immunoassay for detection of C-reactive protein with a detection limit of 0.130 ng/mL [20]. A competitive assay was used with a 9 MHz quartz resonator for detection in a liquid flow cell. In chemical sensing applications, Pei *et al.* have demonstrated detection of dimethyl methylphosphonate (DMMP), a compound used to simulate sarin vapor, at a concentration of 0.35 ppm [21].

Despite their continued use, quartz crystal resonators are prevented by their size from array integration, and the limited frequency range has effectively capped sensitivity scaling for this technology. Their micron-scale analogs, however, show great promise for overcoming these limitations.

Bulk acoustic wave resonators

A bulk acoustic wave (BAW) device is formed by a thin film of piezoelectric material, which deforms in response to a transverse electric field. This is the same mechanism by which the quartz crystal resonator operates, and it will be the subject of Chapter 3. The resonant frequency of a BAW device is set by the thickness (or thinness) of the resonant layer, which yields the highest attainable frequency of the acoustic resonator categories. A thin-film bulk acoustic resonator (FBAR) typically operates in the low gigahertz range. The resonance is formed by acoustic standing waves within the bulk material, as opposed to along its surface or comprised of the device flexure itself. This is illustrated in Figure 2.4.

For biological and biochemical detection, Gabl *et al.* from Siemens AG demonstrated frequency shifts in response to nucleic acid and protein detection in 2003 [22, 23]. Fabricated BAW devices with a nominal resonant frequency of 2.2 GHz were functionalized with biotinylated DNA oligomers through thioakyl bonding to the gold resonator surface. The devices were then incubated with streptavidin, and resonant frequency was measured dry between each step. Frequency shifts of 1-3 MHz were observed for both DNA and protein

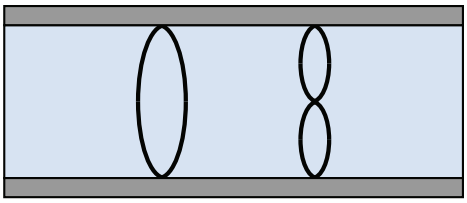

Figure 2.4: In a bulk acoustic wave device, the acoustic energy travels in the bulk material. A standing wave is excited through the thickness of the piezoelectric layer. A frequency shift occurs in response to material aggregation on the top (or bottom) surface.

attachment, and a sensitivity of 1.5-2.5 Hz·cm^2/pg was reported.

Continued work from the Siemens AG research group has established several significant advances in BAW sensing applications and performance. Weber *et al.* demonstrated in-liquid sensing through the use of shear-mode resonators for the detection of avidin/anti-avidin binding [24, 25]. A measured sensitivity of 585 Hz·cm^2/ng was reported, in comparison with 0.54 Hz·cm^2/ng for a quartz crystal. Importantly, the limit of detection for the BAW device was improved two-fold over the QCM case. These have also been shown to operate in a glycerol solution [26] and for the quantification of relative humidity and ambient carbon dioxide [27]. Nirschl *et al.* have demonstrated CMOS-integrated BAW resonators for the multiplexed detection of protein attachment and DNA hybridization with a mass sensitivity of 5.6 kHz·cm^2/ng and an average minimum detectable mass of 1.5 ng/cm^2 [28, 29]. This is early evidence of evolving sensitivity performance for integrated BAW devices, which will be the subject of Chapter 4.

In 2005, Zhang *et al.* demonstrated the use of 1.2-1.4 GHz resonators for the detection of isopropanol vapor in air with a minimum detectable mass of 1 ng/cm^2, comparable to a QCM [30]. This device was also shown to operate in liquid, and in 2010 the authors demonstrated a frequency shift of 170 ppm in response to biotin-streptavidin binding on a 600 MHz device [31]. More recently, Xu *et al.* have incorporated a microfluidic layer for the confinement of a liquid at the surface of a 1.5 GHz BAW device [32]. The authors have demonstrated a competitive protein adsorption assay with a mass sensitivity of 1358 Hz·cm^2/ng and a minimum detectable mass of 1.35 ng/cm^2.

The detection limits described above are indeed better than measured from a quartz resonator, but the improvement is not yet the one to two orders of magnitude possible from BAW devices as compared to QCM. The minimum resolvable frequency shift degrades with increasing resonant frequency, nullifying to a large extent the benefit gained from increased sensitivity. For a traditional 5 MHz QCM, the frequency can typically be resolved to within 0.1-1 Hz or 20-200 ppb, whereas a 1 GHz BAW sensor has a minimum frequency resolution closer to 0.5-1 kHz or 0.5-1 ppm [33]. This directly limits the improvement enabled by the 1000-fold increase in sensitivity measured for a BAW device.

The limited frequency resolution measured for bulk acoustic sensors arises from a decreased quality factor and an increased sensitivity to temperature as compared to a quartz resonator, which are discussed in Chapter 3 and Chapter 4, respectively. This performance gap is continuously narrowing as both fabrication and compensation techniques evolve.

Surface acoustic wave resonators

A surface acoustic wave (SAW) resonator is also formed from a piezoelectric layer, and acoustic waves travel along the surface of the material. Typically, these propagate as Rayleigh waves, which comprise particle displacement normal to the piezoelectric surface and have a finite penetration depth within the layer [34]. They are said to be 'launched' from a set of interdigitated electrodes whose spacing determines the wavelength of the surface acoustic wave, and they can be received by a second set of electrodes to form a delay line [35] or reflected from a second set of electrodes to form a resonant cavity on the substrate surface [36]. For either configuration, the piezoelectric material surface between electrode sets can be used as a physical sensing site, where changes to the material will affect propagation velocity of the surface acoustic waves. The basic SAW topology is illustrated in Figure 2.5 for comparison with the bulk wave resonator.

The SAW device was first reported by White and Voltmer in 1965 for a quartz plate [37], and both quartz and thin-film variants have since been employed commercially for use in electronic filters, delay lines, and pressure sensing applications [33, 38–40]. Rayleigh

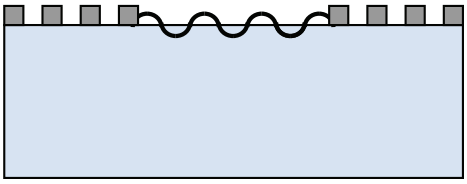

Figure 2.5: In a surface acoustic wave device, acoustic energy travels along the surface of the piezoelectric layer between sets of interdigitated electrodes. Sensing occurs in the delay region between the electrodes.

surface waves are heavily damped at a fluid interface, so most demonstrated sensing techniques target gas and vapor phase applications. These employ a thin polymer layer between the electrode sets to absorb low concentrations of organic vapors [41]. For aqueous applications, horizontal shear surface waves, which travel in the plane of the surface, and Love waves, which propagate along the full thickness of the device, are used in place of the more traditional Rayleigh wave structure.

In 2000, Rapp *et al.* implemented a multiplexed SAW sensor array using eight discrete SAW oscillators [42]. Toluene concentration as low as 26.1 μg/mL was demonstrated, and in a related work the concentrations of hexane and ethyl acetate were determined to within 1% in a binary mixture of the two vapors [43]. Many other groups have also demonstrated quantification of organic vapors using SAW sensors; this will be discussed in Chapter 5, where a similar technique is applied to integrated FBAR devices.

For chemical and biological detection in liquids, Rapp *et al.* have employed surface-shear wave SAW (SH-SAW) devices with a microfluidic enclosure for the detection of aqueous proteins. A frequency shift of 20 kHz was measured on a 426 MHz SAW sensor upon exposure to 4 mg/mL bovine serum albumin [44]. The authors have extended this work with the addition of a parylene-C sensing layer and have demonstrated linear detection response from 0.5-5 μg/mL for an anti-folic acid immunoassay [45].

Kalantar-Zadeh *et al.* have used Love mode SAW sensors for detection of proteins, where a frequency shift of 7 kHz is demonstrated after exposure to 400 ng/mL IgG (the nominal resonant frequency was not reported) [46,47]. For the quantification of nucleic acids,

Hur *et al.* have demonstrated detection of 0.1-4.0 μM DNA targets during hybridization to a functionalized 100 MHz SH-SAW sensor [48].

Surface acoustic wave devices have proven very sensitive in gas sensing applications, and several commercial systems utilizing one or more SAW devices are currently available [33]. The development of SH-SAW and Love mode SAW devices has extended their use to biological sensing applications, and they continue to be used extensively as electronic circuit elements. Despite their continued improvement, however, SAW devices suffer two primary limitations. First, the resonant frequency is limited by the spacing of the interdigitated electrodes, and modern photolithographic techniques have not enabled SAW devices much above 500 MHz. In comparison, demonstrated BAW devices have been fabricated for resonance at 5-8 GHz [49, 50]. Second, the delay line and reflector structure of a SAW resonator require large areas; a typical SAW device layout uses several square millimeters, which is 400 times larger than a typical 100×100-μm^2 BAW resonator. This area constraint makes SAW devices untenable for CMOS integration and fabrication in dense arrays.

Contour mode resonators

The high quality factor achieved in released electrostatic MEMS devices can be translated to a piezoelectric acoustic device as a contour mode resonator (CMR). The CMR device uses a thickness extensional contour mode, where the width of the structure determines the resonant frequency instead of the thickness [51]. This enables a lithographically defined resonance, like a SAW device, while maintaining the high achievable frequency and small form factor of a BAW device.

Rinaldi *et al.* have demonstrated the use of 463 MHz aluminum nitride CMR devices for the detection of 80-800 ppm dimethyl methylphosphonate (DMMP) vapor, where a sensitivity of 24.8 kHz·μm^2/fg was reported [52]. A thin layer of swingle-wall carbon nanotubes was used to increase adsorption surface area of the CMR structure. More recent work by the authors has demonstrated the integration of such a device with a CMOS oscillator by wire-bonding, and a sensitivity of 41.6 kHz·μm^2/fg to the presence of dinitrotoluene

(DNT) was reported [53]. For RF applications, CMR structures with a resonant frequency of 3.7 GHz have been demonstrated [54].

The application space for most demonstrated contour mode resonators is limited to gas and vapor sensing applications, as the damping of a liquid interface severely degrades the performance. Where shear-mode BAW and SAW devices can be employed to mitigate this effect, similar approaches do not exist for thickness-extensional CMR devices.

Conclusions regarding acoustic resonators

With the exception of the work by Nirschl *et al.* and Rinaldi *et al.*, which will be revisited, the work described in this section is limited to single-sensor applications. The acoustic resonator is monitored with a network analyzer or spectrum analyzer, both of which are bulky, complex, and expensive pieces of instrumentation. Additionally, characterization of a passive resonator through a high-frequency probe setup is practically limited to one or two sensors. While detection sensitivity is significantly increased over the traditional QCM, and the minimum limit of detection is also improved, the system functionality is inherently limited in the same manner as for the quartz resonator: a few sensors and a lot of equipment. This system-level measurement limitation can be overcome through the integration of acoustic resonators with CMOS integrated circuits, which will be discussed in Section 2.4.

2.3.2 MEMS and NEMS resonators

Cantilevers and resonant beams at both micron- and nanometer-scale have become synonymous with 'electronic nose' applications, where their parts-per-billion (ppb) sensitivity for vapor detection applications has been unrivaled. These sensors can be used in a quasi-static method, where deflection is measured when analyte binds to the cantilever surface. Alternatively, the cantilever can be driven as a resonator through electrostatic, piezoresistive, or magnetic means [33].

Li *et al.* have demonstrated a resonance shift in response to 20 ppb DMMP vapor

on a 127 MHz sub-micron cantilever [55]. This sensor had a calculated limit of detection approaching 2 ppb for DMMP when used as the output detector in a gas chromatograph, and the resonance was measured by driving the cantilever with a piezoshaker. The minimum demonstrated resolvable mass was approximately 1 attogram.

Hwang *et al.* have demonstrated a 30 kHz cantilever operating in liquid for the detection of prostate-specific antigen (PSA) [56]. A resolvable frequency shift was demonstrated for a concentration of 1 ng/mL PSA antigen, which is comparable to the performance achieved by acoustic resonators. The cantilever was driven piezoelectrically and measured with a Doppler laser vibrometer. The use of a sensitive optical system is effective for low minimum detection limits, but it presents a significant barrier to point of use application.

A fully electronic interrogation was demonstrated by Hagleitner *et al.* for a CMOS-integrated cantilever [57]. The cantilever is formed by a silicon n-well and dielectric layers in the CMOS stack, yielding a bimorph structure that can be actuated thermally. The cantilever is released by backside etch of the fabricated CMOS die, and the authors demonstrated its application to ethanol and toluene vapor sensing. A limit of detection approaching 1 ppm was reported. This work represents a substantial fabrication achievement, but also one that cannot be extended to an array of cantilever sensors.

Cantilever and resonant beam sensors have demonstrated excellent sensitivity and mass resolution for vapor applications, and in a few cases they have been applied to aqueous biomolecular detection. The sensitivity in liquid is limited compared to operation in air, as the mechanical action is significantly damped by fluid contact [33]. The fabrication methods currently used for these devices and the complex electronic or optical systems required for their quantification has prevented these technologies from leaving a laboratory environment.

2.3.3 Non-mechanical methods

The previous sections surveyed emerging mechanical techniques for real-time and label-free detection. This section reviews non-mechanical methods, including electrochemical detection, surface plasmon resonance, and capacitive and calorimetric detection.

Electrochemical detection

Electrochemical detection of chemical and biological species relies on the transfer of electrons to or from a measured electrode. This often employs an electrochemical label, where an analyte is conjugated to an electrochemically active molecule that oxidizes in the presence of an applied potential [58]. Label-free methods have been developed, however, for the detection of DNA hybridization, many of which rely on the selective oxidation of guanine or other bases [59]. Similar approaches have been employed for protein detection and for the analysis of small-molecule interaction with immobilized nucleic acids [60]. Additionally, electrochemical detection has been integrated with silicon integrated circuits, showing promise for point of use applications [61].

Despite widespread use, the majority of label-free methods for electrochemical detection are significantly less sensitive and specific than the labeled assays, as non-specific adsorption of molecules in solution also cause measurable signals. Additionally, electrochemical detection is typically limited to aqueous sensing applications.

Surface plasmon resonance

A surface plasmon propagates along the boundary of a metal-dielectric interface, and these can be excited by a specific wavelength and angle of incident light on the far side of a thin metallic layer [62]. The exact angle has a very strong dependance on the interface layer, which for the arrangement in Figure 2.6 is the metallic surface opposite the prism. Subsequently, the distribution of the reflected angles can be influenced by small changes at the metal surface, including gas adsorption, protein binding, or nucleic acid hybridization [63]. This surface plasmon resonance (SPR) technique currently sets the standard for sensitivity and resolution in real-time, label-free sensing techniques, with reported detection sensitivities as low as 0.05-0.1 ng/mL in liquid for small-molecule analytes [64]. The GE Biacore is a commercially available SPR instrument used for a variety of small-molecule affinity and kinetic investigations [65].

Though it continues to outpace competing technologies in lower limit of analyte

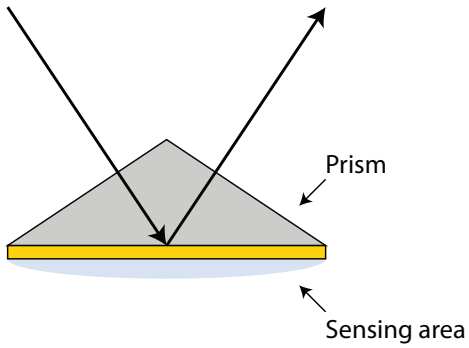

Figure 2.6: Detection by surface plasmon resonance (SPR) is very sensitive to changes at the metallic interface. This method sets the standard for sensitivity and limit of detection of real-time, label-free sensing methods.

detection, SPR inherently requires a complex, calibrated optical system for both the incident and reflected beams. This prevents its use in portable or low cost applications. Additionally, only a few sample areas can be detected in parallel, and deep multiplexing or dense array detection is not currently feasible.

Capacitive and calorimetric techniques

A gas-absorbing polymer layer can be used to quantify gas concentration by capacitive and calorimetric techniques. Both of these have been demonstrated by Hagleitner *et al.* for CMOS-integrated detection of organic gas vapors [57].

In the capacitive technique, the polymer is applied between parallel metal electrodes to form an absorption-dependent capacitance, which can be compared against a bare structure for removal of common-mode noise. Detection of 1000-3000 ppm ethanol and toluene were reported, with a calculated limit of detection of 1-5 ppm.

For calorimetric detection, a temperature difference is sought between a polymer-coated area and a bare area; as molecules absorb into the polymer layer, the temperature of this layer increases or decreases in response to the change in enthalpy. Similar detectable concentrations of ethanol and toluene vapor were reported.

These methods are demonstrated as CMOS compatible, but they cannot be scaled to small devices and dense arrays. Both the capacitive and calorimetric methods depend

on large areas to produce a measurable change in capacitance or temperature. Unlike BAW sensors, these methods will degrade in sensitivity as sensors are made smaller and closer together.

2.3.4 A brief note on single-molecule sensing

All of the methods reviewed in this section rely on ensemble molecular detection. Many theses worth of single-molecule detection techniques have also been developed, and this area of research lies at the limit of molecular sensitivity. Such devices include nanowires, nanotubes, and many of the smallest nanometer-scale mechanical resonators [66–68]. While these technologies hold great promise for future use, they have been excluded from review in this section. Their development is too recent and application space too undeveloped for reasonable comparison with ensemble techniques. For specific application comparison, such as organic vapor detection, some of these systems will be revisited in Chapter 5.

2.3.5 Comparison of label-free sensing techniques

There are few application-independent metrics by which to compare the sensor modalities reviewed in this section. Vapor sensing applications are typically quantified by minimum detectable gas concentration, which depends on the gas species, capture layer, and ambient environmental conditions. For aqueous biological sensing, the limit of detection is most effectively characterized by concentration of the target analyte in the liquid, which is similarly dependent on capture mechanism, affinity, temperature, sample matrix, and pH. For the development of a broadly applicable sensor platform, a multitude of applications and conditions must be considered.

For the comparison of real-time and label-free technologies, the sensitivity and detection limits can be compared across applications by extracted mass, so long as the previous caveat is observed. Table 2.1 summarizes these values for several of the emerging technologies reviewed in this section. The values for surface plasmon resonance are also included, as it represents the current commercial laboratory standard.

Table 2.1: Summary of label-free detection methods. Values are reported by or deduced from: QCM [69], SAW [70], BAW [33], CMR [53], SPR [71]. SPR and QCM are reported in liquid, others in air.

	QCM	**SAW**	**BAW**	**CMR**	**SPR**
Sensitivity [Hz·cm^2/g]	500×10^5	15×10^9	100×10^{10}	400×10^9	100×10^7 mdeg·cm^2/g
LOD Limiter [Hz]	0.1	10	1000	20	0.1 mdeg
LOD [ng/cm^2]	2	0.7	1	0.05	0.10
Typical Area [cm^2]	1	40×10^{-3}	1×10^{-4}	0.3×10^{-5}	1×10^{-5}
Min. Resolvable Mass [ng]	2	3×10^{-4}	1×10^{-4}	1.5×10^{-6}	1×10^{-6}
Air/Gas Operation	Yes	Yes	Yes	Yes	Yes
Liquid Operation	Yes	Yes	Yes	No	Yes
CMOS Monolithic	No	No	Yes	No	No
Arrayble	No	No	Yes	Yes	No

As can be deduced from Table 2.1, BAW devices represent the most promising of these techniques for the integration with portable electronics and use in a broad scope of applications. These sensors do not represent the lowest attainable limit of detection, but the sensitivity and resolution of extant devices is sufficient for many applications, and future devices will continue to increase sensitivity and lower the minimum resolvable mass.

2.4 Integrating acoustic resonators with CMOS circuits

High-frequency acoustic resonators have been limited to laboratory sensing applications by the bulky, complex, and expensive electrical equipment required to measure them. For a traditional QCM operating in the low megahertz range, the quartz crystal can be attached by cable to an oscillator circuit and monitored with a standalone frequency counter. For acoustic resonators operating at hundreds of megahertz or several gigahertz, delays, reflections, and parasitic loading make this simple topology infeasible. The resonator must be brought much closer to the oscillator and frequency counter. This is accomplished by integrating the electronic circuitry on a CMOS substrate and locating the resonator in close proximity. Wire-bond, flip-chip, and monolithic processes have been developed for this interface and are reviewed in this section.

2.4.1 Wire-bonding

The majority of published examples of acoustic resonator integration with CMOS circuitry are for application to high-frequency clocks, filters, and duplexers [72]. For these applications, only a few resonators are required, and a straightforward wire-bond interface is employed. This technique involves the ultrasonic welding of a very small-diameter ($\sim$50 μm) gold or aluminum wire between the pads of adjacent substrates.

Otis *et. al.* were the first to demonstrate a CMOS oscillator using a BAW device as the resonant tank, where an off-chip FBAR substrate was connected to a 0.18 μm CMOS chip to form a 300 μW 1.9 GHz oscillator [73]. This work was extended by Chee *et al.* with the demonstration of a 100 μW 1.9 GHz oscillator formed from a wire-bonded FBAR device [74]. Many publications have followed that report increased frequency, decreased power, and maintain the basic single FBAR wire-bonded topology [75–78]. In these applications, the overarching goal is to improve phase noise performance while decreasing power, where high quality factor FBAR resonators provide a significant advantage over frequency synthesis, ring-oscillator, and LC methods [79].

Multiple BAW devices have been integrated through a wire-bond interface by Chabloz *et al.* to implement a bandpass filter at the input of a low noise amplifier for application to an RF receiver [80]. Four BAW structures on a single substrate form a lattice filter around 2.4 GHz, which was attached a CMOS substrate via four wire bonds for differential interface. Rinaldi *et al.* have also demonstrated the integration of multiple off-chip resonators; four contour mode resonators were used as a switchable resonant tank to enable a frequency-selectable oscillator on an adjacent CMOS circuit substrate [81]. On-chip oscillator frequency was switched among the four available CMR frequencies from 268-785 MHz with a power consumption of 0.4-4 mW.

Wire bonds add additional parasitic inductance to the electrical path, but the published work makes clear that this does not prevent the implementation of oscillators and filters in the low gigahertz range. However, this is due to a very close spacing, with a typical wire bond length for an off-chip FBAR implementation of less than a few millime-

ters [73]. For applications in which many resonators are required, such as multiplex sensing, the wire-bond implementation technique is not applicable.

2.4.2 Flip-chip and wafer-level transfer

To further decrease the parasitic contribution of the wiring between an FBAR and a CMOS circuit, Augustyniak *et al.* have demonstrated a flip-chip implementation [82]. Eight 1.9 GHz FBAR devices were fabricated on a silicon substrate alongside metalized receiving pads. Oscillators were implemented in a 0.13 μm CMOS process, and the CMOS substrate was inverted and attached to the metalized receiving pads on the FBAR substrate by solder balls. This arrangement limits the wiring length from circuit to FBAR to 600 μm, which the authors estimate adds 0.7 Ω and 1 nH in parasitic loading. The oscillator was shown to operate with the resonator both in air and in water.

Campanella *et al.* implemented an integrated process using wafer-level transfer of FBAR devices to a CMOS substrate [83]. Resonators were fabricated on a sacrificial substrate, and these were bonded to a receiving CMOS substrate using metalized receiving posts. The FBAR substrate was removed by an etch process, leaving FBAR devices connected directly above the integrated circuit substrate. The authors demonstrated the transfer and characterization of a 2.4 GHz resonator, but no active circuits were employed.

The flip-chip and wafer-transfer methods address the parasitic loading of wire-bond attachment, but they suffer the same integration limitation faced by wire-bonding and all package-level integration techniques; the method can only be applied to a few, linearly arrange devices and cannot support the development of an array of resonators.

2.4.3 Monolithic fabrication

Large arrays of acoustic resonators can be implemented with monolithic CMOS integration. In this method, resonators are fabricated directly on the CMOS chip surface, either as part of the original CMOS fabrication or as a post-processing step. This enables arrays of devices that are collocated with required support circuitry, and the number and density of sensors

is limited only by the size of a resonant device and the footprint of the associated circuitry.

For RF applications, Dubois *et al.* have developed a monolithic fabrication method for building released FBAR structures on a fabricated CMOS substrate [84]. Eight devices were used to construct a double-stage lattice filter around 2.1 GHz, and a 2.2 GHz filtering low noise amplifier was also demonstrated. Aissi *et al.* has extended this work to design a 5 GHz balanced oscillator with a single monolithically integrated resonator [50].

For sensing applications, the work by Nirschl *et. al.* (Siemens AG) described previously for protein detection was implemented with an array of 64 monolithically integrated acoustic resonators [28]. Devices with a resonance around 800 MHz were used for protein detection, where resonance was measured on chip using impedance spectroscopy. This fabrication method shows significant promise for a broad scope of biological and chemical detection applications. The use of on-chip impedance spectroscopy, while successfully integrating the measurement electronics, may limit the attainable frequency resolution of the system. In addition to the limited frequency resolution introduced by a resonator with a finite quality factor, the use of an integrated VCO for impedance spectroscopy introduces additional error, where the swept VCO frequency is not an ideal source. This will be addressed in Chapter 5.

2.5 An array of monolithic FBAR-CMOS oscillators

This chapter has presented the background and motivating framework for the research and development described in the remainder of this dissertation. Acoustic wave devices have the potential to bring laboratory-grade sensitivity and specificity to point of use applications. They remove the need for optics and sample labeling, and they enable real-time quantification of binding and sorption events. Their use still requires the application of high-speed, high-performance electronic interrogation, and CMOS integration will enable this in a small, low-cost, and highly manufacturable format.

For the most broadly useful sensing platform, an array of individually addressable sensors is required than can be functionalized independently, measured in parallel, and

fabricated in dense arrays. Previous work has shown many examples of interfacing acoustic resonators and integrated circuits, but these package level techniques significantly limit the ability to build sensor arrays. More recent work on monolithic resonator integration has shown promise, as it enables many sensors in a small array atop the measurement circuitry.

The remaining chapters of this dissertation describe a body of work directed at the monolithic integration of acoustic resonators with a silicon integrated circuit substrate. This is used to build an array of real-time, label-free sensors that can be adapted to point of use applications. The sensor platform is demonstrated for a vapor sensing application in Chapter 5, which highlights one of the many applications addressable by this technology.

Chapter 3

Design and fabrication of thin-film bulk acoustic resonators

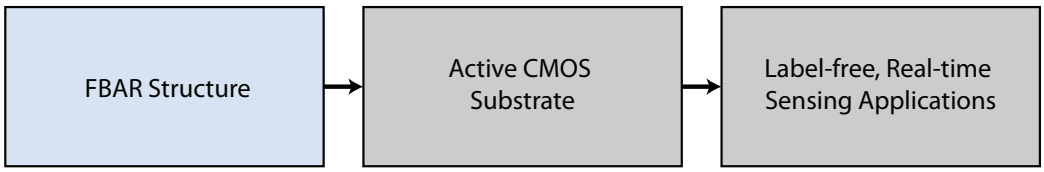

Figure 3.1: Chapter 3 discusses the theory, design, fabrication, and characterization of thin-film bulk acoustic resonator devices.

3.1 Introduction

This chapter begins with an introduction to elasticity and wave propagation in solid materials, which is used to describe bulk resonant modes in thin films. The piezoelectric effect is introduced to describe transduction between electrical and mechanical energy modes, which forms the basis of the resonant behavior and of its use in electrical circuits. This is also, quite literally, the driving force behind most modern high frequency acoustic devices. Mechanical isolation methods are described, with a particular emphasis on the operation and simulation of periodic acoustic reflectors. Finally, the design, fabrication, and characterization of simple FBAR structures are presented. These devices will form the basis of the monolithically fabricated FBAR structure on integrated circuit substrate discussed in

later chapters.

The treatment of wave propagation, resonance, and acoustic reflection given here is intentionally simplified. Where possible, equations are reduced to a single dimension and only design-relevant aspects of associated tensors and matrices are included. A complete review can be found in [85]. The aim in this section is to provide a sufficient background on which to develop an intuition for the design tradeoffs in FBAR fabrication.

3.2 Basic structure of a thin-film bulk acoustic resonator

A thin-film bulk acoustic resonator (FBAR) is formed when a thin layer of piezoelectric material is sandwiched between two electrodes. This is depicted in Figure 3.2. When an alternating voltage is applied to the electrodes, the piezoelectric material is deformed, alternately stretching and compressing the structure like a simple spring. There is a specific driving frequency, natural to the particular device dimensions, at which the magnitude of this deformation is maximized, forming a resonator. This is analogous to the 32,768 Hz quartz crystal resonator found inside a modern timepiece, which yields a stable and precise frequency reference for ticking off seconds [86]. A very similar structure can be found in filters and radios of modern electronic devices, with these resonators operating well into the gigahertz range [87]. All of these devices follow from the same basic structure and operating principles, many of which are discussed here.

Modern FBAR devices typically employ zinc oxide or aluminum nitride as the piezo-

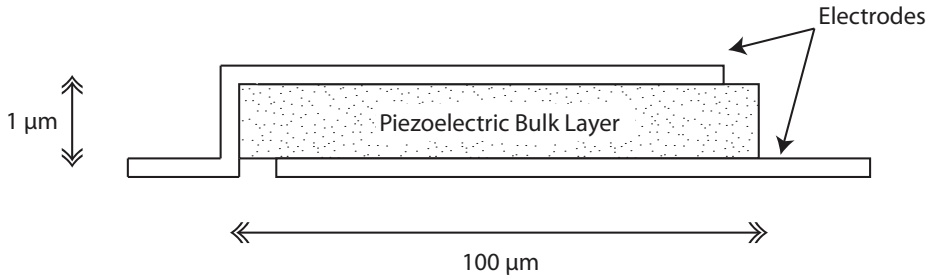

Figure 3.2: Illustration of an FBAR cross-section. In its simplest form, an FBAR is formed when a piezoelectric layer is sandwiched between two electrodes. Typical dimensions are given, and illustration is not to scale.

electric layer. In the following sections, these will be used as example materials for the description of physical properties, and zinc oxide will be used for the fabrication of measured devices.

3.3 Acoustic wave propagation in elastic solid materials

An acoustic wave is a vibration. It travels through a solid medium by way of localized particle displacement; minor perturbations of atoms from their equilibrium positions comprise a much larger, ensemble wave motion [88]. From a macroscopic perspective, the wave travels, the particles do not. This solid can be imagined as a distributed mass-spring system, where particles are confined by localized restoring forces; the nodes of this system need not be individual atoms. For an ideal spring, physical deformation is linearly proportional to the applied force, as described by the simplest form of Hooke's Law [89]

$$F = -kx \tag{3.1}$$

The strain x is linearly proportional to the stress F, with a constant of proportionality k, referred to commonly as the spring constant. For small deformations, the process is reversible, and a stretched or compressed spring will return to its original state when the external force is removed. This is an *elastic deformation*. This property applies also to bulk solids, as does the same empirical law of linear proportionality [85]. To understand the one dimensional bulk case, we must briefly consider stress and strain in more dimensions.

3.3.1 Stress and strain

Stress is a measure of internal restoring forces arising in a deformed material, which stem from the chemical structure of the underlying solid and define our microscopic spring constants. As a measure of normalized force, stress is quantified per unit area, giving stress vectors units of pressure. For a particle in the material, which we define as a volume cell with faces orthogonal to the x, y, z unit vectors in a rectangular Cartesian coordinate system, a

stress vector can be described by its axial force components

$$\mathbf{T}_x = \hat{\mathbf{x}}T_{xx} + \hat{\mathbf{y}}T_{yx} + \hat{\mathbf{z}}T_{zx} \tag{3.2}$$

$$\mathbf{T}_y = \hat{\mathbf{x}}T_{xy} + \hat{\mathbf{y}}T_{yy} + \hat{\mathbf{z}}T_{zy} \tag{3.3}$$

$$\mathbf{T}_z = \hat{\mathbf{x}}T_{xz} + \hat{\mathbf{y}}T_{yz} + \hat{\mathbf{z}}T_{zz} \tag{3.4}$$

which denote the stress associated with the x, y, and z directions, respectively. Each of these forces is comprised of a normal stress component, in the direction of the associated unit vector, and two shear stress components, along the two orthogonal axial planes containing the unit vector. The nine associated stress components, T_{ij}, reduce to only six independent components with planar shear stresses being symmetric, where $T_{ij} = T_{ji}$. The $i = j$ terms in the T_{ij} matrix describe the normal (longitudinal) stress components, with $j \neq i$ terms describing shear stress.

Particle displacement itself is measured as strain. Consider our volume cell particle at a location described by the vector $\mathbf{r}$ undergoing a displacement described by the vector $\mathbf{u}$. For the simple, linear case, the time dependent strain is related to displacement as

$$S_{ij}(\mathbf{r}, t) = \frac{1}{2}\left(\frac{\partial u_i}{\partial r_j} + \frac{\partial u_j}{\partial r_i}\right) \tag{3.5}$$

which yields nine strain components S_{ij}. As with stress, only six of these components are independent, with planar symmetry yielding $S_{ij} = S_{ji}$, and again noting that $i = j$ components describe normal (longitudinal) strain and $j \neq i$ components describe shear strain.

We can now extend the simple $F = -kx$ form of Hooke's Law in (3.1) to the more general, multidimensional

$$T_{ij} = c_{ijkl}S_{kl} \tag{3.6}$$

where i, j, k, l represent all permutations of x, y, z in the rectangular coordinate system, yielding a total of 81 constants. The spring constant k has been expanded to many elastic stiffness constants c_{ijkl} to describe coupling in the mass-spring analog system. Note that the

signs of k and c_{ijkl} are reversed; in both systems the restoring force opposes the applied force. As with stress and strain components, not all of the stiffness constants are independent, and the 81 are reduced to a simple 6×6 matrix, aligning with the six-component T_{ij} and S_{ij} vectors in (3.6). Ultimately, any crystalline material can be described by at most 21 stiffness constants, with the majority of common structures requiring far fewer [85].

A subscript notation is commonly used for describing the set of independent elastic stiffness constants, substituting c_{ij} for c_{ijkl} with i, j chosen from $1 = xx, 2 = yy, 3 = zz, 4 = yz, zy, 5 = xz, zx, 6 = xy, yx$. For example, c_{11} describes the x-only dependent stiffness constant c_{xxxx} and c_{44} describes the yz-plane stiffness constants $c_{zyzy} = c_{yzyz}$. For the design of simple bulk acoustic wave devices, it will suffice to consider one-dimensional wave propagation, which for each axial direction and propagation mode is associated with a single stiffness constant. The relevant stiffness constant will depend on the propagation mode, direction, and crystal structure of the propagation medium, as a stiffness constant c_{ij} may denote different relations in different crystal classes.

For simplicity, the Hooke's Law relationship of 3.6 can be expressed in the tensor notation

$$\mathbf{T} = \mathbf{c} : \mathbf{S} \tag{3.7}$$

where the double dot product indicates the summation over pairs of indices.

For the design of practical FBAR devices in zinc oxide or aluminum nitride, the relevant stiffness parameters are c_{33} and c_{44}. These describe the stress-strain for a z-axis propagating longitudinal wave (c_{33}) and shear wave (c_{44}), which propagation modes are discussed in Section 3.3.3. Notably for these materials, c_{33} and c_{11} are ascribed to longitudinal modes along the ^{+}z-axis (0001) and ^{-}z-axis (1000), respectively, with $c_{11} \approx c_{33}$ [85].

3.3.2 Wave propagation in an isotropic solid

The one-dimensional wave equation can be derived from Newton's second law

$$F = m \cdot a \tag{3.8}$$

where the force F is determined by the stress component, which as described in Section 3.3.1 denotes a force per area. Subsequently, the derivative of stress over some small displacement in z gives force per volume. The mass m per volume is given by material density ρ, and acceleration a is simply the second time derivative of a particle displacement function $u(z,t)$ [90]. For the moment, we consider only the non-piezoelectric, isotropic bulk material, and we assume zero material losses. These relationships

$$F = \frac{\partial T}{\partial z} \cdot \Delta V \tag{3.9}$$

$$m = \rho \cdot \Delta V \tag{3.10}$$

$$a = \frac{\partial^2 u}{\partial t^2} \tag{3.11}$$

are combined with (3.8) to yield

$$\frac{\partial T}{\partial z} = \rho \cdot \frac{\partial^2 u}{\partial t^2} \tag{3.12}$$

and for the one-dimensional case of propagation in z, we can simplify (3.5) and (3.6) to

$$T_z = c_{ii} \cdot S_z \tag{3.13}$$

$$S_z = \frac{\partial u}{\partial z} \tag{3.14}$$

which are substituted into (3.12) to yield the characteristic acoustic wave propagation equation

$$\frac{\partial^2 u}{\partial t^2} = \frac{c_{ii}}{\rho} \cdot \frac{\partial^2 u}{\partial z^2} \tag{3.15}$$

whose nontrivial solution describes a periodic, acoustic plane wave. The phase velocity for this solution is a materially determined property comprising stiffness constant of the particular propagation mode, c_{ii}, and bulk material density, ρ. This is described as

$$V_p = \sqrt{\frac{c_{ii}}{\rho}} \tag{3.16}$$

which is closely related to the characteristic acoustic impedance Z_α, defined by the same material properties as

$$Z_\alpha = \rho V_p = \sqrt{\rho c_{ii}}. \tag{3.17}$$

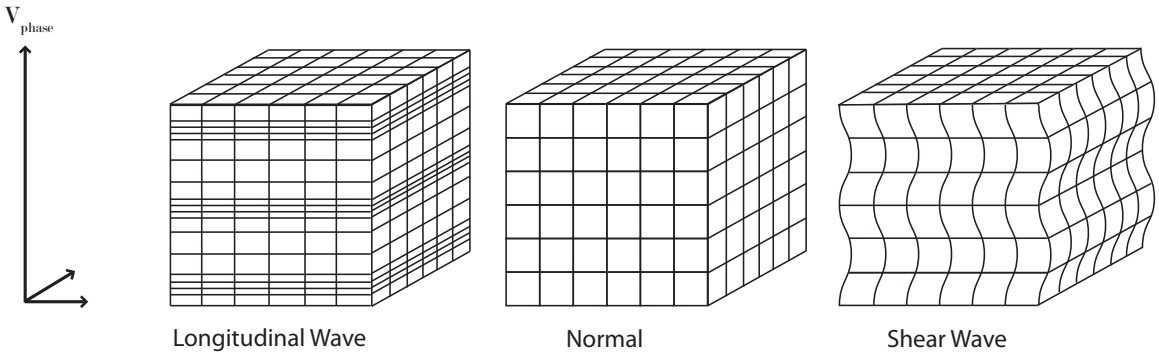

Figure 3.3: A bulk resonator supports multiple modes of traverse acoustic waves. A longitudinal wave, or compression wave, has particle displacement parallel to its propagation axis. A shear wave has particle displacement orthogonal to the propagation axis.

As with wave propagation in other domains, the acoustic wavelength λ_α of a plane wave propagating in a bulk material is defined by the wave frequency and by the phase velocity in the medium, such that

$$\lambda_\alpha = 2\pi \frac{V_p}{\omega_\alpha} = \frac{V_p}{f_\alpha} \tag{3.18}$$

for an acoustic wave. Acoustic wavelength, acoustic velocity, and characteristic impedance are important design parameters for FBAR devices, and these will be revisited.

While developed for the simplified case of one-dimensional wave propagation in an isotropic solid, the propagation equation and acoustic parameters developed here accurately describe two distinct modes of transverse propagation in a bulk material.

3.3.3 Acoustic wave propagation modes

For thin-film bulk acoustic resonators, there are two propagation modes that are of particular interest: thickness longitudinal mode and thickness shear mode. Both modes describe transverse wave propagation parallel to the thickness direction, which is normal to the substrate in most thin-film resonators. The two basic propagation modes are illustrated in Figure 3.3, where deviations from a regular grid represent localized particle displacement from the equilibrium condition.

Shear mode

For a thickness shear mode (TSM) acoustic wave, particle displacement within the bulk is perpendicular to the transverse wave propagation axis, as depicted in Figure 3.3. A shear wave is polarized, with the direction of particle displacement denoting polarization. For example, a shear acoustic wave propagating along the z-axis might have its associated particle displacement parallel to the x-axis or the y-axis, or parallel to any line in the xy plane.

In-liquid FBAR sensing applications typically employ TSM acoustic waves. For such a structure, the top sensing surface moves side to side, parallel to the sensor-liquid boundary. Energy is not efficiently coupled across this boundary, as fluids do not support shear wave propagation modes. The mechanical action is therefore minimally degraded by energy loss. Bjurström *et al.* have demonstrated a 1.6 GHz membrane FBAR operated with one face in air and one face in water; the quality factor was degraded from 350 in air to 150 with one face in water [91]. Quality factor will be detailed in Section 3.5.3.

Shear propagation modes can be excited in an FBAR structure using two common methods. The first is to grow a zinc oxide or aluminum nitride film whose columnar, piezoelectric c-axis is tilted with respect to substrate normal [91, 92]. When a normal electric field is applied, both shear and longitudinal modes can be excited, and with proper design of the auxiliary circuits a shear-mode resonance can be sustained. The alternate method is to use lateral field excitation, in which electrodes are applied on either side of the resonator surface, instead of through its bulk. This produces a lateral electric field within the piezoelectric layer, which can excite TSM waves within the bulk material. This method has been employed by Dickherber *et al.* to demonstrate aqueous biosensing [93].

Longitudinal mode

For a thickness longitudinal mode (TLM) acoustic wave, particle displacement within the bulk is parallel to the transverse wave propagation axis. Wave propagation comprises alternating peaks and troughs of higher and lower density material planes, forming a compression

wave. This is depicted in Figure 3.3. For an FBAR device, a propagating TLM wave yields a top surface that moves up and down. In air or vacuum, this motion is largely unimpeded, and the top surface is effectively an unclamped boundary. In a liquid environment, however, this top surface motion will efficiently transfer energy at the fluid interface by exciting compression waves in the liquid, which significantly damps the mechanical action of the bulk material. This is experimentally demonstrated in Section 3.7.6.

For thin-film bulk acoustic wave (BAW) resonators, the TLM has been employed commonly in both RF applications and gas-based sensing applications [27, 74]. This is due in part to the straightforward deposition of zinc oxide and aluminum nitride with a piezoelectric *c*-axis normal to the substrate. For the basic FBAR structure shown in Figure 3.2, this yields an electric field parallel to the piezoelectric axis, which excites a longitudinal wave in the bulk material. Additionally, the longitudinal mode for a given crystal has a higher phase velocity than does the shear mode, yielding higher frequency devices for a given thickness [85]; this is advantageous for both RF and sensing applications. The devices built and measured in this and later chapters are all longitudinal mode resonators.

While longitudinal mode resonators are rarely used in a liquid environment, aqueous TLM operation has been demonstrated by Zhang *et al.* using a zinc oxide resonator on a thin silicon nitride support membrane [30]. A quality factor (Q) degradation from 200 down to 10 was reported. More recently, Xu *et al.* have demonstrated a method to confine a very thin fluid layer at the resonator surface [32]. This microfluidic layer is thick enough to be useful as a sensing layer, with a thickness of 4-5 μm, but it is thin enough that energy cannot be effectively coupled into the fluid layer. This mitigates the commonly observed Q degradation and suggests that TLM operation is a viable modality for aqueous sensing.

3.4 Resonance of a bulk thin-film layer

A mechanical resonance occurs in a system that is characterized by both a mass and a deflection-dependent restoring force; this includes a simple pendulum, in which the restoring force is gravity, and a simple mass-spring system, in which the restoring force is governed

by the spring constant. The resonant frequency of the mass-spring system is

$$\omega_\circ = \sqrt{\frac{k}{m}} \tag{3.19}$$

where k is the spring constant and m is the attached mass. As it oscillates, a mechanical resonator converts energy alternately between potential energy and kinetic energy. The pendulum and the spring each have a single normal resonant mode, which is limited by each system having a single degree of freedom. For a coupled spring system, with two masses, the system has two degrees of freedom, and two normal resonant modes are found [89].

As described in Section 3.3, an elastic solid, such as a crystal, can be likened to a distributed mass-spring system, with a multitude of nodes. Continuing this analogy, the bulk solid can support a *very large* number of resonant modes. However, it is only the modes in which forward and reverse waves constructively interfere that can be sustained in an observable resonance.

A resonator is bounded. For a thin-film BAW device, the most relevant boundaries are set by the thickness of the film, as reflections of propagating waves occur at these interfaces. Constructive interference will occur when the forward and reverse waves are in phase, which requires that the total path length be equal to a wavelength multiple [34]. A wave that leaves one resonator face, travels the thickness d, reflects at the second resonator face, and returns over the thickness d, will be in phase when it reaches the original face if $2d = n \cdot \lambda_\alpha$ for positive integer n. At these wavelengths, propagating waves of wavelength λ_α will add to form a standing wave of wavelength λ_α. The fundamental mode will occur for $n = 1$ at $2d = \lambda_\alpha$, and as such thickness BAW devices are often referred to as half-wavelength resonators. As a design parameter, the target thickness for a BAW resonator is given as

$$d = \frac{1}{2} \cdot \frac{V_p}{f_\circ} \tag{3.20}$$

where d is layer thickness, V_p is the phase velocity of the thickness mode wave in the target material and $f_\circ$ is the target resonant frequency. For a crystalline acoustic layer in the low gigahertz range, d will be on the order of one micron, as shown in Figure 3.2.

In the special case of a piezoelectric resonator, resonance is still developed in the piezoelectric medium in the same manner, with only slight and often negligible differences in stiffness [85]. In this case, however, in addition to energy transfer alternately from mechanical potential to kinetic energy, there is additionally energy transfer to and from electrical potential, which enables the practical implementation of BAW devices. This result has been anticipated in previous sections, but it will be developed directly in Section 3.5.1.

3.5 Piezoelectric materials and deposition

So far, the piezoelectric effect has been omitted from the treatment of elastic media in order to simplify the description of acoustic waves. However, nearly all modern thin-film resonators are built from piezoelectric materials [94], and it is piezoelectricity that allows them to interact with electrical systems.

3.5.1 Piezoelectric effect

The piezoelectric effect is observed in certain materials in which a charge is developed in response to the material being stretched or compressed; it is literally a 'squeeze-charge'. This electrical-mechanical coupling arises in materials lacking inversion symmetry, as shown schematically in Figure 3.4. As the material is deformed, the positive and negative charge centers move in opposite directions, electrically polarizing the bulk material. Such materials also exhibit a reverse piezoelectric effect, in which an applied electric field causes mechanical deformation of the bulk crystal structure. Further, both the piezoelectric effect and its inverse are, for small deformations, reversible and symmetric; if a field in one direction causes a contraction of the bulk material along its piezoelectric axis, a field in the opposite direction causes an extension along the same axis [88]. This simple relationship is depicted in Figure 3.5. This reversible transduction between electrical and mechanical energy makes piezoelectric materials valuable for many sensor and actuator applications.

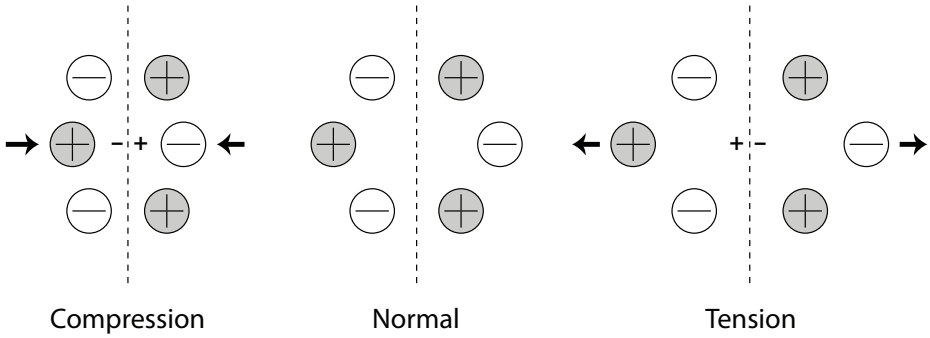

Figure 3.4: The direct piezoelectric effect arises in crystal structures that lack inversion symmetry. A compressive or tensile deformation of the bulk displaces bound charge centers, causing a polarization of the bulk material. The polarity of charge displacement is opposite for tension and compression.

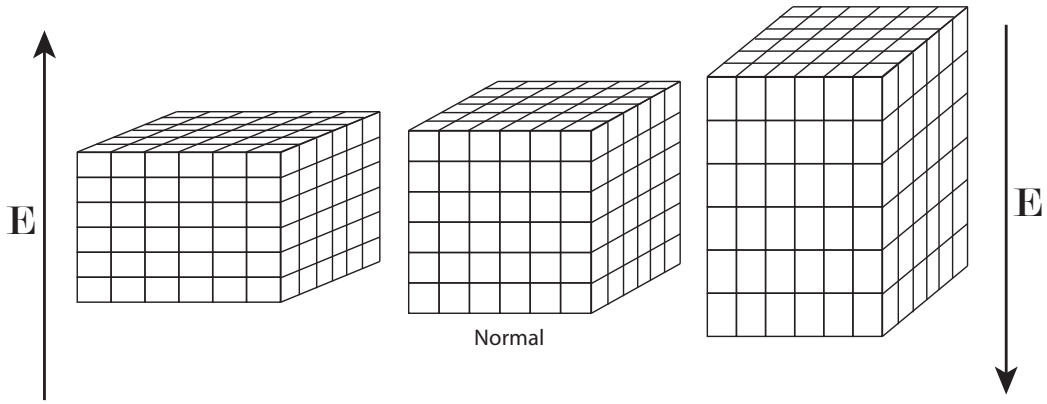

Figure 3.5: The reverse piezoelectric effect describes a bulk transduction between electrical and mechanical domains. An electric field in one direction compresses a piezoelectric slab, while an electric field in the opposite direction stretches the slab.

3.5.2 Constitutive relations

In a simple dielectric material, the separation of bound charges is described by the electrical displacement field $\mathbf{D}$, which is a function of the applied electric field $\mathbf{E}$ and and the permittivity in the material $\boldsymbol{\varepsilon}$, as

$$\mathbf{D} = \boldsymbol{\varepsilon} \cdot \mathbf{E} \tag{3.21}$$

where the single dot product indicates summation over single subscripts.

In a piezoelectric material, mechanical and electrical properties are coupled. This complicates the standard relationship for electrical displacement, as an applied electric field induces strain, which in turn impacts the effective electrical displacement. It also complicates Hooke's Law, where in a piezoelectric material strain induces both stress and electrical polarization, both of which induce restoring forces. These behaviors are described by piezoelectric constitutive relations, which couple the electrical and mechanical domains, modifying the standard forms of (3.7) and (3.21). One of several possible ways to describe these relations is with the stress-charge equations [85]

$$\mathbf{T} = \mathbf{c}^{\mathbf{E}} : \mathbf{S} - \mathbf{e} \cdot \mathbf{E} \tag{3.22}$$

$$\mathbf{D} = \mathbf{e} : \mathbf{S} + \boldsymbol{\varepsilon}^{\mathbf{S}} \cdot \mathbf{E} \tag{3.23}$$

where $\mathbf{T}$ and $\mathbf{S}$ are stress and strain as described in Section 3.3.1, $\mathbf{E}$ is the electric field, $\mathbf{D}$ is the electrical displacement, $\mathbf{c}^{\mathbf{E}}$ is the stiffness under constant electric field, $\boldsymbol{\varepsilon}^{\mathbf{S}}$ is the permittivity under constant strain, and $\mathbf{e}$ is a newly defined matrix of piezoelectric stress coefficients, which have units of charge per area.

For acoustic propagation, it can be shown that the effect of this electrical-mechanical coupling is to increase the stiffness of a piezoelectrical material above what would be calculated for the non-piezoelectric case [85]. Piezoelectric stiffening intuitively arises from the additional restoring force induced by the charge polarization in the material. For the materials of particular interest to thin-film acoustic resonators, zinc oxide and aluminum

nitride, the one-dimensional piezoelectric stiffening reduces to

$$\bar{c}_{33} = c_{33}^{E} + \frac{e_{z3}^2}{\varepsilon_{zz}^{S}} \tag{3.24}$$

$$\bar{c}_{44} = c_{44}^{E} + \frac{e_{x3}^2}{\varepsilon_{xx}^{S}} \tag{3.25}$$

which typically yields a minor increase in stiffness. For example, for a longitudinal mode in zinc oxide, we have

$$c_{33} = 21.09 \times 10^{10}\ [\mathrm{N/m^2}] \tag{3.26}$$

$$\bar{c}_{33} = 23.02 \times 10^{10}\ [\mathrm{N/m^2}] \tag{3.27}$$

which corresponds to an increase in the phase velocity in (3.16) of

$$V_\alpha = 6093\ [\mathrm{m/s}] \tag{3.28}$$

$$\overline{V}_\alpha = 6366\ [\mathrm{m/s}]. \tag{3.29}$$

Subsequently, while the piezoelectric effect is critical to the electrical use and theoretical electrical modeling of elastic solids, in most cases has a minimal effect on acoustic propagation in the bulk material.

3.5.3 Resonator performance metrics

Piezoelectric materials and devices are typically employed as transducers, interchangeably converting mechanical and electrical energy. This process is not inherently efficient, and related metrics are used to quantify this conversion.

Electromechanical coupling coefficient, k^2

When a crystal is stretched or compressed, it has imparted to it a potential energy that is a function both of its material elasticity and the magnitude of its deformation. For a piezoelectric material, this energy is stored as mechanical stress and separated charge. As with a real, non-ideal spring, the energy required for this deformation is greater than that stored as potential, with the remaining fraction accounted for by internal material

losses. That is, for a piezoelectric material, the electrical energy required to deform the material is greater than the subsequent energy stored by the mechanically deformed bulk. Conversely, if a piezoelectric crystal is squeezed, the mechanical energy required to squeeze the bulk is greater than the electrical energy stored in the resulting polarization, with the remaining energy accounted for by mechanical strain and material loss. These two symmetric inefficiencies have the same magnitude. As such, a ratio k of energy applied to energy transduced is defined, and it is equal for the two cases described:

$$k = \sqrt{\frac{\text{stored mechanical energy}}{\text{applied electrical energy}}} = \sqrt{\frac{\text{stored electrical energy}}{\text{applied mechanical energy}}} \tag{3.30}$$

Typically reported as k^2 to describe a full conversion cycle, the electromechanical coupling coefficient is a measure of the efficiency with which energy transduction between electrical and mechanical domains occurs. For piezoelectric thin-film devices, this is a function both of the piezoelectric material chosen as well as the structure, purity, roughness, grain size, homogeneity, and crystallinity of the deposited film. It serves as an accurate measure of film quality as it relates to piezoelectric behavior, and it is directly related to the resonator quality factor, detailed below.

A maximum attainable electromechanical coupling k_t^2 is determined by piezoelectric and elastic material parameters, which for a longitudinal mode can be calculated as

$$k_t^2 = \frac{e_{33}^2}{c_{33}^D \varepsilon_{33}^S} \tag{3.31}$$

where e_{33} is the longitudinal piezoelectric stress coefficient, c_{33}^D is the longitudinal stiffness constant under constant electrical displacement, and ε_{33}^S is the permittivity subject to constant strain [49]. This maximum value is never attained in practice, however, where devices are impure, polycrystalline, and suffer material losses. In aluminum nitride, for example, theoretical k_t^2 approaches 7%, whereas reported effective values commonly range from 1% to 5% [34].

For measured devices, the effective electromechanical coupling can be calculated from the separation between the resonance (series) and antiresonance (parallel) frequencies

of a device as

$$k_t^2 = \frac{\pi}{2}\frac{f_s}{f_p}\tan\left(\frac{\pi}{2}\frac{f_p - f_s}{f_p}\right) \approx \frac{\pi^2}{4}\frac{f_s}{f_p}\frac{f_p - f_s}{f_p} \tag{3.32}$$

where f_s is the series resonant frequency, and f_p is the parallel resonance frequency [95]. These frequencies can in practice be taken as the local maximum and minimum of a measured device admittance [49].

Finally, k_t^2 describes a coupling property for the piezoelectric material layer, but additional losses in a fabricated device degrade the attainable electromechanical coupling of the whole structure. These losses stem primarily from spurious modes and contact impedance, and they are accounted for by defining an effective attainable electromechanical coupling k_{eff}^2 as

$$k_{\text{eff}}^2 = \frac{f_p^2 - f_s^2}{f_p} \tag{3.33}$$

to make the comparison of actual devices more convenient [96].

Quality factor, Q

When a stretched spring is released, it will contract past its natural relaxed point, ending in a compressed state; the process then reverses, returning the spring to a stretched state, at which point it reverses again, and so on, yielding a simple mechanical oscillator. For an ideal spring, this periodic extension and contraction would occur *ad infinitum*; in a real spring, as with the bouncing ball that rises less on each hop, every period has loss and every period shows a decrease in amplitude. The magnitude of this loss can be normalized by comparing it to the fully stretched (or fully compressed) mechanical potential energy exhibited by the spring before initial release; this gives the fraction of stored energy that is lost in each full period, and the relationship can be applied to mechanical or electrical domains. Traditionally, this metric is reported as the inverse of the loss ratio, and it is defined as the quality factor Q of a resonator

$$Q = 2\pi\frac{\text{maximum energy stored}}{\text{energy lost per cycle}} \tag{3.34}$$

where the factor 2π stems from its periodic definition.

Experimentally, the quality factor is determined using one of several approximate definitions. Most commonly, Q is approximated from from the width of the resonance peak, which derives from the parallel RLC resonator definition as

$$Q = \frac{R}{\sqrt{L/C}} = \frac{\omega_\circ}{\Delta\omega} \tag{3.35}$$

where $\Delta\omega$ is the -3 dB bandwidth of the admittance curve [97]. The equivalent quality factor can also be calculated from the impedance phase response slope as

$$Q = \frac{\omega_\circ}{2} \left| \frac{\partial\phi}{\partial\omega} \right|_{f_\circ} \tag{3.36}$$

which is evaluated at the resonance frequency [49]. Both (3.35) and (3.36) can be evaluated at either series or parallel resonance, which for most BAW devices will not yield equivalent quality factors.

Finally, Su *et al.* have derived an approximation for series quality factor that is particularly convenient for calculation from measured scattering parameters as

$$Q_s = \frac{\omega_s/\omega_p}{1-(\omega_s/\omega_p)^2} \sqrt{\frac{(1-|S21_{min}|)}{|S21_{min}|} \frac{1-|S11_{min}|}{|S11_{min}|}}. \tag{3.37}$$

In practice, these methods for calculating Q yield similar results when applied to FBAR devices, and the most convenient for a particular workflow can be chosen.

Quality factor, coupling, and the development of piezoelectric oscillation

Both quality factor and coupling coefficient can be used to develop an intuition for the operation of a sustained piezoelectric oscillation. For a real system, $k^2 < 1$, and only a fraction of applied electrical energy will be transduced into mechanical energy. For the portion of the energy that does couple into a mechanical strain, for $Q > 1$ the energy will remain in the resonator for more than one cycle. In this manner, energy contributed in small amounts each cycle add to the total stored energy, and the oscillation amplitude builds.

3.5.4 Piezoelectric material systems

As described in Section 3.5.1, the piezoelectric effect arises in crystal structures that lack inversion symmetry. For BAW applications, a variety of material systems are commonly

employed. Quartz has found widespread use for crystal resonators, where its low thermal expansion coefficient enables its use as a stable frequency reference [16]. Lead zirconate titanate (PZT) is a ceramic material with a high dielectric constant and a large electromechanical coupling coefficient (when polled), and it is used in the manufacture of capacitors and ultrasonic transducers. It has also been used to build high-power, high-efficiency piezoelectric transformers [98]. Polyvinylidene fluoride (PVDF) is a fluorinated polymer that exhibits a strong piezoelectric effect and can be used to make flexible tactile sensors and strain gauges [99]. For thin-film devices, there is a class of crystalline material that is particularly useful, which includes both zinc oxide and aluminum nitride. These materials are straightforward to deposit in a laboratory environment at sub-micron thickness, crystalize preferentially to a piezoelectric form, and need not be polled.

Zinc oxide

Zinc oxide (ZnO) is a large bandgap semiconductor that is used extensively in industrial applications; it can be found in paint, sunscreen, concrete, and a variety of packaged foods [100]. More recently, it has gained traction in electronic applications, where it can be used as a semiconductor or doped and used as a transparent contact material where indium tin oxide (ITO) has been the dominant material system. In its most common form, zinc oxide exists in a hexagonal Wurtzite structure, depicted in Figure 3.6. For thin-film applications, zinc oxide is deposited by RF sputter deposition from a ceramic target.

As a sputtered film, zinc oxide usually forms a polycrystalline structure of hexagonal columns with the *c*-axis normal to the receiving substrate. This axis is also the dominant piezoelectric axis, along which transverse longitudinal and shear waves propagate.

Sputter deposition

Many of the materials used for FBAR fabrication are deposited by sputtering, a common tool for physical vapor deposition (PVD). An inert gas, such as argon, is used to excite a plasma in the presence of an accelerating voltage. Positively charged gas ions are accelerated

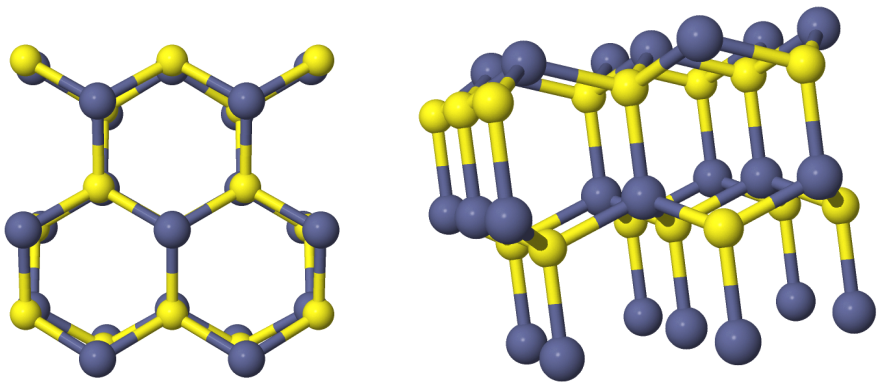

(a) (b)

Figure 3.6: In its most common form, zinc oxide forms a hexagonal Wurtzite structure, shown here. In 3.6(a), the view is end-on, with the z-axis coming out of the page; from this angle, the hexagonal structure is clearly visible. In 3.6(b), the view is with the z-axis oriented up, in the plane of the page; the lack of inversion symmetry is clearly visible, which gives rise to a bulk piezoelectric effect. *Images rendered in Jmol* [101].

and impacted against a solid target source material. This impact ejects atoms from the target source, which re-deposit on surrounding surfaces.

Unlike evaporation, sputtering releases atoms from a source material by momentum exchange, allowing deposition of materials that are difficult to melt; this includes materials that decompose, such as ceramics, and materials with high melting temperatures, such as tungsten. Thin-films of zinc oxide, aluminum nitride, tungsten, and silicon dioxide can all be deposited by sputtering.

Sputter yield can be increased by the addition of a strong magnetic field at the target surface. This field confines secondary electrons near the target surface, enhancing plasma excitation at the source material [102]. This is referred to as a magnetron sputtering setup. Additionally, the use of an alternating voltage for plasma excitation, typically in the mega-hertz regime, allows deposition from insulating source materials. FBAR structures reported here have been deposited in an RF magnetron sputter system, and nominal deposition conditions are listed in Table 3.1. The primary process variables are inert gas concentration and applied RF power, both of which influence sputter yield, deposition rate, and isotropy of the deposited film. A detailed, quantitative analysis may be found in [102].

Table 3.1: Typical process parameters for films deposited by RF magnetron sputter deposition in this work. These parameters will be specific to a particular sputtering system.

Material	**Process Gas**	**Pressure** [mTorr]	**RF Power** [W]	**Depostion Rate** [$\AA$/s]
Silicon dioxide	Ar	2	250	0.25
Tungsten	Ar	10	300	1.50
Zinc oxide	9:1 Ar:O_2	2	300	0.40

3.5.5 X-ray diffraction of piezoelectric thin-films

The piezoelectric effect is difficult to measure directly, especially in thin-film devices, where typical deflections are smaller than one angstrom. For bulk materials this can be measured in a macroscopic block of material [103]. For thin-films, piezoelectric constants have been quantified for a limited set of materials using strained cantilevers and optical interferometry at sub-angstrom resolution [104, 105]. For process development, it is generally more convenient to confirm a particular crystal orientation and infer an intrinsic piezoelectric property.

X-ray diffraction (XRD) is used to deduce the orientation and lattice spacing characteristics of a crystalline material. Incident monochromatic x-rays scatter elastically in a crystalline solid. The scattered waves form interference patterns as they exit the crystal, due to the periodicity of the atomic scattering centers. This is described by Bragg's Law as $\lambda = 2d \cdot sin(\theta)$, where λ is the x-ray wavelength, d is the distance between crystal planes, and θ is the angle of the incident and scattered x-rays relative to crystal normal [106]. By measuring the angle of diffraction maxima and minima, crystal orientation and lattice spacing may be determined; related techniques are employed to measure residual strain and grain size. Diffraction patterns are not unique, and XRD is used to confirm or to quantify suspected or known materials.

In this work, X-ray diffraction is employed to determine the crystal structure of sputtered piezoelectric films. Zinc oxide, for example, may form the hexagonal wurtzite structure in Figure 3.6, but it may also crystalize into a cubic zincblende structure, which is not piezoelectric [100]. For the wurtzite arrangement, the crystal structure will create

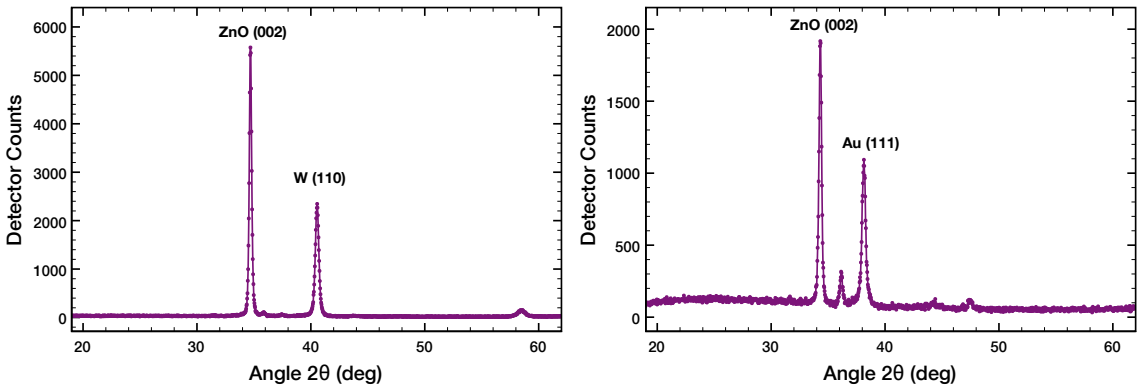

(a) (b)

Figure 3.7: Glass substrates have been coated with a metal seed layer followed by RF sputtered zinc oxide. The scan in (a) is of zinc oxide on sputtered tungsten, and the scan in (b) is of zinc oxide on evaporated gold. The peaks at 34.2°, 38°, and 41° correspond the the (002) zinc oxide plane, the (111) gold plane, and the (110) tungsten plane, respectively [107, 108].

a diffraction maximum at 2θ=41°, where 2θ measurements represent the angle between the incident and scattered x-rays, each of which is at an angle θ to the film surface [107]. Measured angle spectra are taken on an Inel X-ray Diffractometer, examples of which are shown in Figure 3.7.

3.5.6 Optimization of zinc oxide deposition for piezoelectric orientation

The preferred orientation of zinc oxide for FBAR fabrication is as a *c*-axis oriented piezoelectric Wurtzite structure, as detailed in Section 3.5.4. Process variables for film deposition are tuned improve crystal quality, which may be characterized by XRD peak width, surface roughness, grain size, and visual inspection.

Substrate temperature during film deposition

Substrate heating can strongly effect the outcome of RF sputter deposition. As ejected source molecules reach the substrate surface, their ability to move and settle before being confined to a location in the growing film layer is influenced by the temperature of the receiving bulk. For zinc oxide, temperature-based improvement in crystal orientation has been previously demonstrated, where substrate heating during both the metallic seed layer

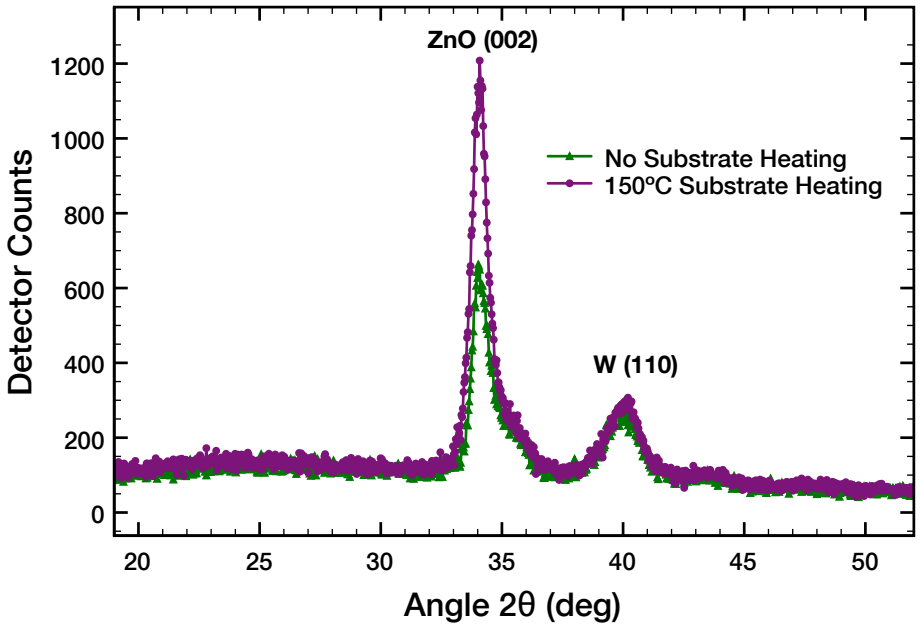

Figure 3.8: Comparison of heated and non-heated RF magnetron sputter deposition on zinc oxide on a thin tungsten seed layer. Both techniques yield *c*-axis oriented wurtzite zinc oxide, but crystallinity improves measurably with substrate heating.

deposition and of the zinc oxide layer deposition independently improved preferred *c*-axis growth [109]. Chang *et al.* speculate that the former is due to improved crystallinity of the metallic seed layer, which in turn promotes crystallinity in the zinc oxide layer.

For the zinc oxide process developed in this work, crystal orientation was improved by mild substrate heating, as assessed by XRD. This is achieved unintentionally in a short-throw deposition setup, where the substrate is close to the sputter source and is heated by the plasma. Early films were deposited in this manner, with a target to source distance of approximately four inches. More recently, films have been deposited in a sputter system with a target to source distance of more than 10 inches. In this setup, marked improvement in *c*-axis crystal orientation was observed with substrate heating, with an optimized temperature of approximately 150°C. XRD spectra shown in Figure 3.8 demonstrate this phenomenon. Susbtrate temperatures above 200°C were not employed, as limited by the photolithographic processing; photoresist becomes a permanent fixture at higher temperatures. In future work, an etch-based process flow could enable higher substrate temperatures during deposition,

limited only by the CMOS back end of the line (BEOL) layer stack.

Process gas mixture

Non-elemental materials may lose stoichiometry during sputter deposition, especially in oxides and nitrides; as the particles are ejected from the source target, released oxygen or nitrogen may be dissipated before recombining at the substrate, leading to a deficiency in the resulting film. For zinc oxide deposition, an oxygen partial pressure was employed to mitigate this effect. In a pure argon environment, films had low resistivity and a silvered appearance, both of which are attributed to zinc enrichment. Argon to oxygen ratios from 9:5 to 9:0 were tested. A ratio of 9:1 was chosen for device growth, which yields transparent, high resistivity films.

Zinc oxide metallic seed layer

For the basic FBAR structure depicted in Figure 3.2, the bottom electrode serves as the seed layer for the piezoelectric bulk layer. Crystal orientation of the piezoelectric layer depends strongly on the surface morphology of the underlying surface [109]. Zinc oxide deposition was tested on tungsten, gold, chrome, silver, and silicon dioxide. Both tungsten and gold yielded strong *c*-axis zinc oxide orientation, which is attributed to their own crystallinity, as seen in the XRD spectra of Figure 3.7. Both of these metals have been employed as bottom electrodes.

3.6 Mechanical isolation of thin-film resonators

In the simplest FBAR example of Figure 3.2, no reference is made to mechanical isolation. In practice, excitation of a sustained mechanical oscillation requires unhindered movement of the resonant structure. This can be accomplished by having both faces in air or vacuum, or by using a solid acoustic reflector. This section describes both methods.

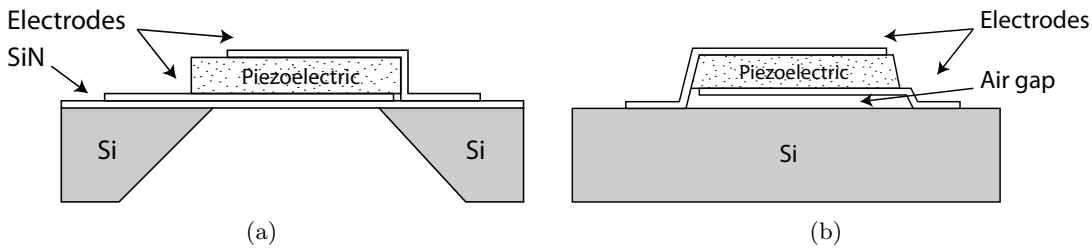

Figure 3.9: Illustration of released FBAR structures for mechanical isolation of the resonator. A partially released resonator on a nitride membrane in (a) is formed by backside etch, and the air gap structure in (b) is formed by an undercut etch.

3.6.1 Released resonator structures

Thinned support cavities

A partially released FBAR structure is fabricated by backside thinning of the build support structure [30, 74]. First, a silicon-nitride etch stop layer is deposited on a silicon substrate by chemical vapor deposition (CVD), and the silicon substrate is etched with potassium hydroxide to form a released silicon nitride membrane. An FBAR structure is built on the thin supporting membrane, as depicted is Figure 3.9(a). After fabrication, the nitride membrane can be further thinned with reactive reactive ion etching.

Zhang *et al.* have demonstrated operation of such devices in a liquid environment, where the thinned nitride was exposed to water and retained a quality factor of 250 [30]. This isolation method is limited by the mechanical loading introduced by the nitride layer, and it cannot be used for dense device arrays or for monolithic CMOS fabrication.

Undercut membrane release

Mechanically isolated FBAR structures can also be formed through undercut, in which a cavity is etched beneath an extant resonator. Typically, the fabrication includes the deposition of a sacrificial oxide or nitride upon which the FBAR is built; this layer is then removed with a wet or dry etch to open an air gap beneath the completed structure [87,110], yielding a released structure similar to that illustrated in Figure 3.9(b). This process is commonly employed for standalone resonator fabrication, after which resonators can be

combined with a CMOS substrate through standard package-level techniques. It has also been been demonstrated by Dubois *et al.* for monolithic FBAR integration with a BiCMOS process [110]. The advantages of this technique are offset by the processing difficulty of an undercut process and the fragility of a suspended membrane.

3.6.2 Solidly mounted resonator structures

Thin-film resonators can be mechanically isolated, yet structurally solid, though the use of an acoustic mirror. This forms a solidly mounted resonator (SMR) device, and it is the most physically robust FBAR topology [111]. Where membranes can be fragile and subject to mechanical shock or fracture due to processing stress, every layer of an SMR resonator is supported by and attached to another underlying layer. FBAR devices used in this work employ an SMR structure.

Acoustic Bragg stack theory and simulations

An acoustic mirror is formed by alternating layers of high and low acoustic impedance, analogous to a distributed Bragg reflector in optical applications [112]. In this case, however, its reflection bandwidth occurs at acoustic wavelengths and confines mechanical energy within the bulk piezoelectric layer. In addition to offering a mechanically isolating, solid support for an FBAR device, an acoustic resonator can also act as a filter, reflecting only the target resonant frequency and dissipating overtones and spurious resonant modes [113]. In many cases, this is a desirable effect. The behavior of an acoustic mirror derives from periodic impedance mismatches at layer boundaries, as proposed by Newell in 1965 [114].

The acoustic characteristics of several relevant materials are shown in Table 3.2. Because the entire FBAR structure is part of the acoustic path of a propagating wave, characteristics of the piezoelectric bulk layer, metallic contacts, underlying substrate, mechanical isolations, and all associated layers must be considered. For an acoustic reflector formed by a periodic stack of thin-film materials, we are in particular interested in the reflection of a propagating acoustic wave at each layer boundary. This can be described

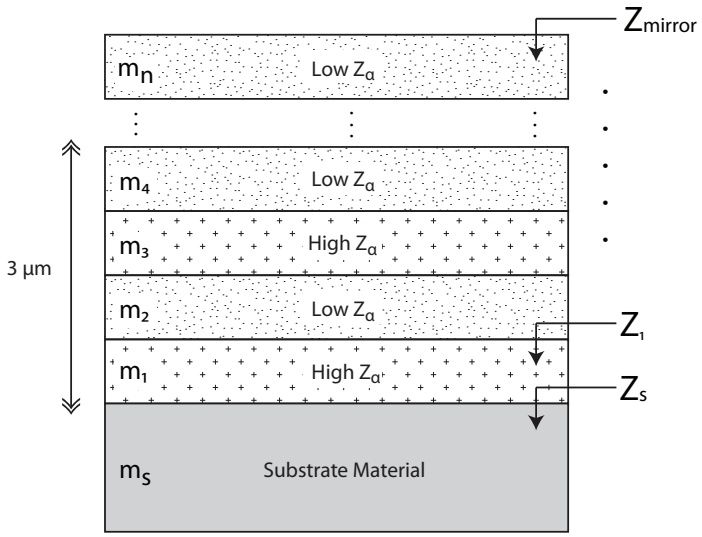

Figure 3.10: A periodic acoustic reflector is formed by alternating layers of high and low acoustic impedance materials. Each layer is tuned to a quarter wavelength of the target resonator frequency. Mechanical energy is reflected back toward the piezoelectric layer.

analytically by several treatments, including the use of scattering matrices, wave-transfer matrices, and transmission line theory [115–118]. The transmission theory approach is described here.

Consider the basic multi-layer reflector structure shown in Figure 3.10. For mechanical isolation, we are interested in the acoustic reflection at the boundary between the piezoelectric layer and the combined structure below it; maximum reflection around the resonator frequency will confine energy within the piezoelectric layer every cycle, increasing the effective resonator quality factor.

For the structure shown in Figure 3.10, each layer has both a thickness, which determines the propagation distance through the layer, a phase velocity, determining the acoustic wavelength within the layer, and a characteristic acoustic impedance. For propagating waves, electrical or mechanical, an impedance mismatch yields a reflection. The multi-layer structure forms a cascaded transmission line, where each layer is a line segment with a known characteristic impedance and length. The impedance seen at the piezoelectric-mirror boundary can be calculated by recursively applying the transmission line equation at each boundary. This is the same equation used for electrical wave propagation along a

Table 3.2: Physical parameters of materials commonly employed for acoustic resonator fabrication. Acoustic velocity and acoustic impedance are calculated from listed constants.

Material	**Density**	**Longitudinal Stiffness**	**Acoustic Velocity**	**Acoustic Impedance**
	ρ $[g/cm^3]$	c_{11} $[N/m^2]$	V_α $[m/s]$	Z_α $[W/m^2/(m/s)^2]$
Zinc Oxide (ZnO)	5.68	20.97×10^{10}	6,100	34.5×10^6
Aluminum Nitride (AlN)	3.26	39.7×10^{10}	11,000	36.0×10^6
Aluminum (Al)	2.7	11.1×10^{10}	6,400	17.3×10^6
Gold (Au)	19.3	20.7×10^{10}	3,300	63.2×10^6
Tungsten (W)	19.2	58.1×10^{10}	5,500	106×10^6
Silicon (Si)	2.33	16.6×10^{10}	8,400	19.7×10^6
Silicon Dioxide (SiO_2)	2.32	7.2×10^{10}	5,720	12.6×10^6

transmission line [119], and it is described by

$$Z_{in} = Z_\alpha \frac{Z_L cos(\beta\delta) + jZ_\alpha sin(\beta\delta)}{Z_\alpha cos(\beta\delta) + jZ_L sin(\beta\delta)} = Z_\alpha \frac{Z_L + jZ_\alpha tan(\beta\delta)}{Z_\alpha + jZ_L tan(\beta\delta)}. \tag{3.38}$$

Applied at a layer boundary, Z_α is the acoustic impedance of the propagation layer, Z_L is the acoustic impedance of the material past the boundary, δ is the thickness of the propagation layer, and β is the phase constant in the propagation layer

$$\beta = k = \frac{2\pi}{\lambda_\alpha} = \frac{\omega_\alpha}{V_\alpha}. \tag{3.39}$$

Referring to the diagram in Figure 3.10, the transmission line equation is applied first at the m_1 and m_s boundary, assuming a wave propagation from m_1 into the substrate m_s. The calculated impedance then serves as the Z_L for m_2, and so on up the stack until m_n is reached, yielding a calculated impedance Z_{mirror} looking into the entire mirror stack. The reflection coefficient Γ_{mirror} can then be calculated using a standard impedance mismatch equation [119]

$$\Gamma_{mirror} = \frac{Z_{mirror} - Z_{piezo}}{Z_{mirror} + Z_{piezo}}. \tag{3.40}$$

This process can be applied to consider the effects of layer number, layer thickness, layer material, and thickness variation in the overall performance of the mirror.

The effect of layer number can be seen in Figure 3.11, using the material constants shown in Table 3.2 for a tungsten and silicon dioxide reflector. This has been simulated

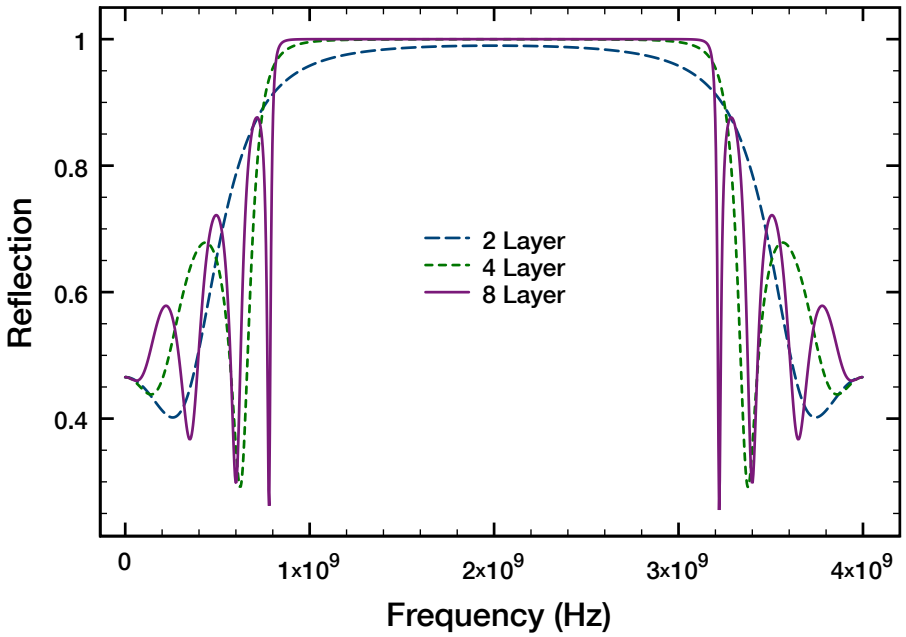

Figure 3.11: Simulation of a periodic acoustic reflector made from alternating layers of tungsten (6500 $\mathring{A}$) and silicon dioxide (7500 $\mathring{A}$). The large impedance mismatch between the two materials yields a strong, broadband reflection with only a few mirror layers.

using a MATLAB script to implement the recursive transmission line equation. Because of the large impedance mismatch of these two materials, even a single pair yields a reflection coefficient greater than 90% and a broad reflection band.

Once the simulator has been implemented, it is straightforward to explore critical design parameters. For example, material selection strongly affects mirror behavior. For the simulated results in Figure 3.12, the layer stack comprises alternating layers of silicon dioxide and zinc oxide. The impedance mismatch of this pairing is not as large as for tungsten, yielding both a decreased reflection coefficient and a narrowed reflection band. In some instances, a narrowed reflection band is desirable for filtering spurious resonant modes. For this work, however, the improved few-layer reflection and broad reflection band are preferred for ease of fabrication and standardization; with a wide reflection band, a single batch of fabricated reflectors can be used for a variety of resonant frequencies.

The large-magnitude broadband reflection also eases the required tolerances on layer thickness within the mirror, especially for buried layers. This is advantageous for practical

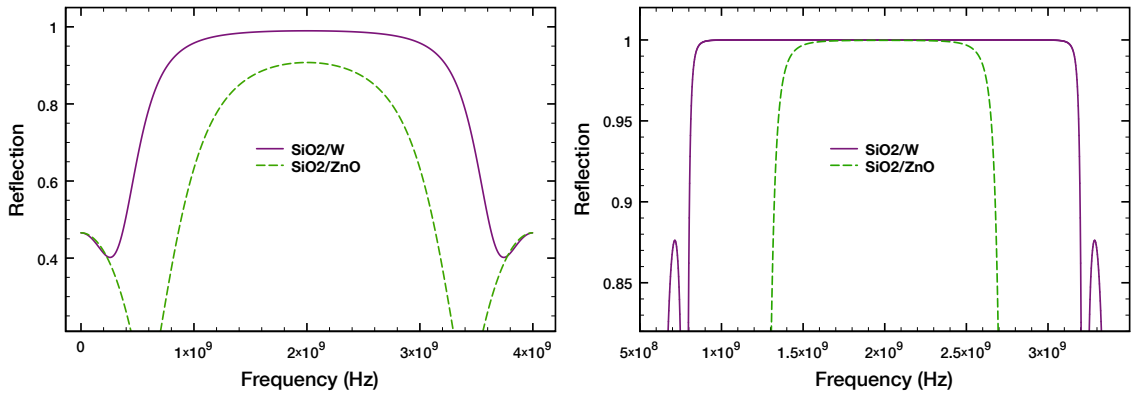

(a) (b)

Figure 3.12: Simulated comparison of acoustic reflection for silicon dioxide paired with either tungsten or zinc oxide. Both reflection coefficient and reflection bandwidth are increased with tungsten. The structure in (a) has two reflector layers, and the structure in (b) has eight reflector layers.

fabrication, where very thick layers are, perhaps counterintuitively, difficult to deposit with tight thickness control. Additionally, sputter deposition is inherently non-uniform, and thickness variation of $\pm 10\%$ has been measured from substrate center to substrate edge on systems used for this work. The thickness tolerance for the tungsten layers is simulated in Figure 3.13. Reflection for a four-layer tungsten and silicon dioxide $\lambda/4$ reflector is shown, and the thickness of the tungsten layers has been alternately increased and decreased by ten percent. The reflection coefficient is unaffected in the reflection band, and variations in band edge are small compared to reflector bandwidth. Also visible is the increasing influence of layer mismatch at higher frequencies. This is expected, where the variation represents a larger fraction of phase length within the material.

3.7 Passive resonator fabrication and characterization

3.7.1 Device geometry

Test FBAR structures are fabricated on glass or silicon for two-port characterization with a vector network analyzer (VNA). This requires that test structures are built with an RF-probe compatible electrode layout. For the devices shown here, a basic ground-signal-ground

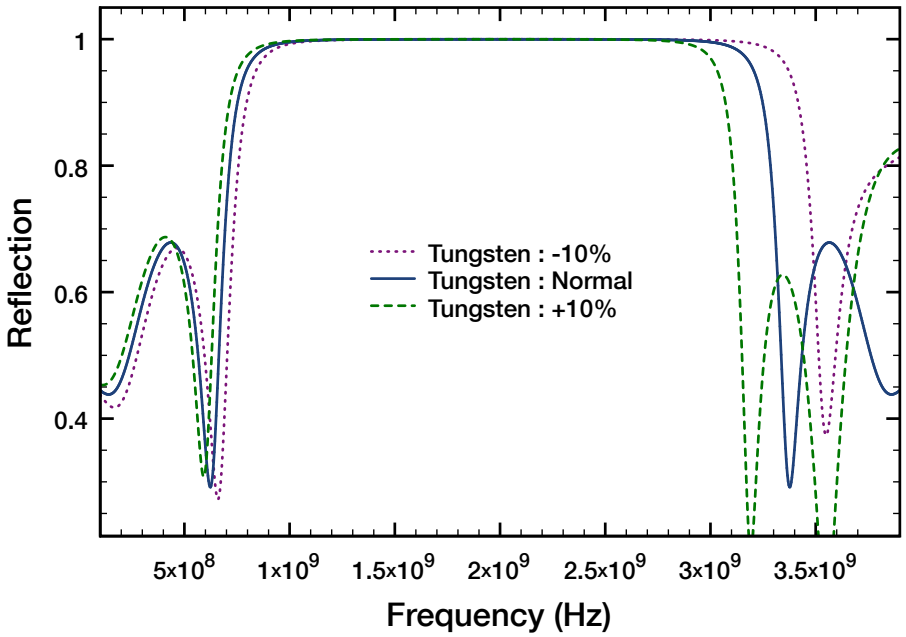

Figure 3.13: Simulation of a periodic acoustic reflector made from alternating layers of tungsten (6500 $\AA$) and silicon dioxide (7500 $\AA$). The tungsten thickness has been alternately increased and decreased by ten percent, which has negligible effect on reflection at the frequencies of interest.

(GSG) topology is chosen, with a probe pitch of 150 μm. This conforms with standard high-frequency GSG test probes for characterization. Excluding the acoustic reflector, a basic FBAR device is fabricated in three successive photolithographic layers: bottom electrode, piezoelectric layer, and top electrode. For the GSG arrangement, ground electrodes can be placed in either electrode deposition step. The FBAR active area is formed by electrode overlap, and the piezoelectric layer is made larger to prevent shorting of top and bottom electrodes. This general arrangement is shown Figure 3.14.

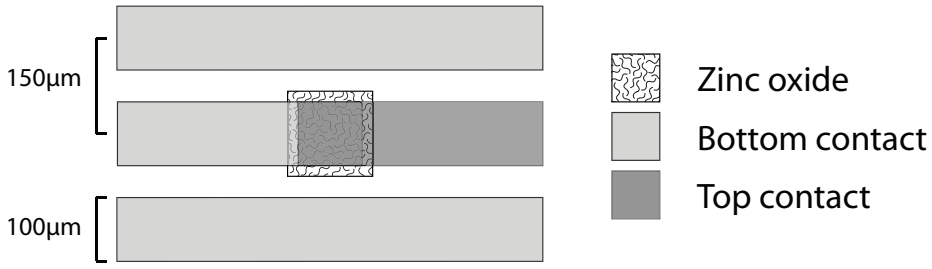

Figure 3.14: Layout of FBAR structures with ground-signal-ground arrangement. Three separate photolithographic masks are required for the fabrication.

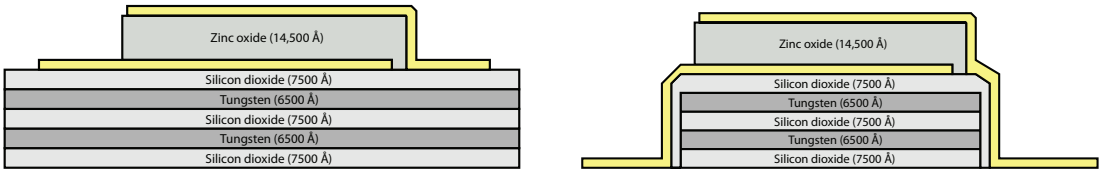

Figure 3.15: Two basic topologies of FBAR devices. The device in (a) is built atop a blanket acoustic reflector, while the device in (b) has an individually patterned acoustic mirror.

Fabrication of devices for characterization is simplest on large-area, blanketed acoustic reflectors. Batches of reflectors can be built on a large substrate and sectioned for use as FBAR build substrates. For direct comparison with CMOS-integrated resonators, however, devices are built with individual acoustic reflectors. These structures more accurately represent the parasitics and losses associated with on-chip devices. Both of these designs are illustrated in figure 3.15.

Mirror structures have been designed to center around 2 GHz, such that they cover the spectrum from 1 GHz to 3 GHz with a high reflection coefficient, as shown in Figure 3.11. In most device batches, a four-layer mirror (two pairs) is built, balancing desired maximum reflection with fabrication turnaround time.

3.7.2 Fabrication process

Resonator fabrication proceeds in an additive fashion, following a standard photolithographic progression, as depicted in Figure 3.16. For structure definition, a bilayer resist process is used, in which a commercially available polymer lift off resist (LOR30B, Microchem Corp.) is applied and spun to final thickness of 4-5 μm. This is followed by the application of Shipley S1813 (Microchem Corp.) at a thickness of 1.3 μm, which is exposed by hard contact under a UV mask aligner and developed with AZ 300 MIF (AZ Electronic Materials). After patterning, alternating layers of silicon dioxide and tungsten are deposited by sputter deposition, ending with a tungsten top layer.

Each tungsten layer is targeted at 6500 $\mathring{A}$; a 5 nm chrome adhesion layer is deposited from a thermal source, followed by tungsten deposition at 250 W in an RF magnetron

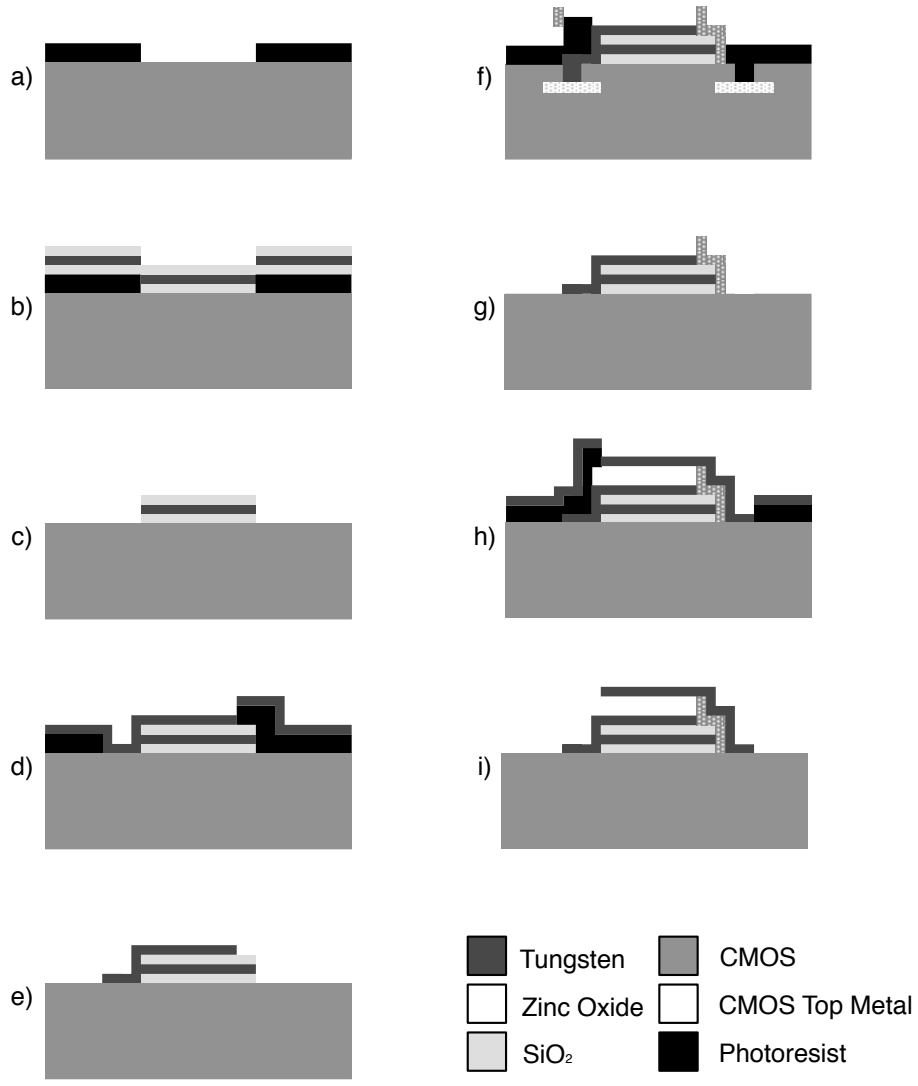

Figure 3.16: Process flow diagram for fabrication of solidly mounted FBAR devices. Photoresist is used to pattern a window for an isolated acoustic reflection (a), and alternating layers of tungsten and silicon dioxide are deposited (b) and lifted off (c). Photoresist is used to pattern the bottom contact (d), which is deposited and lifted off (e). The piezoelectric layer is photolithographically defined and deposited (f) and lifted off (g). Finally, the top contact is patterned and deposited (h) and lifted off (i) to reveal a completed, solidly mounted FBAR structure.

sputter system from a three-inch diameter elemental tungsten target. The sputter deposition is performed in an argon atmosphere at a pressure of 10 mTorr and a gas flow rate of 10 sccm, which yields a deposition rate of approximately 1 $\mathring{A}/s$.

Silicon dioxide layers are deposited without any adhesion layer. The target thickness is 7500 $\mathring{A}$, equivalent to a quarter wavelength in the layer for a 2 GHz acoustic wave. Each silicon dioxide layer is deposited from a three-inch diameter SiO_2 target by RF magnetron sputter deposition in a pure argon environment. In this case, 250 W power is applied with an argon pressure of 2 mTorr at a flow rate of 10 sccm for a deposition rate of approximately 0.3 $\mathring{A}/s$. For both tungsten and silicon dioxide sputter depositions, thickness is measured in real time by a quartz crystal thickness monitor, and film thickness is typically within $\pm$10% of the target thickness.

Lift-off proceeds in heated Remover PG solvent (Microchem Corp.), after which the process is repeated for the top silicon dioxide layer. This layer serves both as top reflector layer and as an insulating passivation to prevent electrical shorting through the tungsten layers. The bottom electrode is defined in the same manner, with a 5 nm chrome adhesion layer and 100 nm of gold by electron-beam evaporation. For zinc oxide deposition, the patterned substrate is heated to 150°C, and sputter deposition proceeds in 9:1 Ar:O_2 at a pressure of 2 mTorr at 250 W. Finally, the top contact is patterned and deposited, yielding a complete, standalone acoustic resonator.

A cross-section electron micrograph of a fabricated FBAR can be seen in Figure 3.17(b). Here, the alternating metal and oxide layers are clearly delineated. Also clear is a visible variation in layer thickness, which is attributed to poor crystal monitor tracking for such thick films. While tighter control over this thickness is desirable, the broadband reflection characteristics detailed in Section 3.6.2 indicate that precise thickness control is not required.

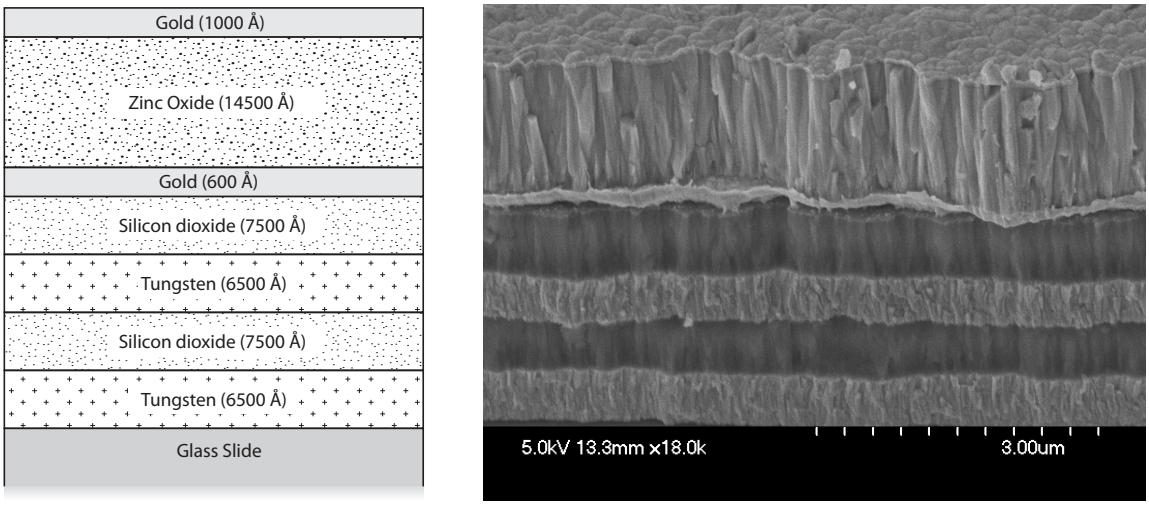

(a) (b)

Figure 3.17: Tilted scanning electron micrograph of a fabricated FBAR device stack cross-section. Columnar zinc oxide is on top, and alternating silicon dioxide and tungsten layers can be seen beneath.

Improved lift-off of thick thin-film layers

The process flow described above employs a bilayer photoresist process, which was developed to overcome poor yield and impaired device performance seen with single-layer photoresist processes. For a lift-off process, film continuity at the boundary of the photoresist mask causes tearing, which increases edge roughness. This problem is significantly amplified when very thick or very conformal films are deposited; additive FBAR fabrication requires both. Edge roughness as a result of tearing can lead to the wings and raised sidewall effects seen in the scanning electron micrographs (a) and (b) of Figure 3.18, and to the open circuit and high-resistance electrode paths in (c) and (d).

A bilayer photoresist uses a first lift-off-resist layer that is not photosensitive but which has an etch rate in developer comparable to exposed negative photoresist. This rate is tunable by bake temperature. Normal photoresist is patterned on top, and the development step creates an undercut in the LOR layer. The resulting ledge can prevent the deposition of a continuous film, leading to clean lift-off. With careful development control, this bilayer combination yields an undercut of several microns. As compared to the devices in Figure 3.18, those shown in Figure 3.19 represent a stark improvement. The

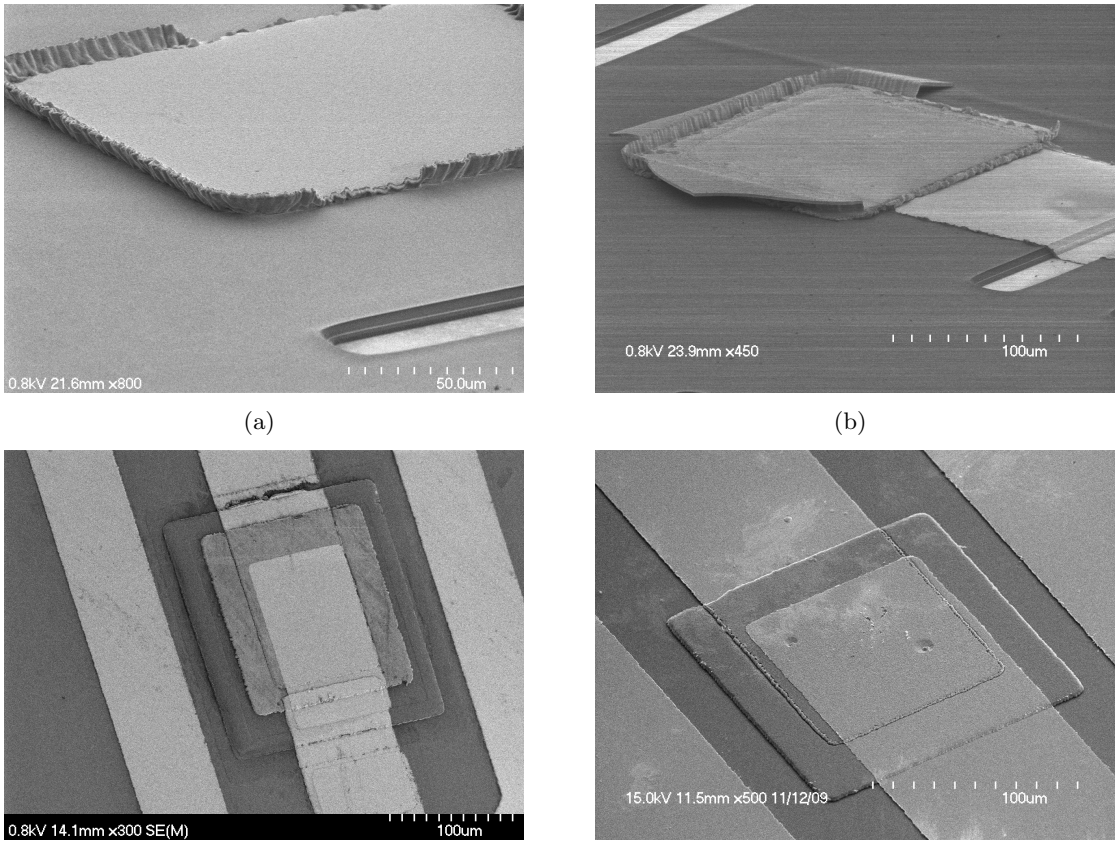

(a) (b)

(c) (d)

Figure 3.18: Lift off with thick photoresist results in rough feature edges. Raised edges are shown in (a), and large wings are shown in (b). These features result in failures like the open contact in (c), and rough edges seen in (d) yield high-resistant contacts at steps.

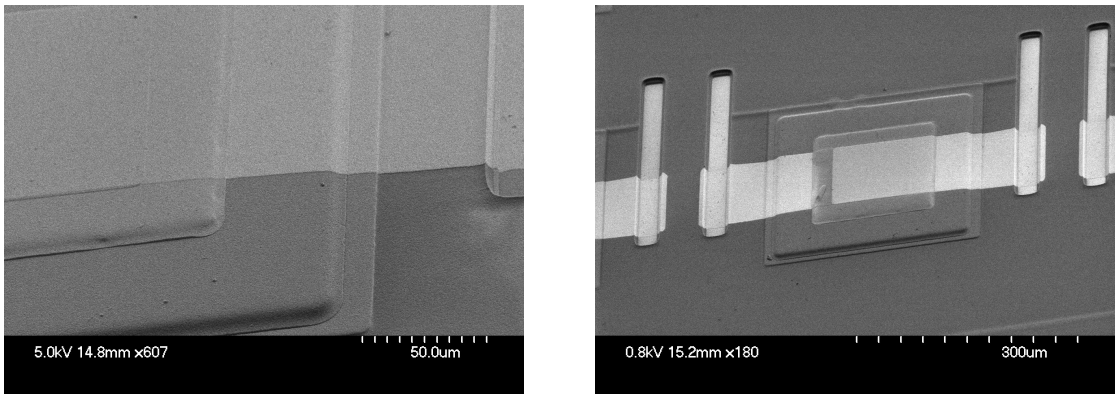

(a) (b)

Figure 3.19: Lift off resist is employed in a bilayer process that allows clean lift off of thick films. Smooth steps are seen in (a) and (b) that improve device yield and performance.

transition to a bilayer process significantly increased both device yield and measured quality factors.

3.7.3 S-parameter electrical characterization

High frequency BAW devices are typically characterized by two-port scattering parameters, or s-parameters, which define the voltage behavior of a two-port linear network [119]. The electrical properties of a fabricated device are fully described by s-parameters over the measured frequency span, allowing for the confirmation of electrical resonance and the calculation of quality factor, electromechanical coupling coefficients, and equivalent circuit parameters. In this section, measured s-parameters are used to characterize individual devices and process variation. In particular, the input reflection described by the magnitude of S11 will have a sharp minimum near the series resonance, which corresponds to a minimum in the input impedance of the device [34].

S-parameters are measured with a vector network analyzer (Agilent N5230A) using GSG high frequency probes (Cascade Microtech), after a 50 Ω short-open-load-through (SOLT) probe calibration procedure. Data are saved to a standard Touchstone file format and processed in MATLAB using custom scripts. For FBAR devices, the input voltage reflection parameter S11 is used to quickly confirm a resonance behavior. Magnitude and phase of a measured device are shown in Figure 3.20(a) and Figure 3.20(b). This device was fabricated on a silicon substrate using the probe layout of Figure 3.14 and the stacked topology in Figure 3.15(b). A minimum in the S11 magnitude confirms a resonance near 1.50 GHz, and the shape of the phase plot indicates the nearby low and high impedance points corresponding to series and parallel resonance in the device. The calculated quality factor for this device is $Q = 305$, which is typical for devices measured on silicon. For devices built on glass, a lower quality factor is observed in the range of 180 to 220, which is attributed to the added roughness of the glass slide as compared to a silicon wafer.

It is often more intuitive to consider the impedance or admittance plots, which can be calculated from the s-parameters. The phase and magnitude of the input impedance for the

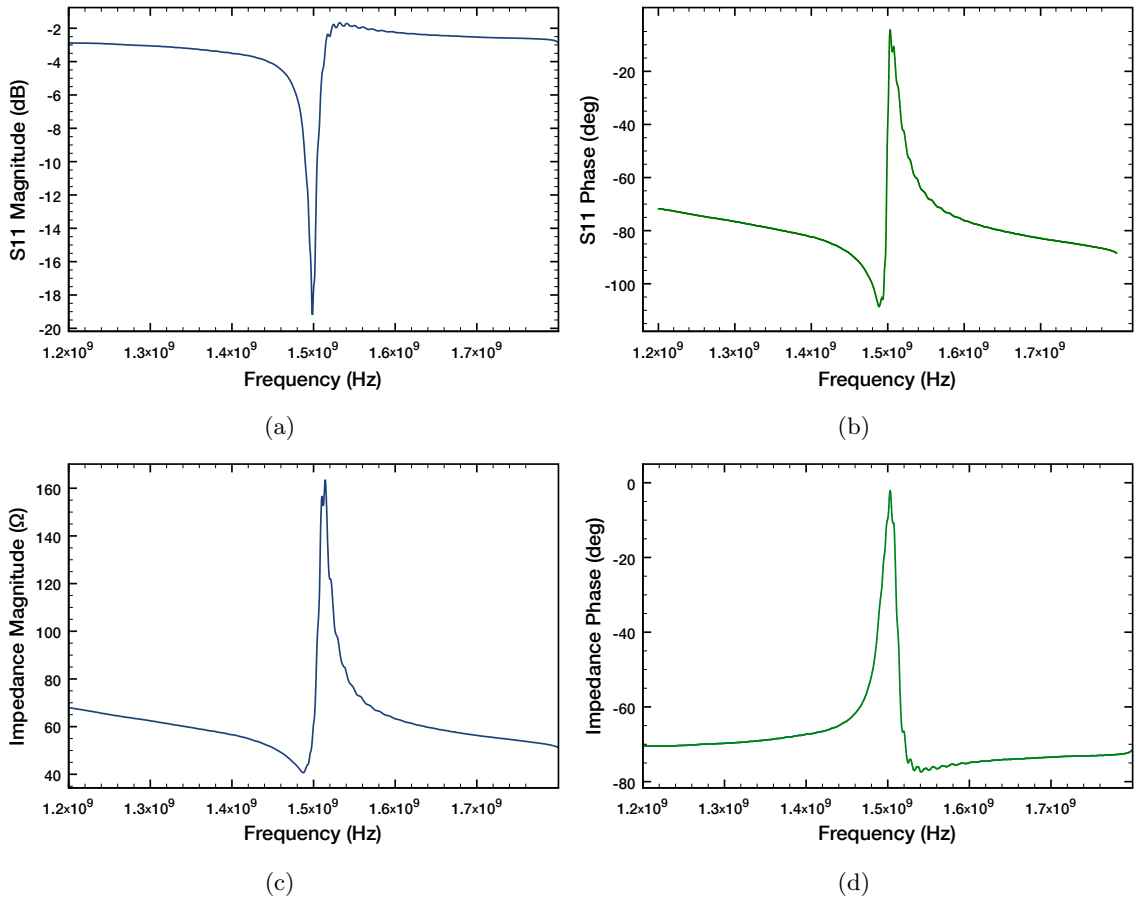

Figure 3.20: Electrical characterization of typical FBAR device. The input reflection S11 is plotted by magnitude (a) and phase (b). This is used to calculate the input impedance, plotted by magnitude (c) and phase (d). Series and parallel resonance frequencies are just below and above 1.5 GHz.

same device is shown in Figure 3.20(c) and Figure 3.20(d). The impedance magnitude maximum and minimum indicated series and parallel resonance frequencies at f_s=1.487 GHz and f_p=1.515 GHz, and nearly identical values are extracted from the admittance magnitude. Using (3.32), the calculated electromechanical coupling is k_t^2=4.2%, and (3.33) yields k_{eff}^2=3.4%.

Resonance may also be identified from the impedance or admittance plotted on a Smith chart, which are shown for two measured devices in Figure 3.21. In a Smith chart representation of the input reflection S11, a resonance appears as a closed circle, and Kaitila *et al.* attribute rippling along the border of this circle to spurious Lamb wave modes in the device [120]. These spurious modes will be discussed in Chapter 4. For the device in

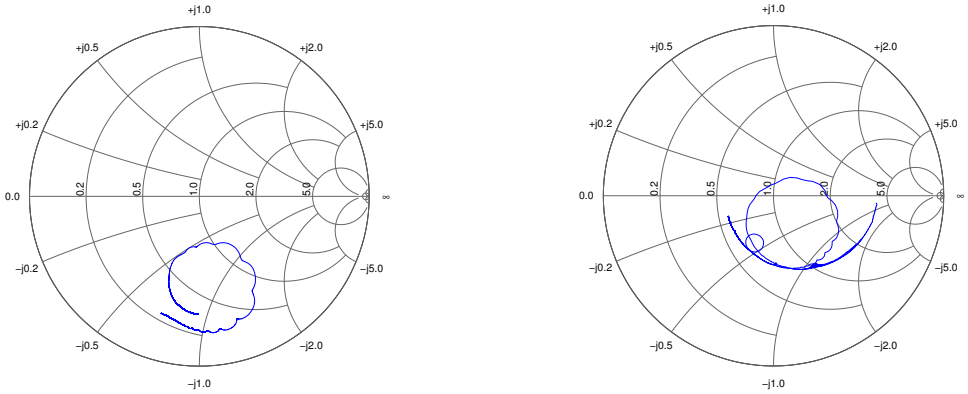

(a) (b)

Figure 3.21: Smith chart representation of measured S11 of basic FBAR structures on a blanket acoustic reflector. The measurement in (a) spans 1.2 GHz to 1.8 GHz and shows one resonance. The measurement in (b) spans 500 MHz to 8 GHz and shows two resonances.

Figure 3.21(a), S11 is measured over a narrow frequency range, from 1.2 GHz to 1.8 GHz, and only a single resonance is visible. The measurement in Figure 3.21(b) was taken on a different FBAR device from 500 MHz to 8 GHz, and two distinct resonances are visible. These correspond to a resonance at 1.48 GHz (big circle) and an overtone resonance at 2.82 GHz (small circle).

3.7.4 Spatial variation of resonant frequency

The effect of small variations in layer thickness of the acoustic reflector was shown in Section 3.6.2 to be negligible on performance, but for the piezoelectric layer it has a pronounced effect. The resonant frequency of a TLM mode resonator, given in (3.20), is entirely determined by the thickness of this layer and the bounding electrodes. This is dominated by the piezoelectric layer, which for 1 GHz in zinc oxide has a thickness exceeding one micron; variations of only a few percent yield tens of nanometers of thickness variation and a corresponding shift in center frequency. This effect can be seen in the measured resonances of many devices over a large substrate area in Figure 3.22.

A 20×20 array of FBAR devices was fabricated on a 2”×2” glass slide with blanketed acoustic reflector. These devices were designed at a target frequency near 1 GHz and

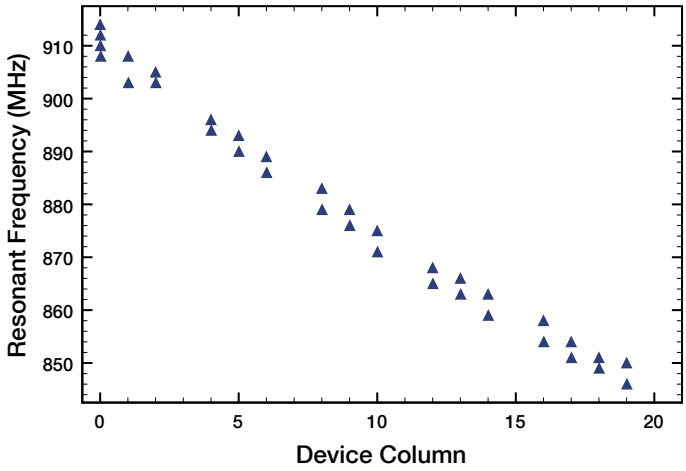

Figure 3.22: Frequency variation is measured across a 2" substrate, which demonstrates a variation of ±2% in nominal resonance. This is attributed to nonuniform deposition thickness of the zinc oxide layer.

fabricated as described in previous sections. Thirty four FBAR devices were measured with a network analyzer (Agilent N5230A) in two rows across 17 columns spanning the substrate, and resonant frequencies were extracted from S11. During sputter deposition of the zinc oxide layer, the substrate was mounted off center of a 6"×6" rotating substrate holder. The resulting devices display resonances from 846 MHz to 914 MHz with a mean of 878.5 MHz and standard deviation of 21.6 MHz, which corresponds to a thickness variation of ±2.4%. This is very good thickness control but a very large frequency variation. A slight variation between the two rows is also visible, which represents a distance on the substrate of approximately 2 mm.

For sensing applications, fabricating FBAR devices to an exact frequency is not critical, where the primary experimental output is a relative frequency shift. For RF applications, however, this is a critical and challenging processing hurdle for the fabrication of filters, and in practice a variety of post-fabrication tuning methods must be employed [49].

3.7.5 Measured resonator topologies

Over the course of this work, many variations in FBAR design and structure have been investigated. Several of the more relevant devices are discussed here.

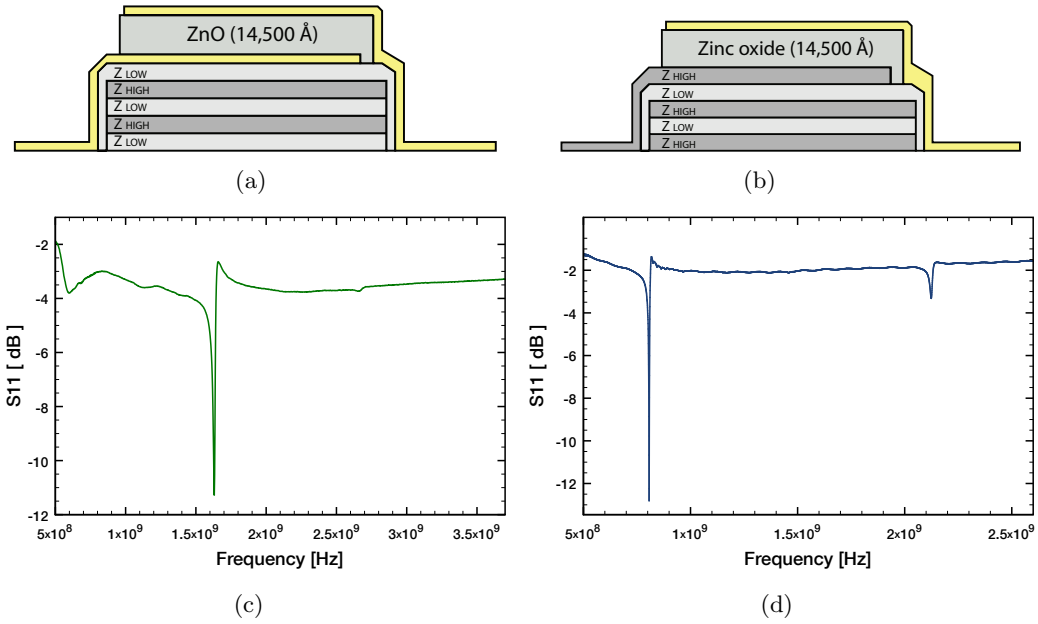

Figure 3.23: Illustration of and measured data from half-wavelength (a,c) and quarter-wavelength (b,d) FBAR devices. This behavior is determined by the top-most layer of the acoustic reflector. For a similar piezoelectric thickness, the device in (a) resonates at 1.6 GHz, while the device in (b) resonates at 800 MHz.

Half-wavelength and quarter-wavelength resonators

For the two FBAR stack topologies illustrated in Figure 3.23, very different resonators are realized. The structure illustrated in Figure 3.23(a) and measured in Figure 3.23(c) is a standard half-wavelength resonator, where the nominal resonance frequency is defined by (3.20). For the discussion of acoustic reflectors in Section 3.6.2, it was assumed that the top-most mirror layer was the lower acoustic impedance material. In this case, the total impedance calculated by (3.38) can be approximated in the reflection band by

$$Z_{\text{mirror}} = \left(\frac{Z_l}{Z_h}\right)^n \cdot Z_s \tag{3.41}$$

for an even number of mirror layers n and substrate acoustic impedance Z_s [96]. This results in a diminishing acoustic impedance as seen by the resonator bottom surface for increasing n, as $Z_l < Z_h$, which yields an unclamped lower boundary as a seen by the resonator. Subsequently, a half-wavelength solidly-mounted FBAR and a released membrane FBAR

have the same resonant frequency for a given piezoelectric thickness.

For the device shown in Figure 3.23(b) and measured in Figure 3.23(d), the top acoustic reflector layer is a thick tungsten layer, which serves both as a mirror layer and as the device bottom contact. In this case the top-most mirror layer has the higher acoustic impedance of the multilayer pair, and the cascaded impedance can be approximated as

$$Z_{\text{mirror}} = \left(\frac{Z_h}{Z_l}\right)^n \cdot Z_s \tag{3.42}$$

which increases with layer number, as $Z_h > Z_l$. In this case, the reflector is seen by the resonator as a very high acoustic impedance, which yields a clamped resonator boundary. The corresponding fundamental resonance will occur for $d = \lambda_\alpha/4$, forming a quarter-wavelength FBAR device [121]. Accordingly, the devices illustrated in Figure 3.23(a) and Figure 3.23(b) have the same piezoelectric thickness, but the corresponding nominal resonances in Figure 3.23(c) and Figure 3.23(d) are measured at 1.6 GHz and 800 MHz, respectively.

Nearly all published FBAR results describe half-wavelength resonator structures, and it can be demonstrated that the attainable quality factor and electromechanical coupling factor are slightly higher for the half-wavelength structure [121]. Both types of devices will be characterized on-chip in Chapter 4.

FBAR shape

For lateral field excitation devices, Dickherber *et al.* have demonstrated a slight degradation in performance for a circular electrode layout, although this effect was not decoupled from area scaling [93]. No similar comparison was found for TLM devices, so thickness-mode FBAR devices with both square and circular device layouts were fabricated in parallel with the isolated mirror topology of Figure 3.15(b). Measured S11 plots are shown alongside the devices in Figure 3.24. These devices show comparable quality factors.

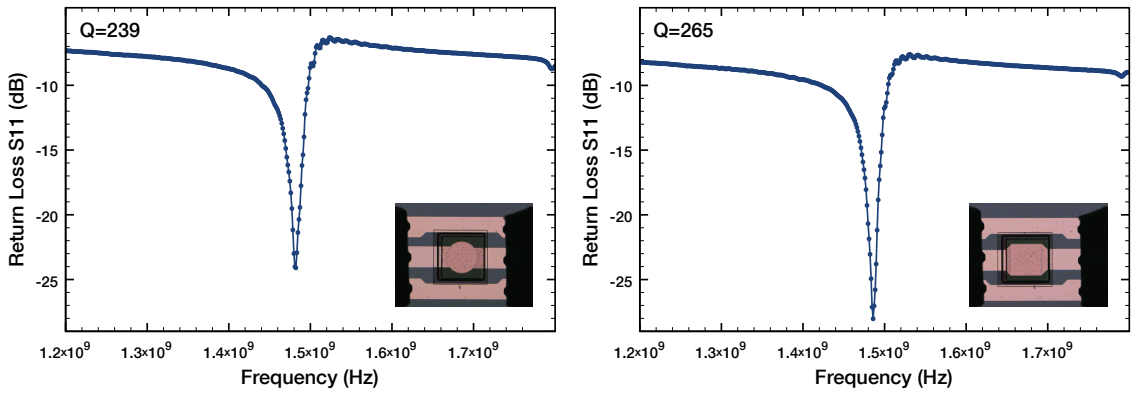

(a) (b)

Figure 3.24: Measured S11 of circular and square FBAR devices on isolated acoustic reflectors. The two device layouts demonstrate comparable performance. It's hip to be square!

3.7.6 Longitudinal FBARs in a liquid environment

A fluid can support longitudinal wave propagation, but unlike like an elastic solid it cannot support shear wave propagation. When a longitudinal mode FBAR has one or more of its surfaces in a liquid environment, longitudinal waves propagate into the fluid layer. This energy is not returned to the piezoelectric cavity, and by definition the resonator Q is degraded.

The quality factor degradation has been verified on several TLM devices fabricated in the manner previously described; these were built with the blanketed reflector topology of Figure 3.15(a) and measured with a network analyzer. After dry characterization, a thinned wooden applicator is used to transfer a water droplet to the FBAR surface, and care must be taken to not interfere with the calibrated GSG probes. Resulting s-parameter data for one such experiment is shown in Figure 3.25.

After the water droplet evaporates, the resonator returns to its high-Q behavior, and the experiment may be repeated. For the device shown, the resonator in air has a Q of 111, and while submerged in a liquid layer the FBAR has a degraded Q of 12. This represents a 10-fold decrease in quality factor. This is similar to the degradation reported by Zhang *et al.* for their submerged longitudinal mode FBAR device [30]. While such devices may be used for sensing, the absolute sensitivity and measurement resolution will

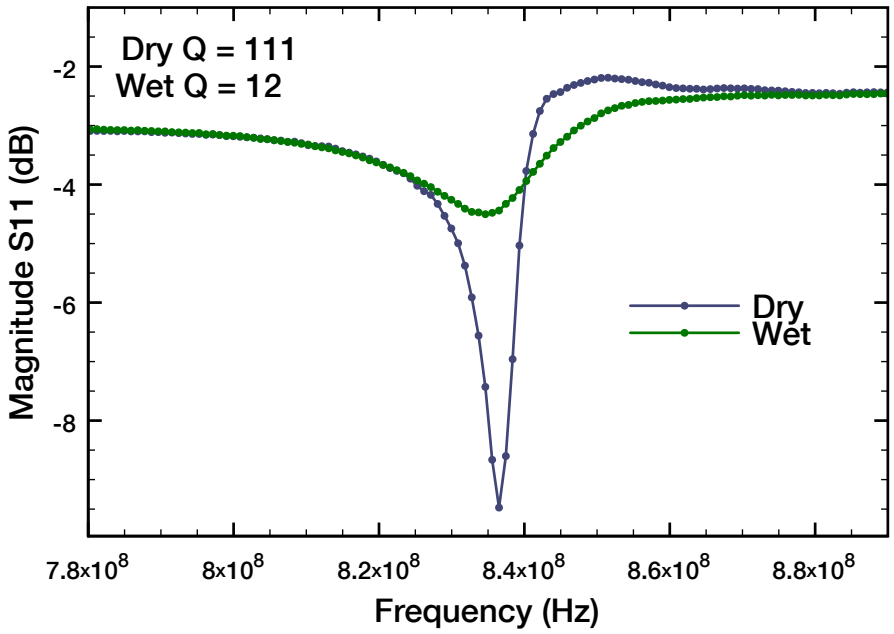

Figure 3.25: A thickness longitudinal resonator is measured and with its top surface immersed in water. The damping of the fluid degrades the measured quality factor.

be significantly reduced, where minimum detectable mass shift is inversely proportional to FBAR quality factor [122]. Fluid sensing applications are best addressed by shear mode resonators, while longitudinal mode FBAR devices are best applied to air and vacuum-based sensing environments.

3.8 Chapter Summary

This chapter provided the background necessary to understand the function of a BAW resonator, including both wave motion in bulk solids and the piezoelectric effect. A thin-film bulk acoustic resonator can be mechanically isolated from a substrate using a periodic acoustic reflector, which enables high Q devices to be built as solidly mounted structures. Several variations of FBAR devices were fabricated and characterized, and these demonstrated resonance between 800 MHz and 1.5 GHz with a typical quality factor Q of 200-300. These devices form the basis for the development of monolithic fabrication of FBAR devices on an integrated circuit substrate in the next chapter.

Chapter 4

Design of CMOS substrate and monolithic FBAR integration

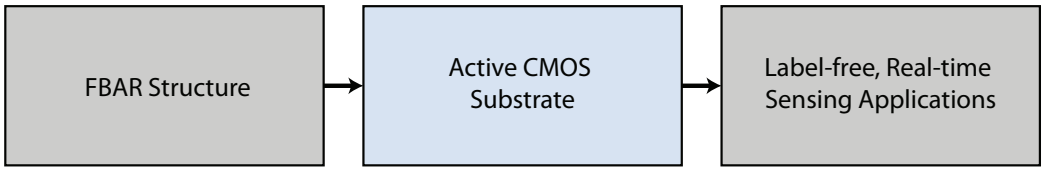

Figure 4.1: Chapter 4 describes the design, implementation, characterization, and post-fabrication of an active CMOS substrate for an FBAR-CMOS oscillator array.

4.1 Introduction

This chapter describes the design, development, and characterization of an active CMOS substrate for FBAR-based sensing applications. The substrate embeds all hardware required for oscillation, frequency counting, control, and digital data export directly beneath monolithically fabricated resonators, obviating the complex instrumentation typically employed for resonant sensing technologies.

This chapter begins with a discussion of the basic functional blocks required to support resonant sensing with CMOS circuits, followed by more detailed sections on CMOS oscillators and the Pierce oscillator topology, tradeoffs in digital frequency counting, and

global chip architecture and layout. The post-processing of fabricated dice is presented, followed by the electrical characterization of individual integrated FBAR-CMOS oscillators and experimental demonstration of a mass-based sensing application. The combined platform described here will be applied to a real-time, label-free gas sensing application in Chater 5.

4.2 Basic functions of a piezoelectric microbalance

4.2.1 Understanding the Sauerbrey equation

When a bulk wave acoustic resonator is employed as a sensor, material additions on the resonator top surface lower the resonant frequency in a manner approximated by the Sauerbrey equation

$$\Delta f = -\frac{f_\circ^2 \Delta m}{NA\rho} \tag{4.1}$$

where Δf is the measured frequency shift, $f_\circ$ is the resonant frequency, Δm is mass change caused by the added material, N is a materially-derived sensitivity constant and can be defined $N = V_{ph}/2$ within the piezoelectric layer, A is the surface area of the active resonator, and ρ is the density of the piezoelectric layer [9, 13]. This relation also applies to surface acoustic wave devices [123]. It is clear that the change in mass is proportional to the change in frequency, and for this reason acoustic wave sensors are frequently referred to as "mass-based" or "gravimetric" sensors. This nomenclature is misleading, and with a closer look both the sensing mechanism and an intuition for the limitations of the Sauerbrey equation can be uncovered.

Consider the thin-film layer illustrated in Figure 4.2. In Chapter 3, it was established that the resonant frequency of a BAW device is determined by the thickness of its active piezoelectric area, where bounding surfaces confine and enable standing acoustic waves in the elastic bulk. As a thin film of material is added to the resonator top surface, it becomes part of the acoustic path length, and the top surface reflection boundary moves slightly out. The thickness of the resonant cavity is increased, increasing the path length of a

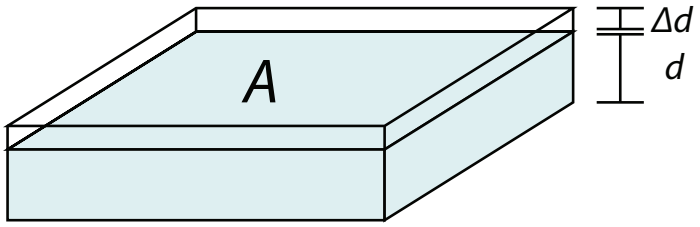

Figure 4.2: Thickness change induced by material accretion on an FBAR surface.

confined standing wave, and the resonant frequency decreases proportionally. Consider the Sauerbrey equation written in the form

$$\Delta f = -\frac{f_\circ^2 \Delta m}{(V_{ph}/2)A\rho} \tag{4.2}$$

and recall from (3.20) that the thickness of a half-wavelength acoustic resonator is given as

$$d = \frac{V_{ph}}{2f_\circ} \tag{4.3}$$

with the two equations (4.2) and (4.3) combined to yield the relation

$$\Delta f = \frac{-2f_\circ \cdot f_\circ \Delta m}{V_{ph} \cdot A\rho} = \frac{-f_\circ \Delta m}{d \cdot A\rho}. \tag{4.4}$$

For a thin-film material addition to the resonator top surface, let the thickness of this addition be described by Δd and the added material volume defined as $\Delta V = A\Delta d$. The density of the added material ρ can be related to this volume through the mass of the added material as $\Delta V = \Delta m/\rho$, which together define the relation

$$\Delta d = \frac{\Delta m}{A \cdot \rho} \tag{4.5}$$

which allows (4.4) and (4.5) to be combined to the more intuitive form

$$\Delta f = -f_\circ \left(\frac{\Delta d}{d}\right) \tag{4.6}$$

where the frequency shift of a BAW sensor is directly related to the change in thickness of the resonant layer. This relation is more closely aligned with the resonant sensing mechanism, where the thickness, and not the mass loading, determines the resonant frequency. The bulk acoustic wave device is modeled as a *distributed* mass-spring system in Chapter 3,

and the attached mass an extension of this distributed system. While this is, at some level, mass-based sensing, a microbalance is very much a distributed, ensemble metrology platform should not be envisioned as a micron-scale laboratory mass balance.

The form of (4.6) also enables an understanding of the limitations of the model. The Sauerbrey equation holds for very stringent assumptions: the added layer is thin relative to the thickness of the resonator; the added material comprises a stiff, elastic medium; the added layer is applied uniformly and homogeneously across the resonator surface [16]. The reasons for these assumptions are now implicit; it is assumed by the Sauerbrey equation that the accreted material to be sensed is simply an extension of the primary piezoelectric material. If this added layer is thick, then the acoustic velocity, density, and stiffness of the added material must be taken into consideration. If the added layer is heterogenous, materially lossy, or applied non-uniformly, then it cannot be treated as an extension of the piezoelectric layer, and the Sauerbrey equation does not apply.

For most sensing applications, the Sauerbrey equation is at best an approximation of the expected frequency behavior, and empirical sensitivity and concentration curves are critical to a quantifiable use of a resonant sensor. Modified empirical forms of the Sauerbrey equation have also been developed for application in liquid environments [12] and for decoupled mass attachments [14].

4.2.2 System-level implementation of a resonant sensor

A resonant sensor shifts in frequency in response to material aggregation on its surface. The primary function of an associated measurement system is to continuously monitor the resonant frequency for this shift and to quantify it. This is directly accomplished with the basic topology illustrated in Figure 4.3, which is functionally identical to a traditional quartz crystal microbalance (QCM). The BAW device is used as the resonant tank of a free-running high-Q oscillator, and the oscillator output is fed into a digital frequency counter for continuous, real-time quantification.

For a commercial QCM system, each of these functional blocks exist as a physical

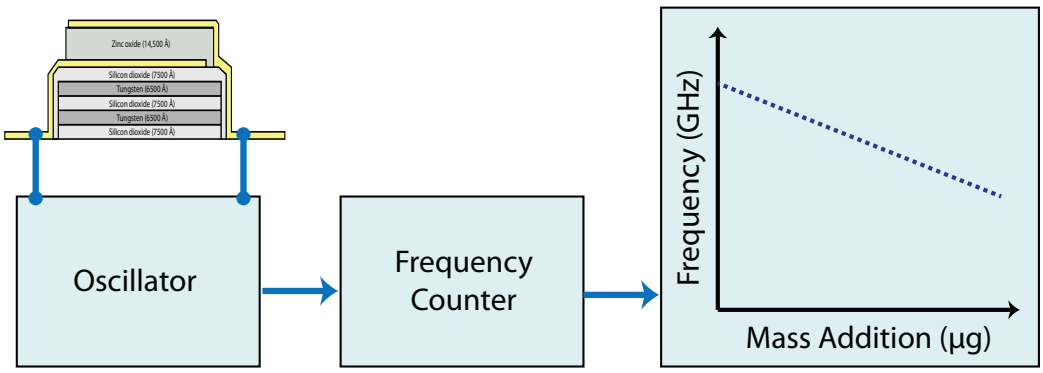

Figure 4.3: A basic microbalance topology wraps a free-running oscillator circuit around the crystal resonator, and the oscillator output is measured with a digital frequency counter.

box; the quartz crystal is held by a fixture, which connects to a discrete oscillator circuit and finally to a discrete frequency counter. This implementation is flexible and robust, but it is limited. With an oscillator and frequency counter box dedicated to a single sensor, multiplex interrogation of dozens or hundreds of sensors is infeasible. Just as critically for FBAR applications, this topology works with a quartz crystal in the standard 1 MHz to 20 MHz range, but it is significantly more difficult to implement in the gigahertz regime. Direct CMOS integration overcomes these primary limitations. The small size of the oscillator and counting circuit blocks enable dedicated circuitry for each of many FBAR structures, and the colocation of the FBAR and its support circuitry limits parasitics and allows direct frequency counting of high-frequency oscillators.

For the architecture illustrated in Figure 4.3, each of the circuit blocks will be described in detail. The resonator was discussed in Chapter 3, and in this chapter the oscillator and frequency counter are described.

4.3 Requirements for the FBAR-CMOS architecture

For a proof of principle, the minimal system requirements of an FBAR-CMOS sensor array comprise sufficient chip area for FBAR device fabrication, dedicated oscillator and frequency count blocks for each resonator, and global digital support for measurement control and data export. This functional combination allows for the operation of the sensor

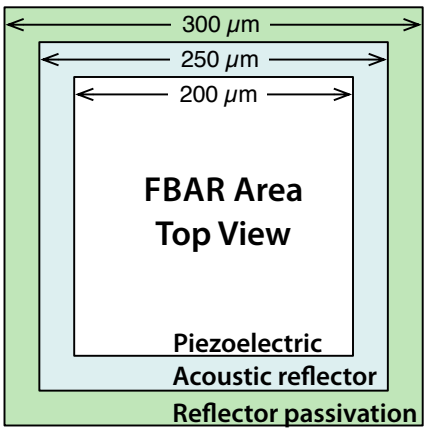

Figure 4.4: Illustration of the area requirements for an integrated FBAR structure on chip. The device forms a tiered structure with the acoustic reflector at bottom, reflector passivation at middle, and piezoelectric layer on top.

array without external support hardware, excepting a standard printed circuit board; the network analyzer and oscilloscope are eliminated from the measurement system. The design constraints of each block are driven by the overarching goal of parallel, high-resolution frequency measurement of on-chip FBAR sensors.

Area of individual FBAR device

FBAR devices built and characterized in Chapter 3 ranged from $80\times80\ \mu m^2$ to $200\times200\ \mu m^2$ for the active electrode overlap area, and a similar range of device sizes is supported by the active CMOS substrate. In addition to the electrode overlap area, the isolated acoustic reflector topology illustrated in Figure 3.15(b) requires additional area for the acoustic reflector, silicon dioxide reflector passivation layer, and some amount of buffer to allow for optical misalignment during manual photolithography. These dimensions for the largest ($200\ \mu m$) device are depicted in Figure 4.4.

The designated sensor array must also allow for access to top-level metal in the CMOS stack, as this is where electrical contact between the FBAR device and the underlying circuitry is made. Openings in the top passivation layer (i.e. 'glass cuts') are designed at a minimum width of 25 μm, which adds a total of 50 μm to the integrated sensor width and

another 50 μm for spacing between neighboring glass cuts.

Sensor array size

For a designated chip area of 3 mm $\times$ 5 mm, approximately 500 μm of the perimeter border is reserved for the pads and pad ring, allowing a maximum array size of 4 mm $\times$ 2 mm. This area is used to support a 6 $\times$ 4 array of 500 μm sensor sites, with additional area reserved for test sensor sites.

Frequency counting resolution and prescaling

Measurement resolution of an FBAR sensor will be limited by the quality factor of the resonator and oscillator or by the frequency counting resolution, whichever is worse. Frequency counting resolution is discussed in detail in Section 4.6. Digital counters scale in area with bit-width, and a compromise between desired resolution and feasible device area is required. For this design, 32-bit counters are implemented for both the reference and local counter blocks, and global counters are shared across multiple devices to address both area and power constraints.

Voltage and current requirements

An overall system power draw of less than 250 mW is targeted to allow bus-powering from a standard USB port. Approximately 100 mW is allocated to the CMOS chip, and the remaining is allocated to the FPGA and external support circuitry on the printed circuit board.

4.4 Global system architecture

The basic functional layout of the active CMOS substrate design in shown in Figure 4.5. Each sensor site comprises an oscillator circuit, prescaler, and a 32-bit digital counter. Each array column has a dedicated 32-bit reference counter, all of which share a common reference frequency input f_{ref}. This setup allows for simultaneous frequency counting across the array

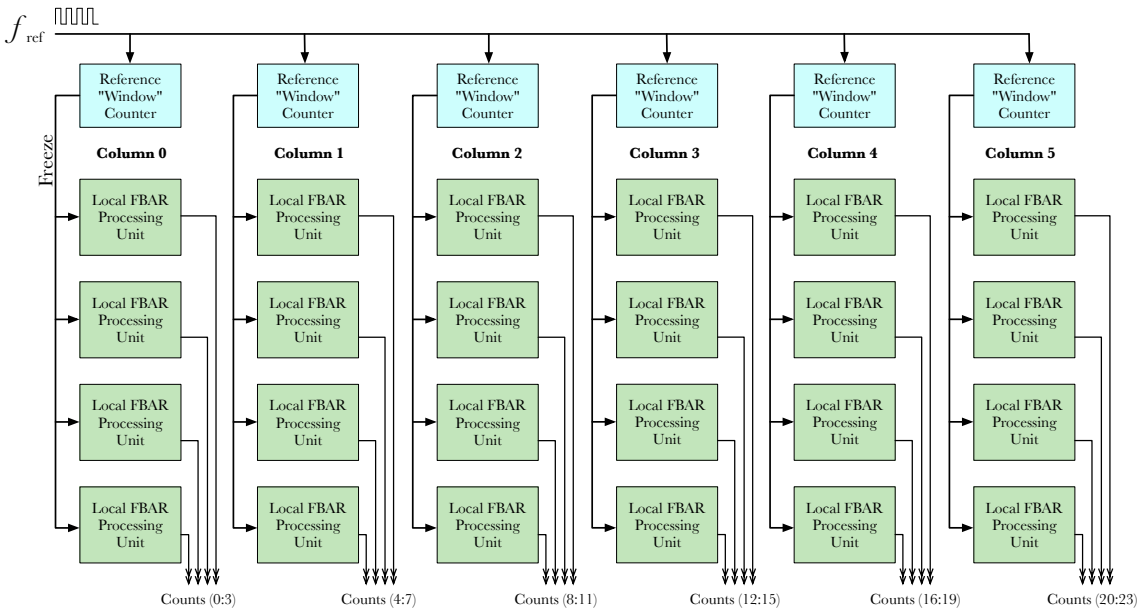

Figure 4.5: Global architecture of the FBAR-CMOS chip. A 6×4 array of sensors is supported, each with a dedicated prescaler and frequency counter. Each column has a reference counter, all of which share the same reference frequency f_{ref}.

and control of the integration window at the level of each column. Data output is routed to four two-wire serial output ports, and configuration and control signals are managed by a global decoder block. The design and implementation of each of these blocks is detailed in the following sections.

4.5 Design of oscillator circuits

An oscillator is built around an FBAR device in the same manner as building a quartz crystal oscillator. In this section, an electrical model of an FBAR device is described for use in design and simulation. The Pierce oscillator topology, commonly employed for crystal oscillators, is designed in concert with the FBAR electrical model and is implemented in a CMOS technology.

4.5.1 Electrical model of a bulk acoustic wave device

For design purposes, the electrical behavior of an FBAR device can be described by the Butterworth-Van Dyke (BVD) model [124]. This model comprises two branches, as depicted in Figure 4.6. The capacitor $C_\circ$ models the large static capacitor formed by the basic FBAR structure, in which a bulk non-metallic layer is sandwiched between two electrodes. This capacitance is materially based, and it is simply described as a parallel plate capacitor with

$$C_\circ = \frac{\varepsilon \cdot A}{d} \tag{4.7}$$

where A is the area formed by electrode overlap, ε is the permittivity in the piezoelectric layer, and d is the thickness of the piezoelectric later [125]. The other branch of the BVD model is the motional arm, whose components model the electrical resonance of the piezoelectric device but have no direct physical meaning [126].

Together, the two branches form both a series and parallel resonance, as anticipated by the measured devices in Chapter 3. The motional arm has an impedance described by

$$Z_m(\omega) = R_m + j\omega L_m + \frac{1}{j\omega C_m} \tag{4.8}$$

and a corresponding series resonance of the standard RLC form

$$\omega_s = \frac{1}{\sqrt{L_m C_m}} \tag{4.9}$$

where the impedance is at a minimum [127]. This models the series resonance of the FBAR structure, occurring at the frequency for which L_m and C_m have equivalent impedance but opposite phase. The static capacitance arm has an impedance of the standard capacitive form

$$Z_{C_\circ}(\omega) = \frac{1}{j\omega C_\circ} \tag{4.10}$$

and a parallel antiresonance is formed between L_m and the combined series capacitance of $C_\circ$ and C_m. The occurs at a frequency given by

$$\omega_p = \frac{1}{\sqrt{L_m \cdot \left(\frac{C_m C_\circ}{C_m + C_\circ}\right)}} \tag{4.11}$$

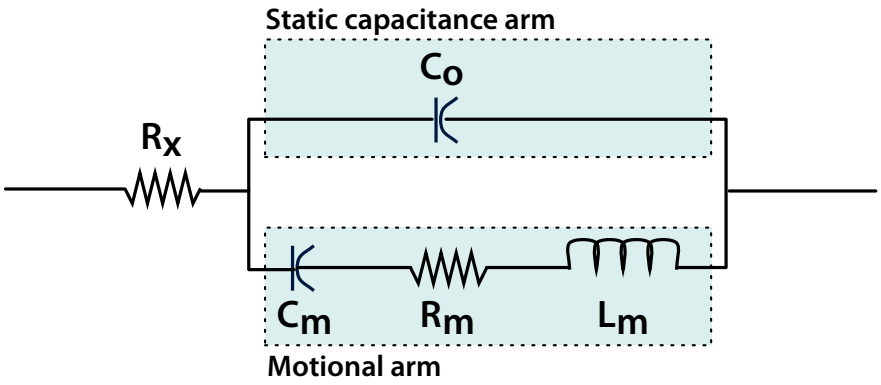

Figure 4.6: Butterworth-Van Dyke model of a piezoelectric resonator. The static capacitance arm models the parallel plate capacitor formed by the FBAR structure. The motional arm models the electrical series resonance induced by the piezoelectric resonator.

and corresponds to an impedance maximum when looking into the BVD circuit. For simplicity, we can relate series and parallel resonances directly by combining (4.9) and (4.11) as

$$\omega_p^2 = \omega_s^2 \left(1 + \frac{C_m}{C_\circ}\right). \tag{4.12}$$

This begins to explain how electromechanical coupling factors k_t^2 and k_{eff}^2 and quality factor Q can be related to the frequency spacing between ω_s and ω_p, as defined in Chapter 3.

The BVD model is attractive for its simplicity and ease of simulation; the model has a DC solution, unlike direct simulation from s-parameters in which a DC solution must be explicitly added. However, the BVD and related lumped-element forms fail to account for additional and sometimes significant complexities of a real FBAR device in a circuit environment. Resonant overtones, electrode and acoustic reflector loading, and environmental loading of the ambient environment (air or water) are all ignored in the BVD model. For optimization of FBAR structures and the development of overtone resonant circuits, more complex FBAR models developed by Mason and Ballato may be used [115, 128]. These models both employ network and transmission line approaches to couple effects of acoustic loading and overtone and parasitic resonances. A detailed review of these techniques is left to [90], as only the BVD model was employed in this chip design.

For the design described in this chapter, FBAR devices had not been successfully fab-

Table 4.1: Subset of BVD parameters used for design to model electrical behavior of an FBAR device.

Parameter	**Value (1 GHz)**	**Value (2 GHz)**
$C_\circ$	125 fF	250 fF
C_m	32 fF	40.5 fF
L_m	770 nH	146 nH
R_m	4.4 Ω	4.4 Ω
R_x	0.25 Ω	0.25Ω

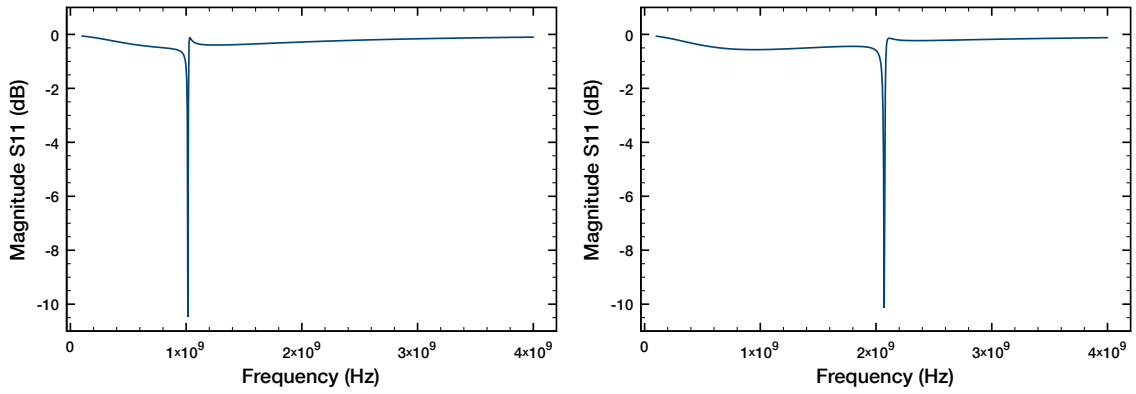

(a) (b)

Figure 4.7: The Butterworth-Van Dyke model of a crystal resonator has been simulated using the parameters listed in Table 4.1. The resonator in (a) has a series resonance at 1.01 GHz, and the resonator in (b) has a series resonance at 2.06 GHz.

ricated and characterized at the time of circuit implementation. An amalgam of published BVD parameters was used to approximate the expected device characteristics, and a range of parameters was tested. These described oscillators from 500 MHz to nearly 3 GHz. An example of such parameters is listed in Table 4.1, and the BVD model has been simulated in Figure 4.7 using SpectreS (Cadence Design Systems) for s-parameter characterization.

4.5.2 Oscillator fundamentals

As a spring oscillates, energy is transferred alternately between mechanical potential energy and kinetic energy, and in a real spring some energy is lost during each compression and extension. This lost energy is quantified by the quality factor Q as described in Chapter

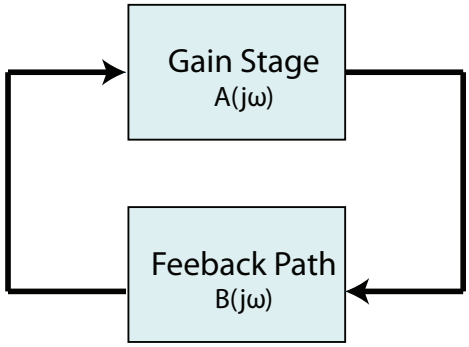

Figure 4.8: Basic feedback model used to define the Berkhausen criterion for steady-state oscillation. Loop gain must be unity, and total phase shift must be a multiple of 2π.

3, and this loss is compensated by the periodic injection of energy into the system. If the energy is greater than the energy lost each cycle, the amplitude of oscillation will grow until the system is limited or destroyed. If the injected energy is less than the energy lost each cycle or injected at the wrong part of the cycle, the amplitude of oscillation will slowly decrease, until the system is at rest. If the injected energy is *identical* to the amount of energy lost each cycle and injected at the correct phase each cycle, the oscillation will continue at its current amplitude indefinitely. This last case is a stable oscillation.

For a piezoelectric resonator in oscillation, energy is injected into the system through the electrical domain. It is critical that this be of the correct magnitude and phase to enable a steady-state oscillation. These intuitive requirements are mathematically described by the Barkhausen criterion, which describes a simple amplifier and feedback block as depicted in Figure 4.8 [129].

For a gain stage with gain $A(j\omega)$ and a frequency-dependent feedback path $B(j\omega)$, the loop transfer function is given as

$$T(j\omega) = A(j\omega) \cdot B(j\omega) \tag{4.13}$$

which can only describe steady-state oscillation if the Barkhausen criterion is met; the loop gain must have unity magnitude, and the total phase shift for the loop must be a multiple

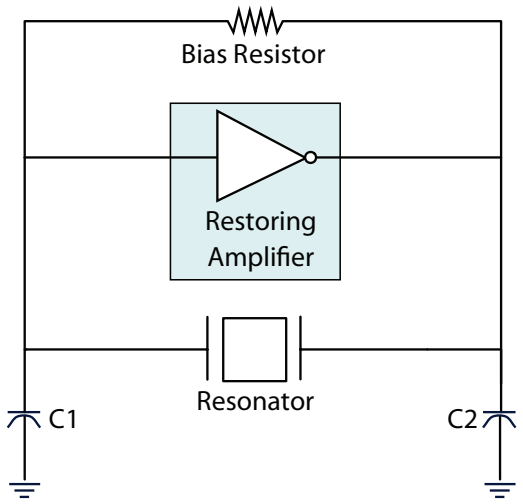

Figure 4.9: A Pierce oscillator is commonly employed for the construction of a crystal oscillator. An inverting amplifier serves as the restoring element, and a crystal resonator and two capacitors for the feedback network. A large resistor is included for biasing.

of 2π. This is summarized as

$$|T(j\omega)| = 1 \tag{4.14}$$

$$\angle T(j\omega) = 2\pi n, n \in 0, 1, 2, 3... \tag{4.15}$$

and importantly describes only a *requirement* of stead-state oscillation; systems meeting this criterion can be constructed that will not oscillate [130, 131].

For a circuit implementation, the gain element will be provided by an amplifier, and the feedback path will be constructed around an acoustic resonator. The amplifier gain must be sufficiently large to compensate for loses both in the resonator and in parasitic elements, and the feedback path must yield the correct total phase shift at the target oscillation frequency. This is implemented for the FBAR oscillator array using a Pierce topology.

4.5.3 Pierce oscillator topology

The basic Pierce oscillator is shown in Figure 4.9. It requires an inverting amplifier for the gain stage, and a resonant crystal and two capacitors form the feedback network. This circuit is closely related to a Colpitt's oscillator, in which two capacitors and an inductor form

the resonant tank of a feedback oscillator [132]. The Pierce oscillator was first developed by G.W. Pierce in 1923 [133]. In the Pierce circuit, the inverting amplifier provides the gain needed to overcome electrical losses in the crystal, and it provides 180° phase shift. The crystal and discrete capacitors form a pi-network filter, which passes only frequencies near the crystal resonance and provides an additional 180° phase shift. With only a few elements, this circuit can meet the Barkhausen criterion and build a sustainable stead-state oscillation. The lack of a discrete inductor is attractive for CMOS implementations.

The resistor shown in Figure 4.9 is not strictly necessary to the function of the basic oscillator, but in most cases it is included to bias the inverting amplifier element [134]. The amplifier is commonly implemented in CMOS circuits with a digital inverter, in which case the resistor biases this element in its high-gain region. The capacitors may be added explicitly or formed by parasitic capacitance at the nodes.

4.5.4 CMOS implementation

The Pierce oscillator was implemented in this CMOS design using three different inverting amplifiers, which are illustrated in Figure 4.10. Each of these designs was replicated at eight locations within the 6×4 FBAR array, with designs tiled to spread each variant across the array. The design goal was both to explore the phase noise and frequency shift resolution of each architecture, and to increase the likelihood of producing a successful, self-starting oscillator design.

The first Pierce oscillator, shown in Figure 4.10(a), uses a single N-channel MOSFET device as an inverting amplifier, which was demonstrated by Otis *et al.* to produce a stable, low-noise oscillator when paired with an FBAR resonantor [134]. In this design, M1 forms the inverting amplifier, while M2 is used as an adjustable, high-value feedback resistor set by voltage V_{FB}. The amplifier is biased with M3, using an off-chip reference to set the current in the current mirror formed by M4 and M3. The output of the oscillator is buffered before driving a local prescaler. The capacitors C1 and C2 are designed with metal-insulator-metal (MIM) stack structure as enabled by the 0.18 μm RF CMOS technology, which allow

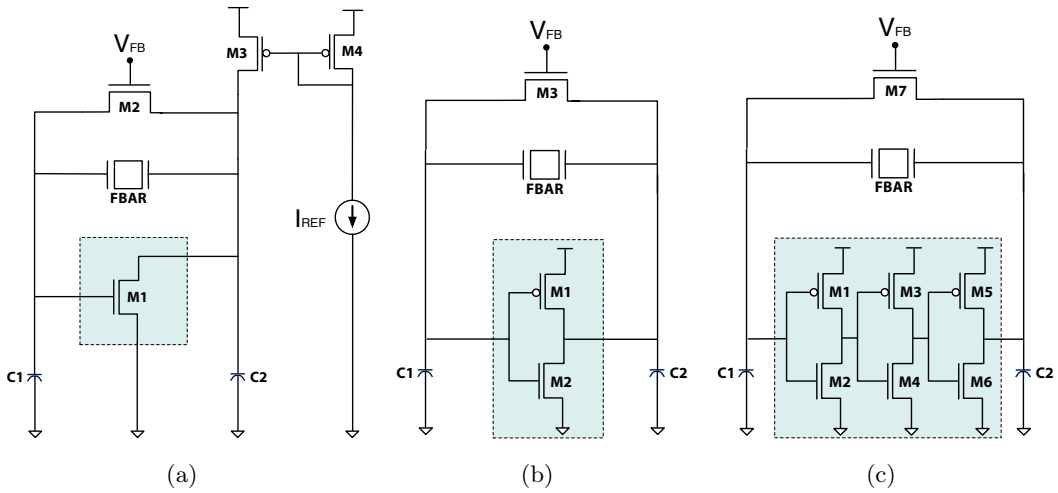

Figure 4.10: Three variations of the Pierce oscillator were implemented in the CMOS design. The inverting amplifier is implement with a single N-channel MOSFET device (a), and basic inverter (b), and cascaded inverters (c). All outputs are buffered (not shown).

a capacitor density of 4 fF/μm^2. The design supports a bias current of 1-2 mA through M3.

For the design in Figure 4.10(b), the inverting amplifier is implemented with a standard CMOS inverter; this is a very common architecture for a quartz crystal oscillator. The inverter formed by M1 and M2 is again biased by the adjustable feedback resistor M3, and the discrete capacitors are implemented with a MIM stack as before. This oscillator derives high gain from the biased inverter, and it is wired to a separate voltage rail to allow some amount of voltage-based gain scaling of the inverter. The oscillator in Figure 4.10(c) is largely identical, with the single CMOS inverter replaced by a three-inverter cascade for additional gain.

The layout of each oscillator is dominated by the MIM capacitors, as shown in Figure 4.11, with the layout mirroring the simple schematic representation of Figure 4.9. Simulated oscillators have a peak to peak voltage swing of 700-800 mV before entering the output buffers.

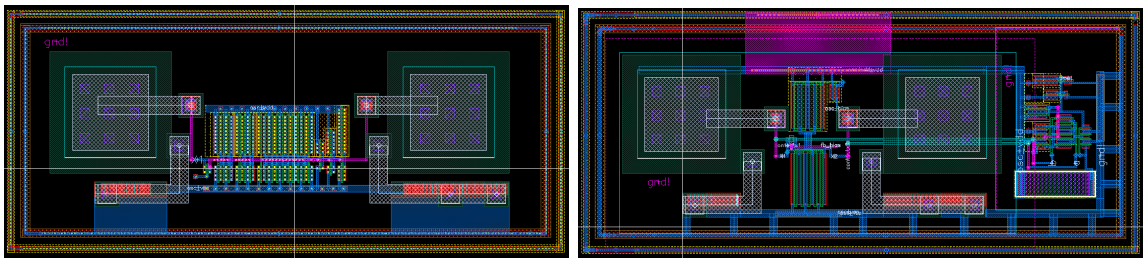

(a) (b)

Figure 4.11: Layout of two Pierce oscillator topologies used in this design. Metal-insulator-metal capacitors flank the restoring element, and the circuits are surround by a guard ring. The three inverter cascade is shown in (a), and the single N-channel design is shown in (b).

4.6 Frequency counting

The primary purpose of the digital CMOS circuitry is to perform a frequency counting function on the output of the FBAR-based oscillator. The goal is to achieve a counting resolution that does not limit frequency resolution of the final system. The most basic method of implementing a frequency counter relies on comparing a target frequency to a known reference frequency through independent counters, as depicted in Figure 4.12.

The first counter, used as a reference, is incremented on each rising edge of a known stable frequency f_{ref} for a determined period of time T_{window}. This T_{window} forms a measurement window of a known duration to act as an absolute time reference. The second counter is incremented on each rising edge of the target frequency f_{measure}, starting from

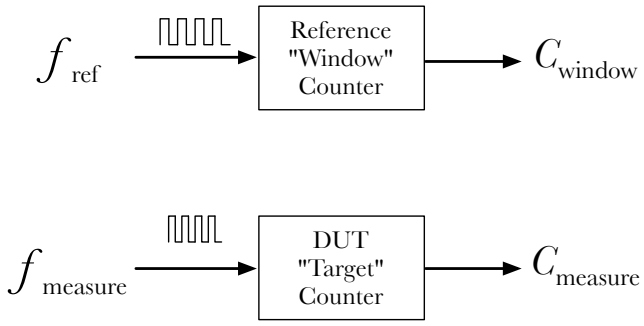

Figure 4.12: Frequency measurement using two independent counters.

zero and incrementing for a duration of T_{window}. At the end of the measurement window, the target counter value is frozen. The counting window is calculated as

$$T_{\text{window}} = \frac{C_{\text{window}}}{f_{\text{ref}}} \tag{4.16}$$

which allows for the direct calculation of the target frequency from the value of its counter

$$f_{\text{measure}} = \frac{C_{\text{measure}}}{T_{\text{window}}} = f_{\text{ref}} \cdot \left(\frac{C_{\text{measure}}}{C_{\text{window}}} \right). \tag{4.17}$$

Ideally, T_{window} and C_{measure} are exact, but in a real system both suffer uncertainty due to their quantized natures. Each of these uncertainties limits the precision of the frequency counting architecture.

Uncertainty of frequency count

For a digital frequency counter, theoretical resolution is primarily a function of the number of counts per measurement. As an illustrative example, consider a known ideal test frequency of 100 MHz driving an 8-bit counter with a period of 10 ns. Assume also an integration window of 2 μs, such that the counter logs 2 $\mu s/10\ ns = 200$ counts. From the output perspective, the signal was fast enough to trigger 200 counts instead of 199, and slow enough to fail to reach 201 counts. Even for an exact 100 MHz input signal, a 2 μs window can only measure the frequency to within 99.5 MHz $< f_{\text{measure}} <$ 100.5 MHz, or $\pm 500kHz$.

More generally, this is described by the relation

$$\left(f_{\text{osc}} - \frac{1}{T_{\text{window}}} \right) < f_{\text{meas}} < \left(f_{\text{osc}} + \frac{1}{T_{\text{window}}} \right) \tag{4.18}$$

where f_{osc} is the unknown frequency. The measurement uncertainty $\Delta f_{\text{measure}}$ can be bounded as

$$|\Delta f_{\text{meas}}| < \frac{1}{T_{\text{window}}} \tag{4.19}$$

where the final measured frequency is known with an accuracy of

$$f_{\text{measure}} = f_{\text{osc}} \pm \Delta f_{\text{measure}}. \tag{4.20}$$

Table 4.2: Uncertainty in f_{meas} due to target frequency counter quantization is calculated for various counter bit-widths. ($f_{\text{osc}} = 100$ MHz)

Target Counter Size (Bits)	**Counts**	T_{window}	Δf_{meas}
4	15	150 ns	± 6.67 MHz
8	255	2.55 μs	± 392 kHz
16	65536	655 μs	± 1.53 kHz
24	16777215	167.8 ms	± 5.96 Hz
32	4294967295	42.9 s	± 0.023 Hz

As is clear from (4.19), a longer integration period yields greater precision. For an ideal input signal of 100 MHz, uncertainty caused by the quantized target counter can be seen in Table 4.2 for different counter bit-widths.

Uncertainty of integration window

The measurement integration window is also set by an on-chip counter, which suffers the same fundamental quantization-related uncertainty as the target counter. This source of error is avoided by using the reference signal f_{ref} as the main clock driving the digital timing logic. In this manner, the signal used to freeze the local counter always arrives at a fixed delay from the edge of f_{ref}, and every frequency count operation is referenced identically to the reference counter. Any variation in f_{ref}, however, will still directly limit the accuracy and resolution of the frequency counting circuits. A temperature compensated quartz crystal oscillator is used as the external reference to minimize this source of measurement variation.

4.7 Oscillator Pre-scaling

Sub-micron CMOS technologies can be used to implement high speed counters for frequency measurement on multi-gigahertz signals, but this comes at a cost of significant design complexity and power dissipation. Lower frequency signals are more easily managed. Additionally, it is desirable to have $f_{\text{ref}} > f_{\text{measure}}$, and importing a stable, on-chip reference in the gigahertz range is nontrivial. It is preferable for a low power and low complexity design to

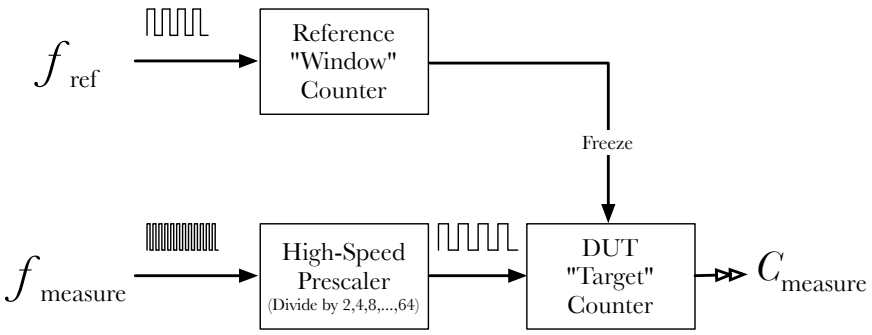

Figure 4.13: Frequency measurement using prescaler and two independent counters.

divide the target frequency down to a more manageable range. This functional topology can be seen in figure 4.13. This decreases total counts in a given integration period, which must be balanced by lengthening T_{window} proportionally to maintain counting resolution.

In this design, a counter-divider prescaler is implemented that allows the oscillator frequency to be divided in programmable octaves from 2 to 64. This circuit block was simulated to operate up to 3 GHz in typical processing corners and 2 GHz in worst-case processing corners. A dedicated prescaler is located adjacent to each buffered oscillator output in the integrated array.

4.7.1 Functional design of an individual oscillator site

The main sensor array consists of a grid of FBAR structures built directly on top of the CMOS substrate. Underneath each of these sensors resides the supporting CMOS circuitry required for each resonant sensor. Each site contains an oscillator, prescaler, 32-bit counter, and parallel-load shift register. The shift register stores the local count value at the end of an integration window and is used for data export. The functional topology of each FBAR site is shown in figure 4.14.

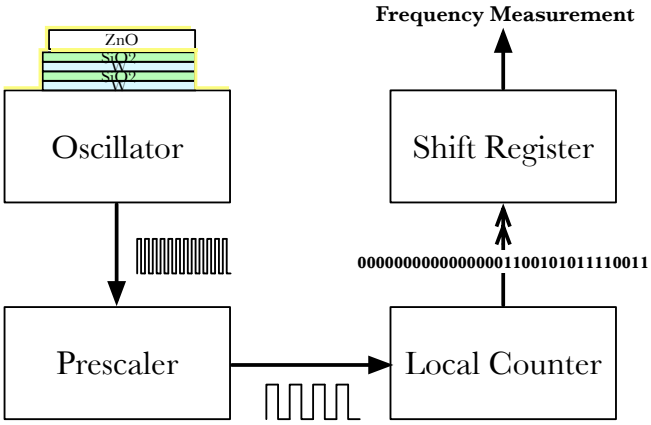

Figure 4.14: Each site in the array includes an oscillator, programmable prescaler, 32-bit counter, and 32-bit shift register. The final count value is stored in the shift register until data export.

4.8 CMOS design and fabrication

The design of the active substrate for the FBAR-CMOS oscillator array was completed in a 0.18 μm CMOS RF process from IBM. This technology supports 6 metal routing layers, including top metal, and it supports dual metal-insulator-metal (MIM) capacitors. The lowest metal layer is copper, and all other metal layers are aluminum. The technology uses a 1.8 V core voltage rail and supports 3.3 V I/O circuits. The total fabricated chip area is 3 mm $\times$ 5 mm and includes 158 pads. The fabricated die photo is shown in Figure 4.15.

The bulk of the chip area is dedicated to the oscillator array, which supports 24 sensor sites in a 4 $\times$ 6 grid. Each of the three oscillator topologies described in Section 4.5.4 are tiled at eight locations. To the left of the array in Figure 4.15 are two oscillator test sites, which are powered independently of the main pad ring and include dedicated local prescaling circuits. To the right of the oscillator area is a large, open area for the fabrication of one or more standalone FBAR structures, as discussed in Chapter 3. The active and passive test sites serve two purposes; first, these allow characterization of the the FBAR structure and the integrated oscillator independent of the full chip and frequency counters; second, these allow a fabricated FBAR batch to be tested prior to chip packaging.

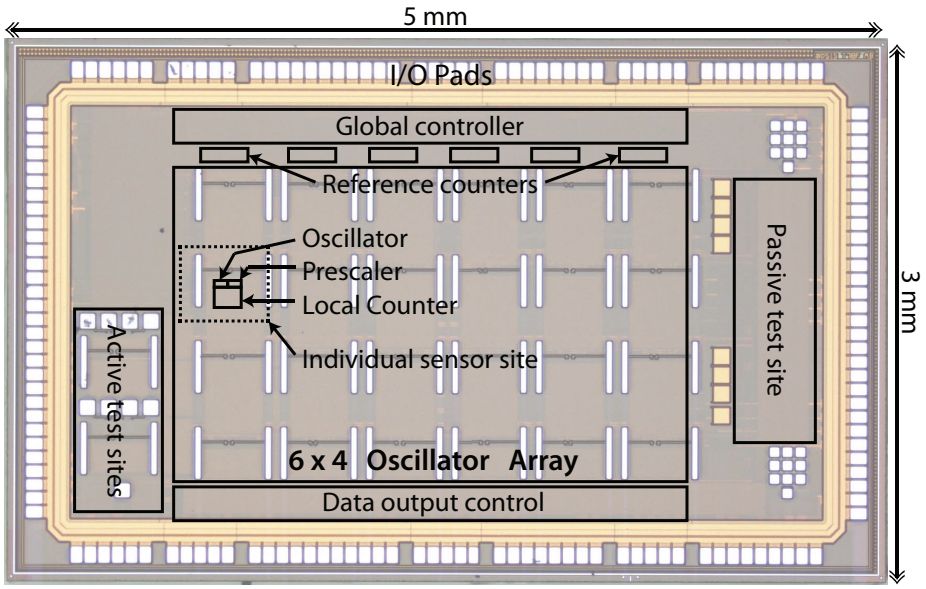

Figure 4.15: Annotated die photo of the fabricated CMOS chip. The 6×4 array sites are flanked by FBAR test sites, and column reference counters and global controller are along the top edge. Final chip layout size is 3 mm×5 mm.

The oscillator and prescaler units were designed at the transistor level, as these are the most critical, high-frequency, and layout-dependent circuit blocks. Digital counters, serializers, and control decoder circuit blocks were synthesized from VHDL and placed and routed using standard cells.

The completed chips were diced commercially, and post-fabrication of FBAR structures was performed on individual chips.

4.9 Post-processing of CMOS dice for monolithic FBAR integration

The process flow for fabrication of standalone FBAR devices was described in Chapter 3, and it requires only slight modification for the fabrication of FBAR devices directly on a CMOS substrate. This section will describe the adapted process flow for monolithic integration. Chip surface roughness and top-metal step profiles are also measured, and completed on-chip devices are presented.

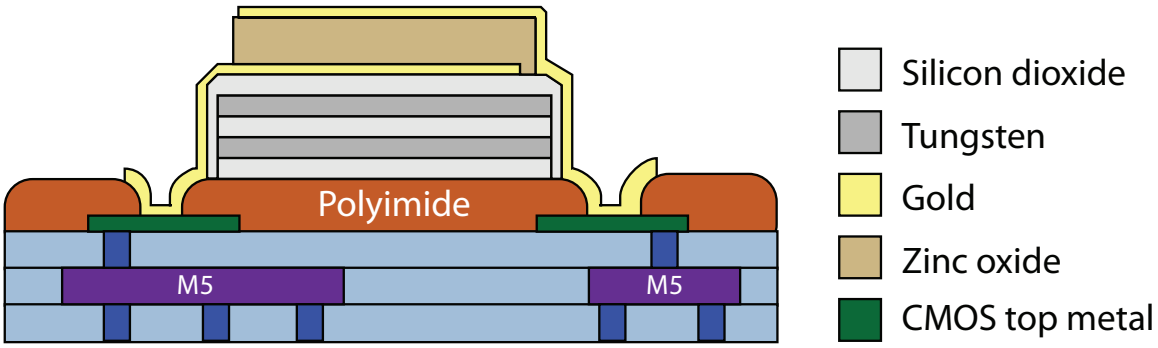

Figure 4.16: Cross-section illustration of a monolithically fabricated FBAR structure on a CMOS substrate. The top and bottom contacts of the resonator connect to the underlying integrated circuits through openings in the chip passivation layers, where a direct metallic contact is made to the top metal layer in the CMOS stack.

4.9.1 Monolithic fabrication process flow

A cross-section of an integrated FBAR device is shown in Figure 4.16. This structure is identical to the isolated-mirror FBAR devices characterized in Section 3.7, and the top and bottom electrodes now connect directly to the CMOS top-level metal layer. The ground lines from the ground-signal-ground layout are also removed, leaving only the signal pathway through the FBAR device.

While structurally similar to standalone FBAR devices, on-chip fabrication requires several additional steps in order to process individual CMOS dice. A single chip is mounted on a section of wafer or glass slide using a small drop of poly(methyl methacrylate) (PMMA), which is heated to 120°C to set. PMMA works well as a temporary mounting adhesive, as it is resistant to UV-photoresist developer but can be released in acetone or Remover PG. Some care must be taken to minimize the time a chip spends in developer or solvent, as these solutions have non-negligible etch rates for the aluminum bond pads [135].

A mounted chip is coated with the bilayer process developed in Chapter 3, and in some cases an additional layer of low-viscosity LOR is applied first to smooth out the abrupt steps around the chip edge and pad openings. Bubble formation is common in this process and is a primary source of low processing yields. The photoresist layers are patterned using a chrome-on-glass mask set. The masks were designed and fabricated in-house on a direct-

write laser system (Heidelberg μPG 101), and a total of five mask layers is required for fabrication of the FBAR topology of Figure 4.16.

4.9.2 Surface roughness of CMOS substrate

Above the top metal layer, the CMOS substrate is passivated with silicon dioxide, silicon nitride, and polyimide. This stack forms the build surface for monolithic FBAR structures, which is a much rougher surface than the silicon and glass substrates used for standalone FBAR fabrication. If this roughness propagates through the multilayer device structure, it can have deleterious effects on the resonant quality factor. Roughness at a reflection interface increases scattering and decreases the amount of energy confined in longitudinal standing waves [136].

Vorbiev *et al.* investigated the effect of electrode roughness on 5 GHz barium strontium titanium oxide (BSTO) resonators, and they demonstrated a measurable decrease in quality factor for increased surface roughness [136]. A Q-degradation from 350 down to 150 was reported for an average roughness increase from 3.2 nm to 6.9 nm. While it is difficult to isolate the cause of this degradation, with electrode roughness affecting both interface scattering and crystal orientation in the deposited films, it is clear that a smoother build surface will yield higher quality devices. This result is also intuitive.

The polyimide surface roughness of the fabricated CMOS substrate described in previous sections was measured with an atomic force microscope (AFM), and the surface profile for an untreated 5×5-μm^2 polyimide area is shown in Figure 4.17(a). This area is not directly over any top-metal routing. The average surface roughness R_a is 12.4 nm, with a maximum peak-to-trough height of 92 nm.

The polyimide layer can be removed with a solvent process. A bath of hydroxylamine-based ACT 935 UP photoresist stripper (ACT Electronic Materials) is heated to 90°C, and bare dice are submerged for 4-8 hours. No additional polyimide removal was observed with increased time, and aluminum bond pads and exposed top-metal electrodes appeared unaffected.

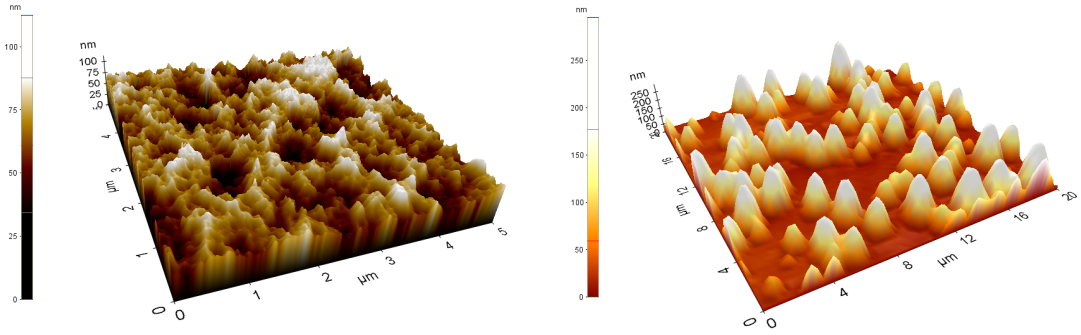

(a) (b)

Figure 4.17: Atomic force microscope scan of chip surface for characterization of surface roughness. The polyimide surface in (a) has a roughness of R_a=12.4 nm, and after polyimide removal the surface roughness in (b) is increased to R_a=54.2 nm.

The surface of a stripped CMOS die is shown in Figure 4.17(b), and the measured surface roughness R_a is 54.2 nm, with a maximum peak-to-trough height of 248 nm. It is clear that the polyimide removal has left behind a sparse assortment of mounded structures. The material makeup of these remnants is unknown. The high etch rate of most solvents for aluminum prevented further attempts to identify or remove these structures. Monolithic FBAR structures are instead built directly on the polyimide surface, which suffices for usable resonators but has an unquantified effect on quality factor. Future work might benefit from planarization of the CMOS die prior to post-fabrication, where chemical mechanical polishing (CMP) or other such planarization techniques could enable an increase in on-chip resonator quality factor.

4.9.3 Step profile of top-metal access

As illustrated in Figure 4.16, a monolithic FBAR structure makes electrical contact with underlying CMOS circuits through openings in the top passivation layers. These openings give direct access to the top metal layer in the BEOL stack. The passivation layers comprise several microns of oxide, nitride, and polyimide, creating large step feature that must be traveresed to electrically connect top metal to a device on the polyimide surface. It is critical that the electrical contact be continuous across this step.

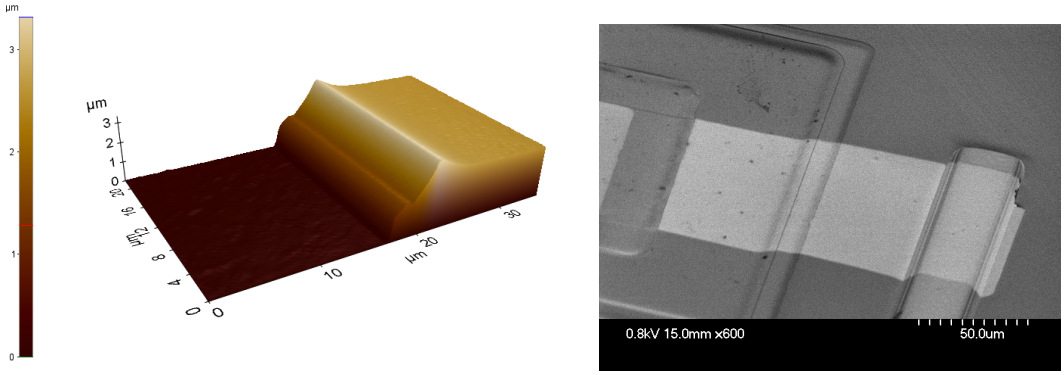

(a) (b)

Figure 4.18: An atomic force microscope scan of the CMOS passivation opening is shown in (a) with a step heigh of 3.3 μm and sloped sidewall. The tilted scanning electron micrograph in (b) shows step coverage achieved by electron-beam evaporation.

The step profile from polyimide chip surface to top-metal at a passivation opening was measured using an AFM, and the results are shown in Figure 4.18(a). The peak height from top-metal to polyimide is 3.3 μm, with an approximately linear transition over 5 μm for a sidewall angle of 33° with respect to the top-metal surface. This shallow angle is advantageous for fabrication, as conformal metal deposition is not required. Line of site methods like electron-beam evaporation produce sufficient sidewall coverage for low resistance metallic contacts. This can be seen in the scanning electron micrograph of Figure 4.18(b), where an evaporated gold contact is continuous across the step boundary. These contacts have also been tested electrically and demonstrate a resistance comparable to contacts made on the planar chip surface.

4.9.4 Monolithic FBAR structures on CMOS

The process flow described in Section 4.9.1 was used to fabricate many batches of on-chip FBAR structures. Optical and scanning electron micrographs of typical post-fabricated devices are shown in Figure 4.19.

Several fabrication batches produced an entire array of non-functional devices. The most common cause of a failed fabrication was a defect in the photolithography stack.

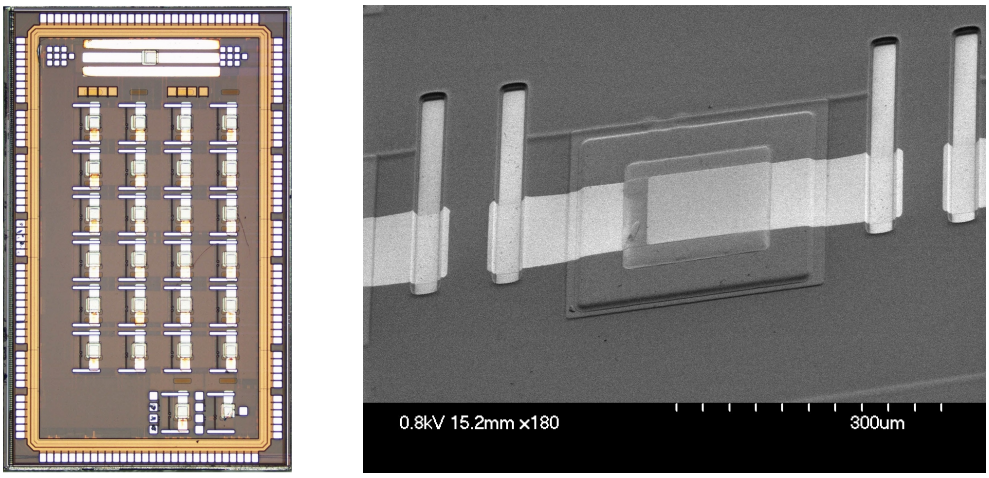

(a) (b)

Figure 4.19: A die photo of a post-fabricated chip is shown in (a), where they 6×4 array of FBAR devices is visible. A scanning electron micrograph of an on-chip FBAR is shown in (b).

Edge beads and photoresist build-up in chip corners led to undeveloped features, as seen in the corner test structure of Figure 4.19(a). Cracks and bubbles in the resist layers led to openings that allowed top aluminum surfaces to be attacked by developer. These openings also enabled metallic shorts during top and bottom contact deposition. Substrates with shorted or eroded bond pads did not move forward in the process flow. For a successfully post-fabricated substrate, it was typical that all measured FBAR devices in the array were functional, and process failures were typically chip-wide.

4.10 Packaging and platform development

A post-fabricated FBAR-COS chip is wire-bonded to a 144-pin ceramic pin grid array (PGA) package. The bonding was done both commercially, as seen in Figure 4.20(a), and onsite with a semi-automated wedge bonder. For testing a small number of dice, the latter was used, although the tight pad pitch and wedge bond setup only allow access to approximately 100 of the 158 pads, making sacrifices in both power delivery and chip functionality. However, all basic chip features can be powered, controlled, and accessed with this subset of pads.

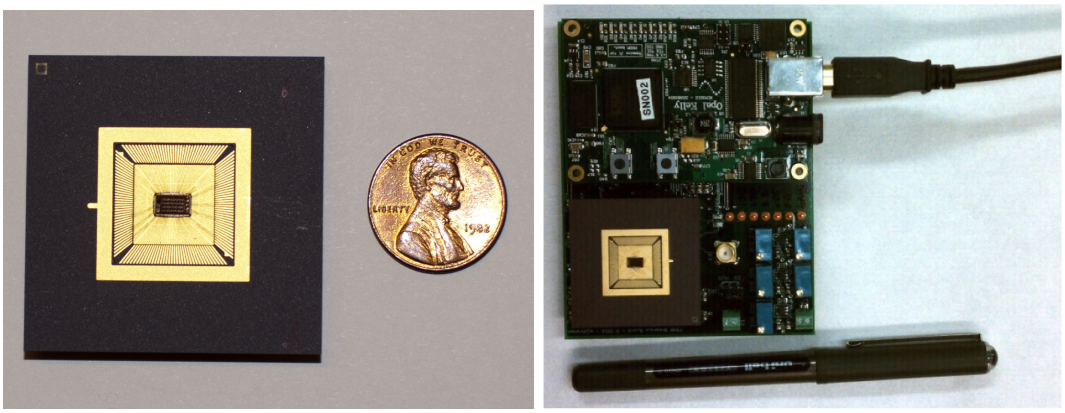

(a) (b)

Figure 4.20: Post-fabricated chip is wire bonded to a 144-pin ceramic pin grid array package, shown in (a). This is socketed to the custom printed circuit board pictured in (b) for electrical interface.

The packaged chip is socketed into a custom 4-layer printed circuit board (PCB), shown in Figure 4.20(b). The PCB includes on-board voltage regulators for core, I/O, and oscillator supply voltages, regulators for oscillator biasing, and a 10 MHz temperature compensated crystal oscillator for use as a frequency counting reference. A commercial FPGA daughter board (Opal Kelly) is also socketed to the PCB, and this is used for both control and data interface with the CMOS chip. The FPGA board includes a USB port, which is used for communication with an external MATLAB user interface and may also be used to power the complete test system.

4.11 Electrical characterization of FBAR-CMOS array

After device fabrication, both standalone on-chip FBAR devices and integrated FBAR-CMOS oscillators were characterized. A standalone device was analyzed with the techniques outlined in Chapter 3 for s-parameter measurement. Integrated oscillators were characterized through the use of a high-speed oscilloscope and a phase spectrum analyzer.

Electrical characterization of two device batches is reported in this section, representative of the quarter- and half-wavelength topologies illustrated in Figure 3.23. The

quarter-wavelength batch has a primary resonance near 900 MHz, and more recently half-wavelength devices with a primary resonance near 1.5 GHz have been fabricated. This design evolution tracks a switch to the half-wavelength topology in an attempt to increase quality factor and resonant frequency. Where possible, both sets have been characterized, but in some cases the limited number of available fabricated chips prevented all types of analysis on all substrates.

At the time of writing, only one of the three oscillator topologies illustrated in Figure 4.10 has been shown to successfully start-up and sustain a countable oscillation. This is the three-inverter Pierce oscillator shown in Figure 4.10(c), which employs the highest gain stage of the three designs. As such, at most eight of the 24 devices in an array are available for characterization and application. Improved FBAR quality factor may enable one or both of the remaining topologies to be utilized, and in future work additional gain must be added to account for resonator and parasitic losses.

4.11.1 S-parameter characterization of on-chip FBAR device

The FBAR mask set includes a standalone FBAR device, which is fabricated in an open area on the far side of the chip. This device can be seen at the top edge of the post-processed die in Figure 4.19(a), where the long ground-signal-ground contact pattern allows access for high-speed probes. The input reflection for this device is shown in Figure 4.21. Sharp peaks at 868 MHz and 2.09 GHz represent two distinct resonances, as detailed for off-chip devices in Chapter 3. The overall shape of the S11 curve, which falls off with increasing frequency, is attributed to the long contact length visible in Figure 4.19(a), which adds capacitance and inductance between the calibrated probe plane and the piezoelectric resonator. There is not sufficient on-chip area available for the fabrication of de-embedding structures.

4.11.2 Active probe characterization of FBAR-CMOS oscillators

Before wire bonding, a post-processed chip was powered through probes for basic characterization. Four DC probes (Cascade Microtech) were used to power the pad ring (3.3V),

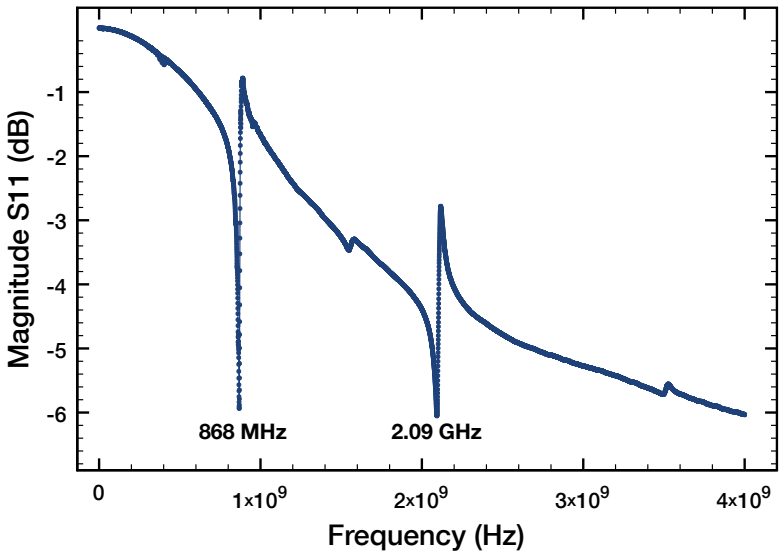

Figure 4.21: A standalone FBAR device is fabricated on chip alongside the integrated array. The measured input reflection S11 plotted here indicates resonances at 868 MHz and 2.09 GHz. The correspond oscillators are measured around 855 MHz.

oscillator rails (1.8V), and oscillator bias points (0V-1.8V). A high-impedance, low capacitance active probe (Picoprobe 35) was used to contact the FBAR structure itself, where oscillations can be measured directly before entering the buffered output and prescaling circuit block. The active probe uses an integrated amplifier to measure signals from DC to 26 GHz while presenting a load of 50 fF and 1.25 MΩ, and this output was connected to a high speed oscilloscope (Tektronix TDS7404) or spectrum analyzer (Agilent E4440A PSA).

Output spectrum

The frequency spectra for two measured oscillators is shown in Figure 4.22. These oscillators are from different chips and different device batches. Narrow peaks at 860 MHz and 1.43 GHz are clearly visible, which demonstrate the fundamental oscillation frequency of each oscillator. This is the nominal frequency at which each will drive its local frequency counter, and this is an important validation of the basic start-up and steady-state behavior of the integrated FBAR-CMOS oscillator design.

A broader spectrum for an integrated oscillator is shown in Figure 4.23(a). This

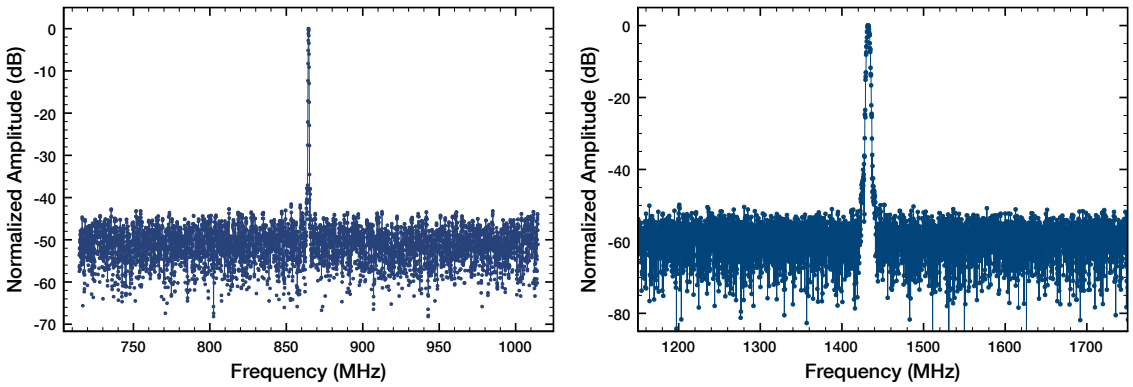

(a) (b)

Figure 4.22: Frequency spectra are measured for integrated FBAR-CMOS oscillators using a high-impedance active probe and a phase spectrum analyzer. The oscillator in (a) has an oscillation frequency on 855 MHz, and the oscillator measured in (b) has a fundamental frequency at 1.44 GHz.

oscillator is from a different device batch, and the FBAR structure has the stack topology of Figure 3.23(a). This measured spectrum shows peaks at 1.48 GHz, 2.97 GHz, and 4.38 GHz, which demonstrate both the fundamental oscillation frequency and the two closest harmonics. These higher frequencies represent harmonics of the oscillator, which are injected by the restoring amplifier and are not indicative of overtones in the resonator itself [74].

A high-resolution spectrum is measured around the fundamental oscillation frequency of an integrated oscillator in Figure 4.23(b). The center frequency is located at 1.4485 GHz, and many close-in sidebands are visible. The closest of these are 350 kHz from the fundamental frequency, with additional sidebands spaced at approximately 1 MHz intervals. There are two primary explanations for this behavior. Young *et al.* demonstrates that very low frequency mechanical resonances are effectively mixed to produce close-in spurious frequency components, in their case separated from a 714 MHz fundamental oscillation frequency by ±20 kHz [138]. A larger body of work from Telschow *et al.* and Ruby *et al.* used laser interferometry to map out Lamb wave modes in thickness-mode FBAR structures, and they found that these lateral modes can present very close to the fundamental resonance frequency with few-megahertz spacing [137, 139–141].

Given the large number of evenly spaced spurious frequency components in Fig-

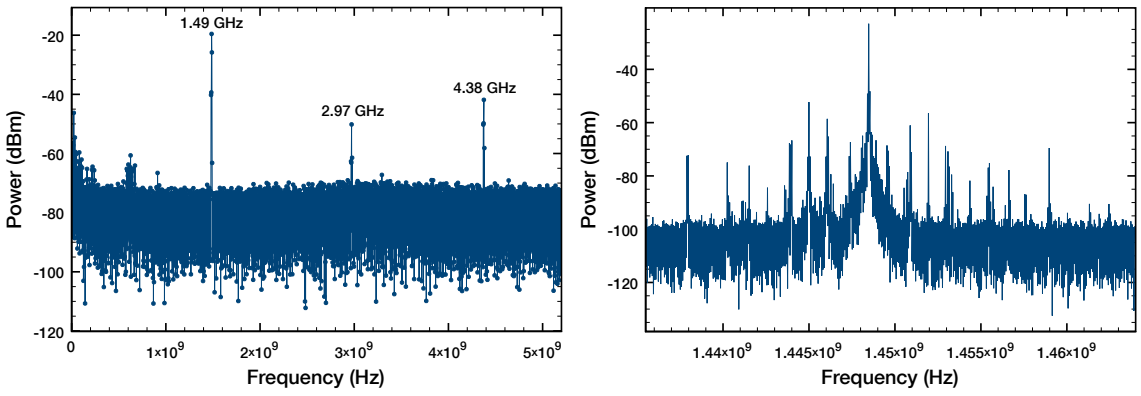

(a) (b)

Figure 4.23: Measured frequency spectra for integrated FBAR-CMOS oscillators with fundamental oscillation frequency near 1.45 GHz. The span in (a) shows first and second harmonics of the fundamental, and the narrow span in (b) shows close-in spurious peaks. These spurious frequencies are attributed to Lamb wave modes in the FBAR structure [137].

ure 4.23(b), the Lamb wave theory is more likely to apply here. As spurious plate modes arise from the geometry of the FBAR device, several groups have taken a structural approach to addressing these unwanted resonances. Kaitila *et al.* has devised a method for mitigation of standing Lamb waves by simple geometric alteration of the active area border region [120], and commercially available FBAR devices employ irregular tetragonal shapes to decrease the number of supported lateral standing wave modes [142].

Phase noise analysis

The phase noise of a feedback oscillator is measured in the frequency domain as the ratio of the signal power P_{sig} at the oscillation frequency $\omega_{\circ}$ to the power at a small offset $\Delta\omega$ from the oscillation frequency [97]. It is commonly quantified in units of dBc/Hz, where dBc is the log ratio of the power at offset $\Delta\omega$ to the power P_{sig} at the carrier frequency. Phase noise was measured for several integrated oscillators with the active probe setup described above. Measurements from typical oscillators are plotted in Figure 4.24, showing plots for an 850 MHz oscillator and a 1.44 GHz oscillator. Phase noise is typically reported at frequency decades, where Figure 4.24(a) demonstrates -112 dBc/Hz at an offset of 1 MHz from the oscillation frequency. This is a convenient way to quantify the skirt around the

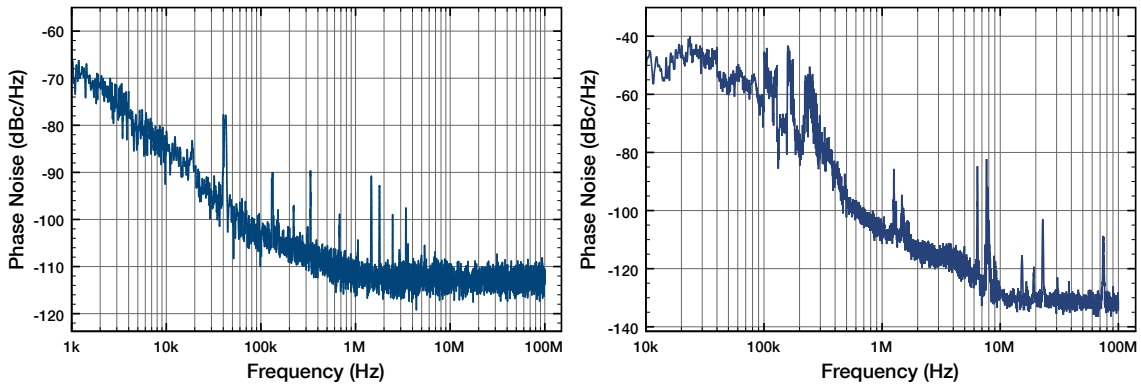

(a) (b)

Figure 4.24: Phase noise measurements from two integrated FBAR-CMOS oscillators. The oscillator in (a) has an oscillation frequency near 850 MHz, and the oscillator in (b) oscillates near 1.45 GHz. The phase noise quantifies the frequency stability of the oscillator.

oscillation frequency as seen in the spectral plots of Figure 4.22 and Figure 4.23.

Extracting quality factor from phase noise

For an oscillator built from a lossy (but otherwise ideal) resonant RLC tank and a noiseless restoring amplifier, the noise from the resistance R as shaped by the feedback circuit can be described as

$$L\{\Delta\omega\} = 10\log\left[\frac{2kT}{P_{sig}}\cdot\left(\frac{\omega_\circ}{2Q\Delta\omega}\right)^2\right] \tag{4.21}$$

where k is Boltzmann's constant, T is absolute temperature, and Q is the quality factor of the resonant tank [97]. This describes a phase noise that falls off as $1/f^2$, which fails to account for any noise floor or for the addition of alternate system noise sources. A real phase noise measurement demonstrates both a noise floor, and a region of noise near the oscillation frequency that falls off with $1/f^3$. An empirical phase noise relationship was developed by D. B. Leeson in 1966 to account for these observations, adapting (4.21) as

$$L\{\Delta\omega\} = 10\log\left[\frac{2FkT}{P_{sig}}\left\{1+\left(\frac{\omega_\circ}{2Q\Delta\omega}\right)^2\right\}\left(1+\frac{\Delta\omega_{1/f^3}}{|\Delta\omega|}\right)\right] \tag{4.22}$$

where F is an empirical correction factor and $\Delta\omega_{1/f^3}$ is the frequency knee at which the phase noise slope changes from $1/(\Delta\omega)^3$ to $1/(\Delta\omega)^2$ [143]. This knee is annotated in the general phase noise shape plot of Figure 4.25, which is the trend described by (4.22).

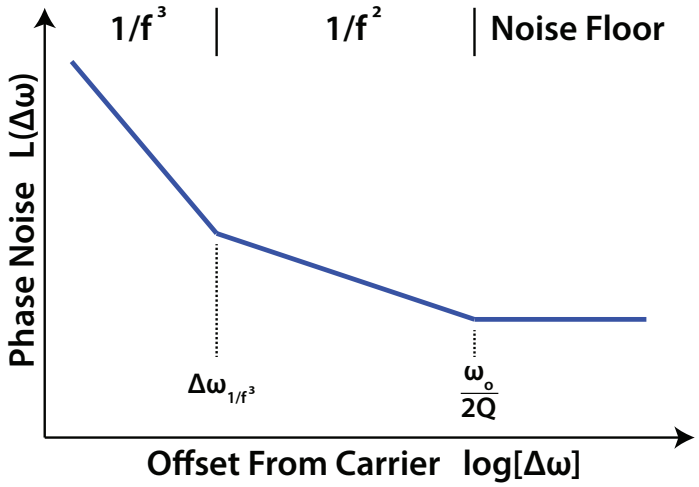

Figure 4.25: Illustration of the shape of the phase noise relationship described by Leeson's equation. The knee that begins the noise floor is used to extract a resonator quality factor from the oscillator.

The three distinct phase noise regions can be divided by slope into a $1/f^3$ region near $\omega_\circ$, a $1/f^2$ region at further frequencies from $\omega_\circ$, and a flat noise floor. The $1/f^2$ region represents the roll-off of resistive noise as it is filtered by the tank, and the $1/f^3$ region results from upconversion of low-frequency noise to the vicinity of the oscillation carrier frequency. A very detailed analysis can be found in [144]. For oscillator design, there are two important results. First, a higher resonator quality factor results in a proportionally lower phase noise. Second, increasing the power P_{sig} of the oscillator decreases phase noise [145].

From the knee at the boundary region between the $1/f^2$ region and the noise floor, depicted in Figure 4.25 as $\omega_\circ/2Q$, we can extract a resonator quality factor from the oscillators measured in Figure 4.24. For the 800 MHz oscillator in Figure 4.24(a), the knee occurs at approximately 2 MHz, which yields a quality factor of Q=212. For the 1.45 GHz oscillator in Figure 4.24(b), the knee occurs at approximately 9 MHz, which yields a quality factor of Q=81. For the higher frequency oscillator, this Q is much lower than the 200-300 typically shown in Chapter 3 for standalone FBAR devices. This may represent an actual Q degradation for the on-chip devices, which could be caused by additional roughness, high-resistance contacts, or poor crystal orientation. However, this can also be an artifact of

the measurement setup. If the noise floor of the measurement equipment (phase spectrum analyzer and active probe) is higher than that of the oscillator, the knee will be artificially moved to a lower frequency.

Ultimately, the frequency resolution of the FBAR-based sensing system will be limited by the Q of the resonator in oscillation. This relationship will be quantified in Chapter 5. It is sufficient to note here that on-chip resonators should be optimized for highest attainable Q and integrated oscillators for lowest phase noise, which depend on both the resonator fabrication itself and on the amplifier and architecture implemented to build a self-sustaining FBAR-CMOS oscillator.

Time domain measurments

Transient signals were measured from an integrated oscillator using the high-impedance active probe and a high-speed oscilloscope. Typical traces are captured in Figure 4.26. The output of the Pierce oscillator, measured as it enters the local output buffer, is shown in Figure 4.26(a). This verifies an oscillation at 1.45 GHz with a peak-to-peak voltage swing of 760 mV. In Figure 4.26(b), the measured output of one of the programmable prescalers is shown. The prescale ratio was set to 64, and the displayed signal has the expected frequency of 22.5 MHz. The peak-to-peak voltage was measured as 2.8 V on a 3.3 V I/O supply.

4.12 Temperature sensitivity of integrated oscillators

The fundamental frequency of an acoustic resonator changes with temperature, and this relationship is quantified by the temperature coefficient of frequency (TCF). The TCF is usually expressed by the ratio [ppm/°C], and it describes a linear shift in frequency for every degree change in temperature of the bulk piezoelectric material [34]. TCF is typically an empirical measurement, in which an acoustic resonator is measured over a range of controlled temperatures, but the underlying physical mechanisms are well-understood. Recall from (3.16) that acoustic velocity is a function of the stiffness constant c_{ii} and the material density ρ, as $V_{ph} = \sqrt{c_{ii}\rho}$. Both stiffness and density are temperature dependent.

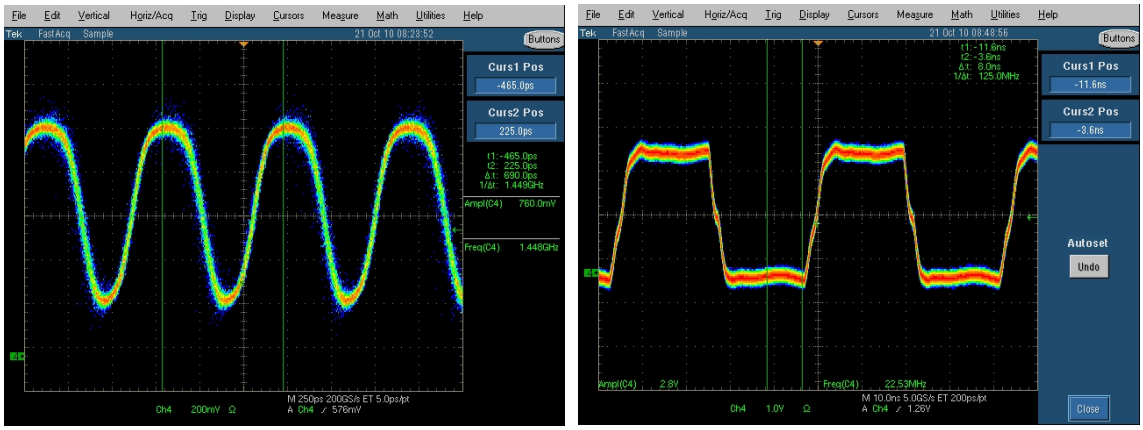

(a) (b)

Figure 4.26: Transient signals are measured for an integrated FBAR-CMOS oscillator using a high-impedance active probe and a high-speed oscilloscope. The oscillator in (a) has an oscillation frequency on 1.45 GHz, and the divide-by-64 prescaler output measured in (b) has a frequency of 22.5 MHz.

Additionally, the frequency of a half-wave resonator is defined by a thickness d, and this thickness is also subject to thermal expansion. Temperature coefficients are applied using the form [146]

$$c'_{33} = c_{33}(1 + TC_{c_{33}} \cdot \Delta T) \tag{4.23}$$

$$d' = \quad d(1 + \alpha \cdot \Delta T) \tag{4.24}$$

with similar equations applied to density, piezoelectric constant, and relative permittivity [147]. In practice, temperature dependence of stiffness (TCc_{33}) and thermal expansion (α) tend to dominate the ensemble effect [146].

For sensing applications, the overall TCF is of critical importance, where frequency drift due to temperature can be larger than frequency shifts induced by attached analyte. In a traditional QCM, the TCF for an AT-cut quartz crystal resonator is 2-3 ppm/°C, which limits frequency drift to a few hertz for well-controlled measurement setups [148]. For a high-frequency BAW device, however, the TCF is typically much higher. Values range from -25 ppm/°C for aluminum nitride to -60 ppm/°C for zinc oxide [146]. This yields ±1 °C frequency drifts measured in kilohertz for a 1 GHz resonator. This sensitivity will degrade the lower limit of detection for a BAW sensor system.

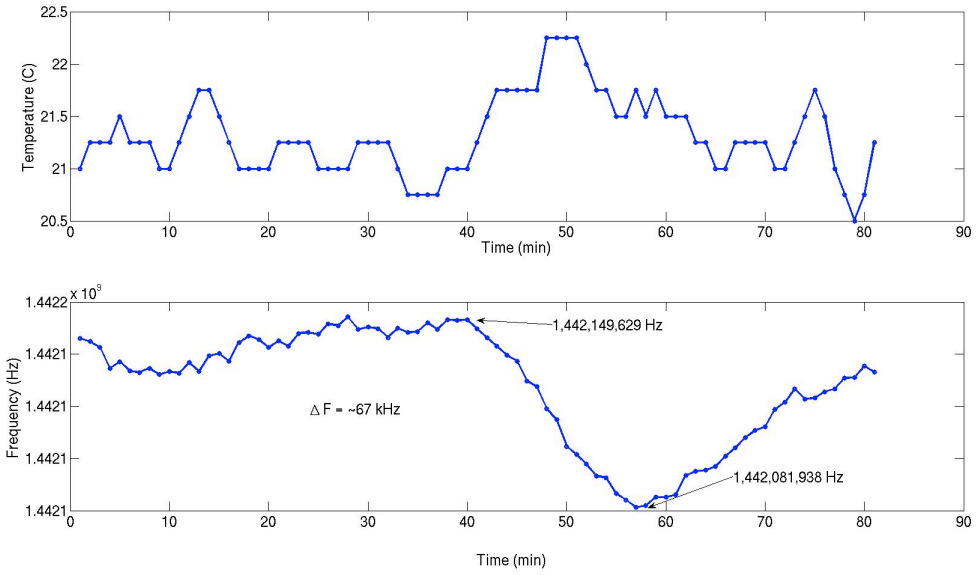

Figure 4.27: The measured frequency drift of an integrated oscillator is plotted alongside temperature. This device has a temperature coefficient of frequency of TCF = -38 ppm/°C.

4.12.1 Temperature coefficient of oscillation frequency

While the TCF of the resonator itself can be extracted from standalone measurements, for a sensor system a more useful parameter is the temperature coefficient of oscillation frequency for the integrated oscillator. This empirical parameter takes into account the ensemble temperature effects of the piezoelectric layer, the acoustic reflector, and the oscillator circuits, all of which are temperature dependent. This can be extracted from a plot of temperature and frequency, as shown in Figure 4.27 for a 1.44 GHz integrated oscillator. Here the measurement tracks a frequency drift that is inversely proportional to the ambient temperature drift with a temperature coefficient of oscillation frequency TCF_{osc} of -38 ppm/°C. This has a lower magnitude than is typically measured for the intrinsic TCF of zinc oxide, which can be attributed to partial compensation from the acoustic reflector. Zinc oxide has a negative TCF of -60 ppm/°C, and silicon dioxide has a positive TCF of 55 ppm/°C; by having silicon dioxide as the top mirror layer, where a non-negligible portion of the acoustic energy resides, the overall TCF_{osc} is reduced [149]. Bjurström *et al.* demonstrated a decrease in TCF magnitude from -31 ppm/°C to ±2 ppm/°C using this technique [148].

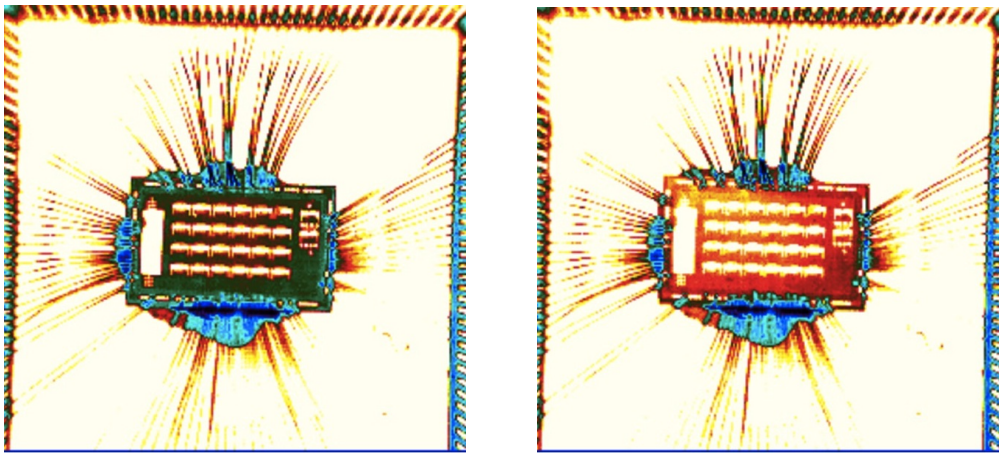

(a) (b)

Figure 4.28: Thermal image from an infrared camera is used to map the spatial temperature distribution across the chip. The image in (a) is of a powered chip at idle, and the image in (b) is taken during a measurement. The change in surface temperature is 0.5-1°C after several seconds of measurement.

4.12.2 Temperature variation of switching CMOS substrate

With integrated FBAR devices subject to a significant TCF_{osc}, self-heating of the CMOS substrate can directly cause a measurable shift in oscillation frequency. Spatial temperature variation can be mapped with an infrared imager, and this is shown for a post-fabricated oscillator array in Figure 4.28. An infrared camera (FLIR Systems) was used with an IR-compatible objective lens to image a chip during both idle and active measurement states. For the image in Figure 4.28(a), the chip is idle. It is powered, and the eight working oscillators and prescale blocks are running, but the local and global 32-bit counters are not switching. For the image in Figure 4.28(b), a measurement is in progress and has been underway for several seconds; both local and global frequency counters are switching. The subsequent temperature increase is clearly visible, and this corresponds to an increase of 1°C in the upper left corner and 0.5°C in the upper right corner over the idle case. An elevated temperate gradient was introduced, which has a magnitude sufficient to cause -27 kHz to -55 kHz frequency shifts in oscillators across the array. Over a long series of measurements, the chip may heat up by several degrees before reaching steady state temperature operation.

The hotspot in the corner of Figure 4.28(b) is attributed to switching in the data

I/O pins. A scaled version of several oscillator outputs is routed to the digital I/O during a measurement. This was implemented as a debug and monitoring feature to bypass the serialized output data path, and it cannot be disabled in the current design.

In practice, self-heating of the CMOS substrate can be mitigated with several techniques for sensing applications. It is important to have a stable, steady-state frequency baseline during a measurement, and both startup drifts and frequency gradients can be tolerated. Self-heating can be limited by pulsing frequency measurements, which allows the substrate to equilibrate between measurements. Conversely, a continuously-operating measurement technique yields an elevated, but stable, substrate temperature.

4.13 Voltage scaling of oscillator frequency

Oscillation frequency is additionally sensitive to oscillator supply voltage. This can be attributed to increased crystal stiffening when the voltage across the FBAR device increases, as described in Section 3.5.2, which causes an increase in resonant frequency for a given device thickness [147]. This effect can be quantified directly by measuring the steady-state oscillation frequency at several different core voltages. The measured results for one such experiment are shown in Figure 4.29 for five 1.44 GHz integrated oscillators.

The 0.18 μm CMOS technology has a nominal core voltage of V_{DD}=1.8V, and here V_{DD} was swept from 1.6V to 2.0V. The region from 1.8V to 2.0V is plotted to demonstrate the local linear trend. The voltage sensitivity of oscillation frequency calculated in this region has an average value measured in Figure 4.29 of 5.1 MHz/V. This translates to 3500 ppm/V for the 1.44 GHz devices measured.

This result has two important corollaries. First, the oscillation frequency will be sensitive to power supply noise, and a noisy supply rail will translate into peak broadening and coupled noise. Second, this voltage sensitivity can be used to counteract the temperature sensitivity with the addition of a control loop, where voltage is continuously adjusted to maintain a constant frequency. Zhang *et al.* has demonstrated a near-complete TCF cancellation with this technique, reducing a measured -112 ppm/°C to +2 ppm/°C [150].

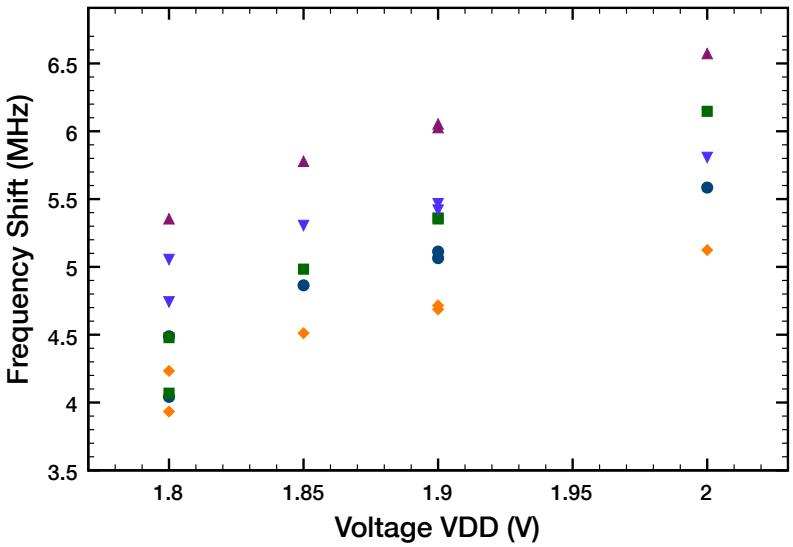

Figure 4.29: Frequency sensitivity to supply voltage for five devices in an array of integrated oscillators. The average sensitivity is calculated as 5.1 MHz/V in the plotted region.

For sensing applications, this method is not directly applicable, but it could be employed with a non-functionalized dummy sensor. For the the devices shown, a V_{DD} increase of 11 mV will counteract the frequency shift induced by every 1°C in temperature increase. The compensation method has not been demonstrated for this platform, but in future work it could be implemented on-chip for fast, active temperature compensation.

4.14 Demonstration of frequency sensitivity to mass addition

Frequency sensitivity of integrated FBAR-CMOS oscillators was demonstrated through a controlled mass series, in which serial additions of silicon dioxide were added to each sensor surface. The results from this experiment are plotted in Figure 4.30 for six oscillator sites in a single on-chip array. This batch had a nominal resonance frequency around 875 MHz, and originally eight oscillators were measured after post-fabrication. Only the six oscillators that successfully completed the mass series are shown.

The fundamental oscillation frequency was measured first as a baseline. Successive layers of silicon dioxide were then added to the resonator surfaces by RF sputter deposition, using standard photolithographic patterning to isolate each of these additions to the

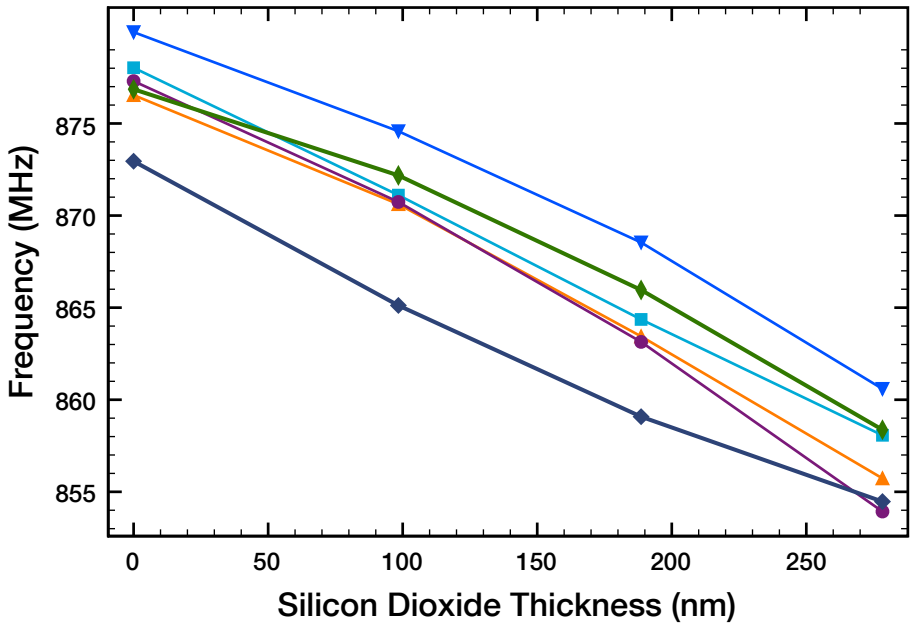

Figure 4.30: Mass sensitivity of the FBAR sensors is demonstrated by the sequential deposition of thin (∼90 nm) layers of sputtered silicon dioxide. This plot shows measured data from six sensors from the array, which demonstrate a baseline resonant frequency spread of 10 MHz.

FBAR sensor area. Each layer had a thickness of approximately 90 nm, and the oscillation frequency of all sensors was recorded after each material addition. From Figure 4.30, we calculate an average mass sensitivity of 3.05×10^{-12} g/Hz·cm^2, which is well above the sensitivity of a typical QCM (6×10^{-9} g/Hz·cm^2) [14] and comparable to previous off-chip FBAR sensors [26].

It is clear from Figure 4.30 that individual sensors may vary by a few percent in nominal resonant frequency (872MHz to 880MHz) before mass addition. This can be attributed to both non-uniform zinc oxide thickness and to non-uniform electrode thickness. These variations may be significant in microwave and communication circuits, but for mass-sensing applications only frequency shift is used to quantify accreted mass. When used in this manner, as shown in Figure 4.31, variation in natural resonance is indiscernible. Error bars in this differential measurement can be attributed in large part to non-uniform deposition of the test masses themselves.

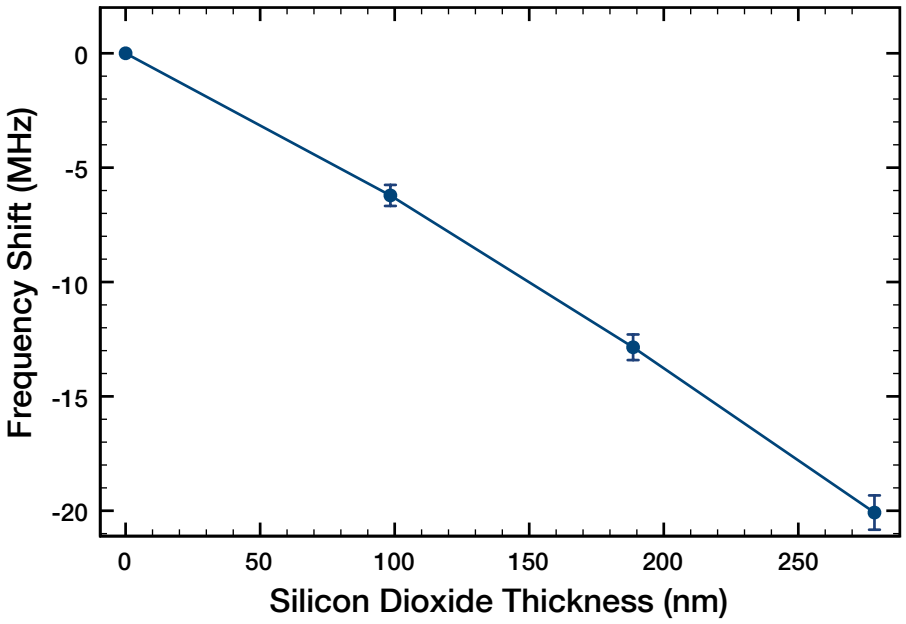

Figure 4.31: Average frequency shift demonstrated by the FBAR array for the sequential deposition of thin (∼90 nm) layers of sputtered silicon dioxide. This shows a sensitivity of 3.05×10^{-12} g/Hz·cm^2.

4.15 Chapter Summary

This chapter has presented the complete design, implementation, and characterization of a custom CMOS chip for the support and measurement of on-chip FBAR-based oscillators. The chip was fabricated in 0.18 μm CMOS, and it supports 24 sensor sites, each with dedicated oscillation and frequency measurement. The electrical model of an FBAR structure was described, and oscillator and frequency counter design constraints were discussed. The FBAR fabrication method developed in Chapter 3 was adapted for post-processing individual CMOS chips, and monolithic resonators were characterized. The mass sensitivity of the integrated sensor platform was measured experimentally as 3.05×10^{-12} gm/Hz·cm^2. The FBAR-CMOS sensor platform will be applied to volatile organic compound detection in the following chapter.

Chapter 5

Volatile organic compound detection with integrated FBAR-CMOS oscillator array

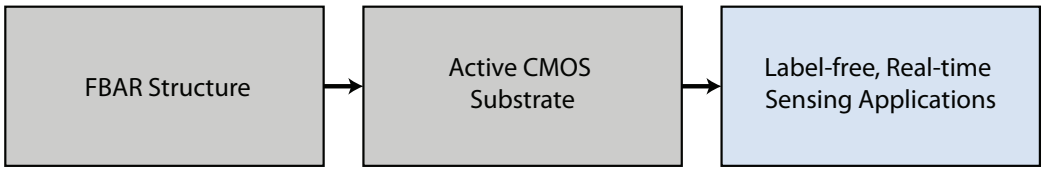

Figure 5.1: Chapter 5 demonstrates the use of the FBAR-CMOS sensor array for application to a real-time, label-free sensing application. Array devices are functionalized for use in quantitative vapor sensing, and platform performance is assessed.

5.1 Introduction

5.1.1 Volatile organic compounds

Both indoor and outdoor air contain quantifiable concentrations of hazardous compounds whose emission stems from both natural and anthropogenic sources [5]. A majority of these are volatile organic compounds (VOC) released by industrial solvents, manufacturing, and decay of plant material [151, 152]. Measuring both environmental release and human expo-

sure to these vapors is critical to their safe, long-term use in industrial applications [151]. Typically, analytical quantification is performed on captured air samples by gas chromatography and mass spectrometry, which was described in Chapter 2. These techniques are sensitive and precise but cannot be employed in real-time monitoring or portable sensing applications.

5.1.2 Polymer-based vapor sensing

Acoustic resonators can be used to detect and quantify volatilized organic compounds using a proportional frequency shift. The change in mass is caused by the absorption of an ambient organic vapor into a thin applied polymer layer. For certain classes of rubbery polymer films, there is a high affinity between target VOC compounds and the polymer material. Commonly employed polymers include polydimethylsiloxane (PDMS), polyisobutylene (PIB), and polyetherurethane (PEUT) for the detection of aromatic hydrocarbons, alcohols, and alkanes [5]. This technique has been applied to several classes of mechanical resonant sensors, including BAW, SAW, CMR and both micron- and nanometer-scale cantilevers [33]. Many of these results were reviewed in Chapter 2, and the basic principle is illustrated in Figure 5.2. In this work, a polymer-based VOC detection method is applied to the FBAR-CMOS sensor platform developed in Chapter 4.

5.1.3 Partition coefficients for vapor-polymer systems

The use of a polymer layer for vapor detection relies on the affinity between the polymer material and the target volatile compound. For absorption, this relation is quantified by a partition coefficient K, which relates absorbed concentration to ambient vapor concentration. This metric describes a specific polymer-solvent pair, independent of the sensing mechanism.

A partition coefficient K is a ratio of the concentration of an analyte in two phases. In this case, it describes steady-state analyte concentration in the polymer film to the concentration of analyte in the surrounding gas, analogous to Henry's Law. At equilibrium,

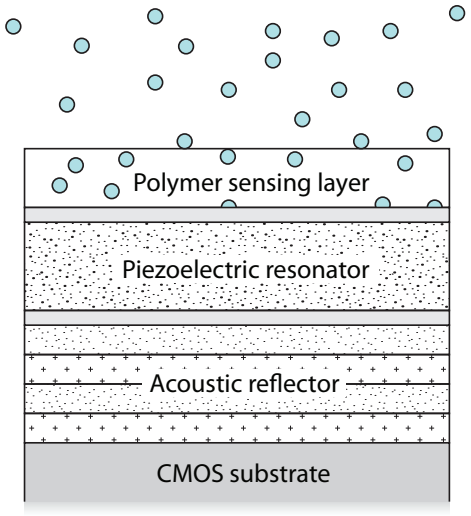

Figure 5.2: Illustration of polymer-based vapor sensing on a solidly mounted FBAR device. A thin polymer layer is applied to the FBAR top surface, where it absorbs ambient organic vapor and induces a frequency shift in the underlying resonator.

the total analyte vapor has been partitioned between a solid phase, absorbed into the polymer coating at a concentration C_s, and a gas phase, in the surrounding chamber at a concentrion C_v. For low concentrations, the partition coefficient is independent of absolute concentration, and it depends only on the polymer, the vapor, and the ambient temperature [153]. We define define the partition coefficient as [123]

$$K = \frac{C_s}{C_v} = \frac{C_{\text{polymer}}}{C_{\text{vapor}}} \tag{5.1}$$

where C_{polymer} and C_{vapor} have matching units of concentration, making K a dimensionless ratio. This ratio is defined at a specific equilibrium temperature.

Despite the fact that partition coefficient K is a function only of the polymer and the VOC analyte, and not of the sensing mechanism, we can empirically determine a partition coefficient from measured sensor values. Extending the derivation of [15], in a manner very similar to [123], we can arrive at the needed equation. This is itself an extension of original work from King *et al.* in 1964 [154].

Consider the basic form of the Sauerbrey equation, written here as

$$\Delta f = s\Delta m \tag{5.2}$$

where Δf is a change in measured frequency, s is a sensitivity factor determined by physical properties of the resonant sensor, and Δm is the attached mass. We can write two such equations for measured values of our polymer-sensor system. The first frequency shift occurs when the polymer sensing layer is itself deposited on a bare FBAR surface, which is described as

$$\Delta f_{\text{polymer}} = s\Delta m_{\text{polymer}} = s\rho_{\text{polymer}} V_{\text{polymer}} \tag{5.3}$$

where $\Delta m_{\text{polymer}}$ is the mass of the polymer layer, ρ_{polymer} is the density of the polymer layer, and V_{polymer} is the volume of the polymer layer. Similarly, for the frequency shift arising from the absorption of a vapor into the polymer layer, we have

$$\Delta f_{\text{voc}} = s\Delta m_{\text{voc}} = sC_{\text{polymer}} V_{\text{polymer}} \tag{5.4}$$

where the solid phase concentration and polymer volume determine the mass of the absorbed analyte. The partition coefficient K is introduced by combining (5.1) and (5.4) to write

$$\Delta f_{\text{voc}} = sKC_{\text{vapor}} V_{\text{polymer}} \tag{5.5}$$

to eliminate the solid phase concentration C_{polymer} from the equation. We can now divide (5.3) by (5.5) to remove s and $V_{polymer}$, which yields

$$\frac{\Delta f_{\text{polymer}}}{\Delta f_{\text{voc}}} = \frac{\rho_{\text{polymer}}}{KC_{\text{vapor}}} \tag{5.6}$$

and is rearranged to form an equation for K

$$K = \frac{\Delta f_{\text{voc}}}{\Delta f_{\text{polymer}}} \frac{\rho_{\text{polymer}}}{C_{\text{vapor}}} \tag{5.7}$$

which is a very usable form for experimentally determining K. With (5.7) we have an equation that can be calculated from measured and known parameters but is independent of the sensor nominal frequency and physical parameters. The relation is a function of only the polymer layer and the VOC analyte. Both $\Delta f_{\text{polymer}}$ and Δf_{voc} are measured directly from experiment, ρ_{polymer} is a known material parameter, and C_{vapor} is calculated from experimental analyte concentration as in (5.15).

Table 5.1: Reported partition coefficients for volatile organic polymer layers. These are calculated from acoustic wave device measurements. Coatings include fluoropolyl, polydimethylsiloxane (PDMS), and polyetherurethane (PEUT), and organic compounds include toluene, octane, and dimethyl methylphosphonate (DMMP).

Sensor	**Polymer**	**Organic Compound**	**log (K)**	Reference
SAW	Fluoropolyol	Toluene	2.9	[123]
SAW	Fluoropolyol	n-Octane	2.1	[123]
SAW	Fluoropolyol	DMMP	6.3	[123]
QCM	PDMS	n-Octane	3.4	[155]
QCM	PEUT	n-Octane	2.8	[155]
QCM	PEUT	Tetrachloroethene	3.3	[155]

The expression (5.7) will be used in Section 5.3 for the calculation of partition coefficients from experimental data, and a variety of bulk acoustic wave, surface acoustic wave, and cantilever devices have been employed to characterize K values for various polyer-vapor pairings. A sampling of these is shown in Table 5.1.

5.1.4 Multicomponent vapor detection method

Array-based vapor sensing is motivated by multicomponent detection applications, in which an unknown vapor is identified from a set of possible compounds. Individual sensors are coated with different polymer types, each of which has a different partition coefficient for a set of target vapors. By measuring frequency shifts simultaneously across the array, classification and quantification of multi-component vapor samples is possible [156].

To illustrate this principle, consider two sensors coated with polymers P_1 and P_2 and two target vapors A and B. The partition coefficients for the four polymer-vapor pairings are measured, which define the linear relationships illustrated in Figure 5.3. The relevant slopes are given as α_1, β_1, α_2, β_2. For the simple case of identifying either A or B, assume that both sensors are in the same isolated environment and an unknown concentration of A or B is introduced. At equilibrium, a frequency shift is measured from each sensor, yielding Δf_1 and Δf_2. In this case, each sensor provides two possible concentration values, CA_i and CB_i, and one pair describing A or B will be equal. For the example in Figure 5.3, the

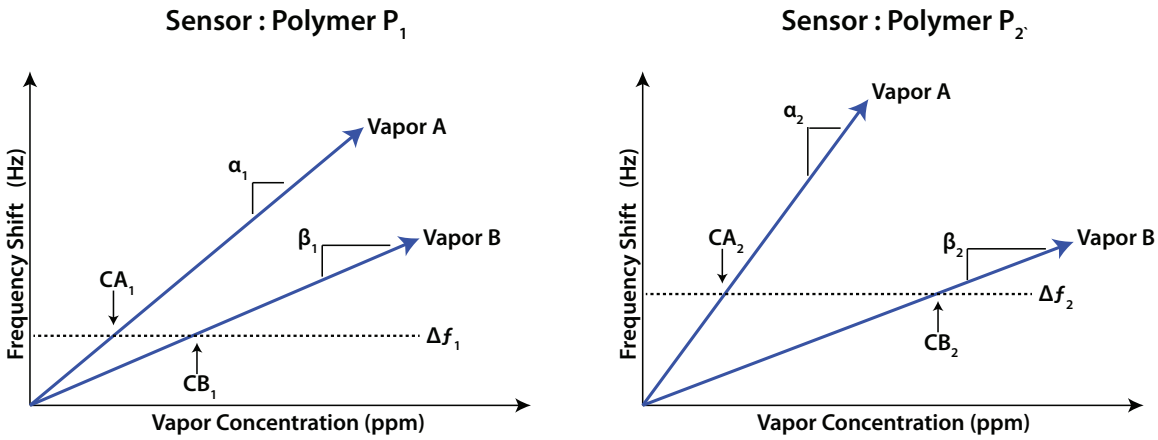

Figure 5.3: Illustration of the simplest form of multicomponent vapor detection using polymer absorption. Two polymer-coated devices are characterized for frequency sensitivity to two vapor species. These concentration curves then can be used to extract the concentration of each vapor from an unknown mixture of the two species.

matching pair indicates that vapor A is present with a concentration $C_A = CA_1 = CA_2$.

For low concentrations, partition coefficients are independent [153]. A polymer will absorb multiple organic compounds, each according to the relevant partition coefficient, and the resulting frequency shift will be a superposition of these values [157]. The simple case of Figure 5.3 can be extended by including an unknown *mixture* of vapors A and B, where the total frequency shift for each sensor can be described by the linear sums

$$\Delta f_1 = \alpha_1 C_A + \beta_1 C_B \tag{5.8}$$

$$\Delta f_2 = \alpha_2 C_A + \beta_2 C_B \tag{5.9}$$

for which Δf_1, Δf_2, α_i, and β_i are experimentally determined, leaving two equations and two unknown variables C_A and C_B. For the simple case of two polymers and two vapors, this is sufficient information by which to quantify the concentration of each vapor in the mixture.

In practice, few applications have such a constrained sample space, and few polymer pairs perform as cleanly at the illustrations of Figure 5.3. Instead, a wide variety of polymers are applied in concert and measured against many different organic vapors, and multivariate analysis and decomposition techniques are used to analyze the corresponding

vapor 'fingerprints'. A unknown vapor can then be separated into its relevant class and concentration. Class determination (aliphatic, alcohol, alakane, etc.) is more tractable than exact species identification, given the lack of very specific polymer-vapor interactions [157].

Carey *et al.* demonstrated a multicomponent detection technique in 1987 [158]. Nine QCM sensors were each coated with a different absorbing polymer, and the concentration-dependent frequency shifts were measured for seven different vapors. Multiple linear regression and partial least squares techniques were used to analyze both two-component and three-component vapor mixtures. For the three-component case, worst-case concentration prediction with an average error of 10.1% was reported, and in most cases the performance was even better.

More recently, Si *et al.* used a similar setup with eight polymer coatings on QCM to classify a set of eight volatile organic compounds [159]. Principle component analysis was employed to separate unknown vapors into polar and non-polar classes, and partial least squares was used to quantify concentrations of a two-component gas mixture with a correlation of 0.96 or better. Many other examples of such techniques have been published, including QCM, SAW, and contour mode resonators and a wide variety of multivariate and neural network data processing techniques [52, 123, 157, 160].

The methods and applications described in this section are intended to provide a broad perspective on acoustic wave vapor sensors, and a more detailed discussion of these methods is left to the references. The remaining sections will describe experimental results using polymer-coated integrated FBAR structures on CMOS for vapor sensing, which provide early evidence that this platform could be similarly extended and employed to multicomponent applications. By extended the number of polymers from a few to a few dozen, as enabled by dense FBAR arrays, more accurate identification and a lower limit of determination can be expected.

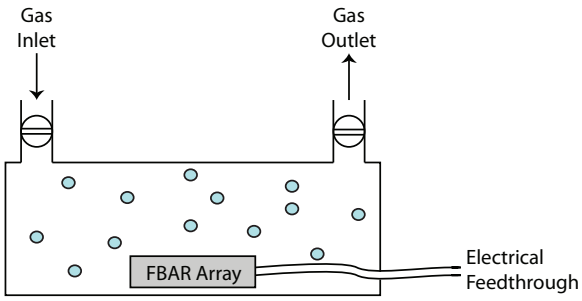

Figure 5.4: Illustration of a typical experimental arrangement for controlled vapor concentration experiments. The sensor platform is enclosed in a sealed chamber, and ports allow for the introduction of both test vapors and a purge gas. The chamber is typically glass or metal to avoid significant adsorption of organic compounds, which can be observed with plastic [161].

5.2 Vapor sensing experimental setup

The primary aims of a single-vapor sensing experiment on an acoustic wave device are to quantify a frequency shift in response to a steady-state change in vapor concentration, and to show that this shift is proportional to concentration. This section details system components required to achieve these aims, and a method for producing a controlled, ambient environment with a known and controllable vapor concentration is described.

The basic vapor sensing setup is illustrated in Figure 5.4. An acoustic wave sensor is placed in a sealable chamber and interrogated by electrical means. An inlet port is used for the introduction of both test organic vapors and purge gas, and an exhaust port is used for vapor removal and optional evacuation. Vapor concentration experiments may be conducted in vacuum or carrier gas environment. For comparison to real-world applications, dry nitrogen or an air-like synthetic gas mixture is typically employed as carrier [161].

For a concentration series, a vapor of known concentration is introduced, and the dose chamber is sealed until until a steady-state frequency reading is measured for the acoustic sensor. The chamber is purged with carrier gas until the frequency returns to baseline, at which point the process is repeated at a different concentration.

5.2.1 Dose chamber apparatus

Vapor dose chambers for sensor testing can be broadly divided into two types, static and dynamic dosing [161]. In a dynamic setup, a volatile organic compound is evaporated and combined with a carrier gas before injection into the sample chamber. This can be accomplished through headspace sampling (bubbler) or through large evaporation bags or bins. Flow control is handled by one or more mass flow controllers and electronically actuated valves. During a measurement, a carrier gas with a known concentration of VOC is continuously flowed through the test chamber.

In a static dosing system, a sample is injected into a closed chamber and allowed to come to equilibrium. Typically, the sample is injected as a small volume liquid, on the order of micro-liters of sample per liter of chamber for ppm-range concentrations. This enables a very accurate calculation of vapor concentration, as is detailed in Section 5.2.2, and the system complexity is low. The primary limitation of a static dose chamber is its lack of pre-evaporation. A sensor step response, limited by absorption into the polymer, cannot easily be separated from evaporation rate, as the two mechanisms occur simultaneously.

For the experiments described here, a static setup was chosen for its simplicity and reliability. This experimental setup is shown in Figure 5.5. The chamber was constructed from a three-liter glass reaction vessel (Chemglass Life Science), and it employs a four-port separable lid with ground glass connections. These ports are used for nitrogen purge inlet, test compound injection, electrical feedthrough, and primary sensor access. Rubber septa are used on the injection port and electrical feedthroughs to enable a sealed system, and a teflon stopcock is used to isolate the purge inlet. A small fan was installed inside the chamber to hasten evaporation and to assure a homogenous steady-state concentration. The dose chamber is insulated from the ambient environment, and a gravity flow controller is used to regulate the purge gas. Nitrogen is used both as purge gas and as experimental background gas. For injection volumes below 10 μL, a micro-syringe is used for sample delivery, and a standard pipette is used for larger volumes.

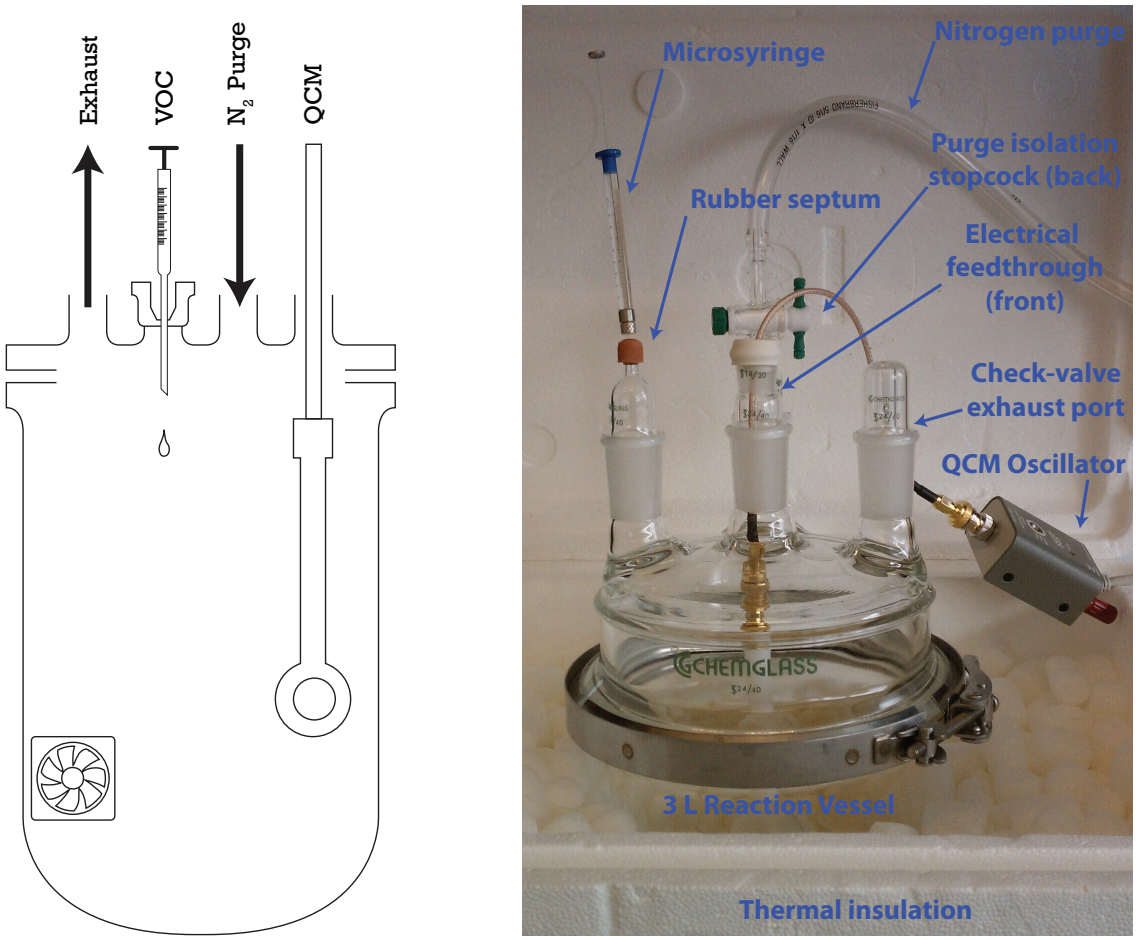

(a) (b)

Figure 5.5: Static dosing chamber for testing of QCM under varying vapor concentrations. A three-liter glass reaction vessel is used to create a sealed environment. Ports allow for solvent injection, purge gas inlet and outlet, and electrical feedthrough for the QCM fixture and enclosed fan.

5.2.2 Evaporated vapor concentration

In a static dose chamber, a small volume of liquid organic solvent is injected into a sealed chamber. The liquid will fully evaporate as long as the concentration is below the saturating vapor limit. For a fixed chamber volume, this evaporated vapor concentration can be accurately calculated.

The concentration of an evaporated VOC is typically expressed in parts per million (ppm). For an ideal gas, volume and molar ratios are identical, and either can be used to calculate the amount of organic compound required for a target concentration [162]. It is important to distinguish between mass/mass and mole/mole ratios when using ppm and similar dimensionless units. All calculations here are given as mole/mole ratios, which are equivalent to volume/volume ratios in the case on an ideal gas.

Consider a concentration y_{ppm}, which indicates y_{ppm} parts in one million parts, by mole, of a larger carrier component (e.g. sample vapor in an air carrier). For a vapor at one part per million, we would have

$$1\ ppm = \frac{\text{moles of VOC}}{\text{moles of air}} = 10^{-6} \tag{5.10}$$

which is extended to multiple parts per million y_{ppm} as

$$\frac{y_{\text{ppm}}}{10^6} = \frac{\text{moles of VOC}}{\text{moles of air}} \Rightarrow y_{\text{ppm}} = \frac{10^6 \cdot \text{moles of VOC}}{\text{moles of air}}. \tag{5.11}$$

Let M_{voc} be the molecular weight of our target compound [g/mol], let x_{voc} be the mass of the target [g] compound injected into the chamber, let V_{chamber} be the test chamber volume [L], and let $V_{\text{stp}} = 24.5$ L/mol be the standard volume of one mole of gas at standard temperature and pressure, in this case one atmosphere and $298K$. Now consider:

$$\frac{V_{\text{chamber}}}{V_{\text{stp}}} = \text{moles of air},\ \frac{x_{\text{voc}}}{M_{\text{voc}}} = \text{moles of VOC} \tag{5.12}$$

We can combine (5.11) and (5.12)

$$y_{\text{ppm}} = \frac{10^6\ x_{\text{voc}}\ V_{\text{stp}}}{V_{\text{chamber}} M_{\text{voc}}} \tag{5.13}$$

Table 5.2: Calculated injection volumes for toluene using a 3 L test chamber at standard temperature and pressure. Toluene has a molar mass of M_{voc}=92.14 g/mol and a fluid density of ρ_{voc}=0.8669 g/mL [161].

Target Concentration ($\mu g/L$)	**Concentration (ppm)**	**Injection Volume**
376 $\mu g/L$	100 ppm	1.3 μL
1128 $\mu g/L$	300 ppm	3.9 μL
1880 $\mu g/L$	500 ppm	6.5 μL
2633 $\mu g/L$	700 ppm	9.1 μL
3385 $\mu g/L$	900 ppm	11.7 μL

which is rearranged to solve for x_{voc} as

$$x_{\text{voc}} = \frac{y_{\text{ppm}} V_{\text{chamber}} M_{\text{voc}}}{10^6 V_{\text{stp}}} \tag{5.14}$$

which calculates the mass of the required liquid injection for a target concentration of y_{ppm}. Note that the equivalent gas concentration [g/L] for a given parts-per-million concentration is calculated as

$$\frac{x_{\text{voc}}}{V_{\text{chamber}}} = \frac{y_{\text{ppm}} M_{\text{voc}}}{10^6 V_{\text{stp}}} = C_{\text{vapor}}. \tag{5.15}$$

Let ρ_{voc} be the liquid density of our target VOC compound in [g/mL], which is used with (5.14) to solve for the liquid injection volume V_{voc} as

$$V_{\text{voc}} = \frac{x_{\text{voc}}}{\rho_{\text{voc}}} = \frac{y_{\text{ppm}} V_{\text{chamber}} M_{\text{voc}}}{10^6 \rho_{\text{voc}} V_{\text{stp}}} \tag{5.16}$$

for a target evaporated concentration of y_{ppm} at room temperature.

From Equation (5.16) we can quickly calculate the volume of liquid organic to inject into our static chamber to achieve a given equilibrium concentration. A sample set for toluene is calculated in Table 5.2 for a concentration series from 100 ppm to 900 ppm.

5.3 Sensing experiments on a quartz crystal microbalance

For polymer-based sensing on an acoustic resonator, the polymer film must be thin compared to the bulk piezoelectric thickness to mitigate the loading and quality factor degradation. For a 10 MHz quartz crystal, sensing films are typically applied in thicknesses from 250 nm

to 1 μm [159, 163], and for higher frequency BAW and SAW devices the coatings are much thinner, from 25 nm to 90 nm [156]. To apply a uniform polymer coating, standard thin-film application methods have been previously employed, including spin-coat, spray-coat, dip-coat, drop-coat, and chemical vapor deposition [15, 32, 156, 159, 163]. For an integrated sensor array on a packaged CMOS chip, not all of these methods are feasible.

In this section, a commercial quartz crystal microbalance is used to develop a spray-coat deposition method. The polymer-coated QCM system is employed for vapor sensing experiments to qualify the dose apparatus and measure polymer sensitivity. These experiments directly demonstrate the effect that is replicated on a smaller scale on the integrated polymer-coated FBAR devices in Section 5.4.

5.3.1 Spray-coating quartz crystals

Polydimethylsiloxane (PDMS) was used as a target polymer layer, which has previously demonstrated strong sensitivity to toluene, octane, and other benzene derivatives, and it is commonly employed in acoustic sensing applications [156]. PDMS must be diluted for spray-coating, and Choonee *et al.* have demonstrated uniform, few-micron film deposition for MEMS passivation applications using either hexane or polymer-based diluents [164]. Hexane was chosen specifically for its high volatility, where they propose that the hexane may evaporate from the aerosolized PDMS solution before the droplets reach the crystal surface. Their method has been adapted here for uniform films at sub-micron thickness.

For this work, Sylgard 184 Silicone Elastomer (Dow Corning), a common two-part PDMS mixture, was diluted in hexane. The ratio of PDMS to curing agent was always 10:1 by weight, with varying amounts of hexane used to dilute the PDMS for different spray viscosities. Dilution was done at room temperature with constant stirring, and dilute solutions produced curable films after a month or more of shelf storage. A subset of the recipes tested are listed in Table 5.3.

A gravity-fed spray gun (DeVILBISS) was used with a nitrogen carrier gas for the spray-coating. Clean 5 MHz quartz crystals were sprayed in multiple passes from a distance

of 6"-8" using the dilutions in Table 5.3, and PDMS coatings were cured overnight at 90°C. The individual crystal frequencies were measured before and after polymer application with an oscillator and frequency counter (Stanford Research Systems QCM200), and these values are listed in Table 5.4. The thickness of an applied film can be approximated by the Sauerbrey equation (5.2), which we rewrite in the form

$$\Delta f = -C_f \cdot \Delta m \tag{5.17}$$

where Δm is the mass *per area* of the applied polymer layer and C_f is a sensitivity constant given by the QCM manufacturer as C_f=56.6 Hz·cm^2/μg. This sensitivity is comparable to that calculated from quartz material parameters. The film thickness d can be derived from the mass per area Δm and the density ρ as $d = \Delta m/\rho$, which is substituted into (5.17) to yield

$$d = -\frac{\Delta f}{\rho \cdot C_f} \tag{5.18}$$

and is accurate for thin applications. Cured PDMS has a density ρ=0.965 g/cm^3, which was used to calculate the applied film thickness in Table 5.4. For the 5 MHz crystals used, the frequency shift was approximately -550 Hz per 100 nm of applied PDMS.

5.3.2 Experimental results

Toluene concentration series

To perform a concentration experiment, the chamber is first purged with nitrogen at 15 scfh until a steady-state response is achieved, at which point the purge line is closed and the chamber has a sealed nitrogen environment. A small volume of liquid organic sample is

Table 5.3: Diluted polymers used for spray-coating 5 MHz quartz crystals.

Dilution Ratio (Diluent:Polymer)	**Hexane**	**PDMS**
10:1 (Stock Solution)	30g	3g PDMS, 0.3g Curing Agent
100:1	30mL	3mL 10:1 Stock Solution
1000:1	30mL	300μL 10:1 Stock Solution

Table 5.4: Spray-coated polymer solutions as applied to quartz crystal surfaces. The frequency shift of the coated resonator is used to estimate the thickness of the applied layer.

Crystal	**Dilution**	**Spray Time**	**$f_\circ$ Before**	**$f_\circ$ After**	**Δf**	**Thickness (nm)**
Control	-	-	5009618 Hz	5009616 Hz	-2 Hz	0.3
#1	100:1	30 s	4965076 Hz	4960460 Hz	-4,616 Hz	815 nm
#2	1000:1	16 s	4987086 Hz	4985850 Hz	-1,216 Hz	214 nm
#3	100:1	23 s	4964354 Hz	4960719 Hz	-3,645 Hz	643 nm
#4	100:1	60 s	4986395 Hz	4976250 Hz	-10,145 Hz	1,792 nm

then injected into the chamber through a rubber septum, where it evaporates in the fixed volume as calculated by (5.15). After steady-state frequency shift has been reached, the chamber is again purged with a nitrogen flow.

Using the PDMS-coated crystal (#4) from Table 5.4, a detailed concentration series was run to measure the toluene-PDMS partition coefficient. Prior to the first injection, the QCM system was powered on and allowed 90 minutes to equilibrate. Toluene injections covered approximately one decade of concentration (70-700 ppm). Each injection was given 2 minutes to equilibrate, 90 seconds nitrogen purge at 30 scfh, and 30 seconds idle before the next injection. A total of 17 injections were measured over a two hour period. Measured results are plotted in Figure 5.6.

From the data in Figure 5.6, a MATLAB script was used to extract the frequency shift for each injection. This is a simple way to mitigate the baseline drift, assuming that this drift is dominated by temperature drift and not by residual absorbed toluene. The script finds each shelf in the data and averages an adjustable window of points just before this step to determine the mean steady-state frequency. A frequency shift from mean baseline to mean stead-state aborbsed frequency is then calculated for each toluene injection.

The extracted frequency shift versus toluene concentration is plotted in Figure 5.7. At each concentration, points lie almost atop each other, and the overall correlation is $R^2 = .99$. The equation of the line shown in Figure 5.7 has a slope of -0.03187 Hz/ppm, which can be used to calculate the partition coefficient. The partition coefficient equation

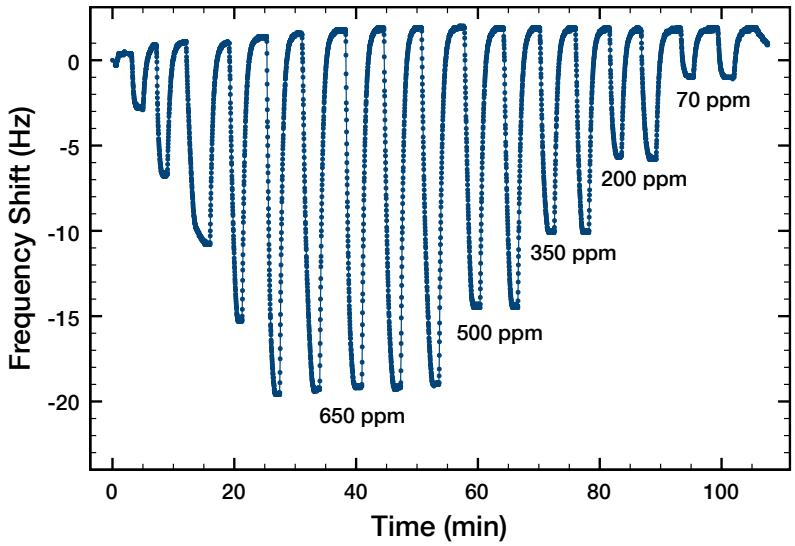

Figure 5.6: Toluene concentration series on spraycoated 5MHz QCM crystal. Annotated concentrations are approximate. Actual calculated concentrations (ppm) are: 70.4, 211.3, 351.5, 492.3, 632.5.

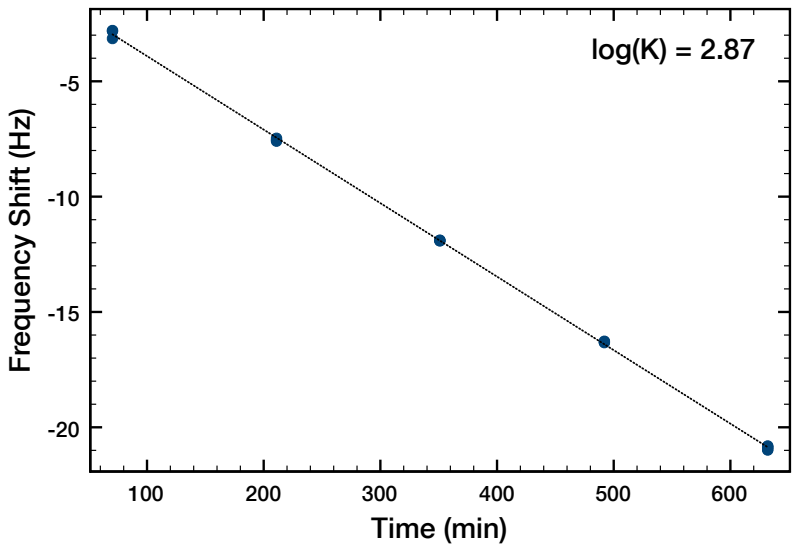

Figure 5.7: Frequency shift vs. concentration for toluene vapor and PDMS. This data is extracted from the series shown in Figure 5.6. The slope is -0.03187 Hz/ppm, which gives a calculated partition coefficient $\log(K) = 2.87$.

(5.7) and the vapor concentration (5.15) can be combined as

$$K = \left(\frac{\rho_{polymer}}{\Delta f_{polymer}}\right)\left(\frac{\Delta f_{\mathrm{voc}}}{y_{ppm}}\right)\left(\frac{10^6 \cdot V_{STP}}{M_{VOC}}\right) \tag{5.19}$$

where the middle term describes the slope of the concentration in Figure 5.7. This was used to calculate a partition coefficient for toluene and PDMS of K = 737 and $\log(K) = 2.87$. This value is identical to that seen in the literature for the toluene-PDMS pairing measured on a SAW sensor [156].

Nonlinear sensitivity at higher concentrations

The concentration trend in Figure 5.7 is very linear in the region from 70 ppm to 700 ppm for toluene absorption in PDMS. For higher concentrations, the absorption behavior of organic solvents into rubbery polymers is known to be nonlinear [165]. Both increasing and decreasing sensitivity have been reported for increasing vapor concentration. Pei *et al.* demonstrate a saturation behavior for increasing concentrations of DMMP on a QCM system [21], while Bodenhofer *et al.* and finds the opposite trend for octane absorption in PEUT [155]. These nonlinear behaviors are not well understood, but each is repeatable for a given solvent/polymer/sensor combination.

An extended toluene concentration series was performed to investigate nonlinearities in frequency sensitivity to toluene for the PDMS-coated quartz crystal. Toluene vapor concentration ranged from 70 ppm to 10,000 ppm. Injection and purge steps were 3-4 minutes each, and a total of eleven concentrations were measured. The results are plotted in Figure 5.8. A saturation effect is observed for the measured sensor at concentrations exceeding a few thousand parts per million. For sensing applications, this will limit the sensitivity at high vapor concentrations

5.4 Vapor sensing experiments on FBAR-CMOS array

The vapor experiments performed with a commercial QCM are repeated with the integrated FBAR-CMOS oscillators to demonstrate their use for vapor sensing applications. This

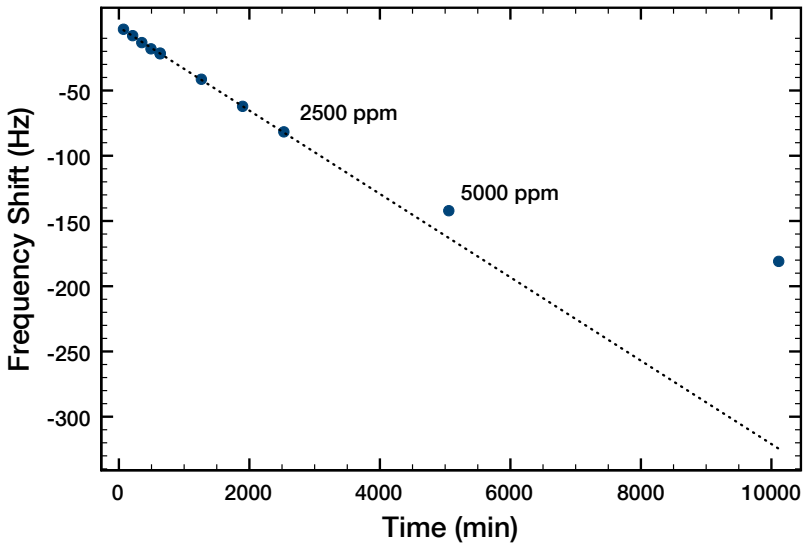

Figure 5.8: For high concentrations of toluene, the sensor response is nonlinear. This concentration series for toluene in PDMS on a 5 MHz QCM shows a saturation effect.

section details the polymer application method adapted for individual integrated FBAR devices, and vapor concentration experiments are reported.

5.4.1 Micropipette application of polymer sensing layers

For an array of sensors, it is important to be able to functionalize each structure independently of its neighbor. This might be used for multi-component applications, as described in Section 5.1.4, or it might be used to functionalize only a subset of devices to retain some for bare control measurements. The spray-coat method developed for use on QCM might be employed through careful shadow-masking, but an alternative drop-coat process was developed for more accurate, localized functionalization. This section describes the use of glass micropipettes for precise, small-volume application of dilute polymer solutions.

Pulling a small-diameter glass capillary tube down to a micron-scale tip diameter creates a micropipette, which is commonly used for the injection or extraction of small volumes of material to or from individual cells [166]. For this application, a 1.5 mm O.D. / 0.86 mm I.D. borosilicate glass capillary tube was pulled to few-micron tip using a pipette

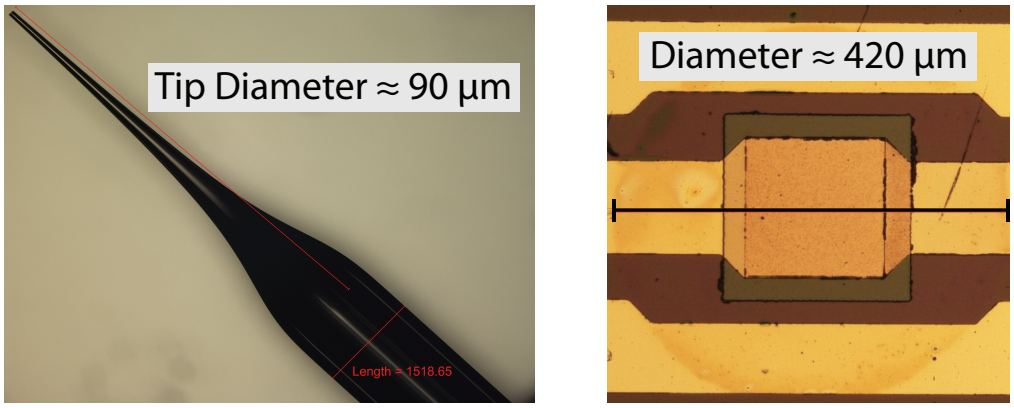

(a) (b)

Figure 5.9: A pulled micropipette is shown in (a), with a final tip diameter of approximately 90 μm. A standalone FBAR device is shown in (b) after application of a thin PDMS layer; a faint outline of the circular spot is visible, and the spot diameter is 420 μm.

puller (Sutter P-95). A glass-glass break was used to achieve a final tip diameter of approximately 100 μm. The micropipette was then used with a precision pneumatic injector and manipulator arm to apply small volumes of dilute polymer solutions to individual FBAR top surfaces.

Uncured PDMS (Sylgard 184 / Dow Corning) was mixed in a 10:1 ratio by weight with its curing agent and diluted many-fold in an organic solvent; typical dilution ratios used span 100:1 to 500:1 (solvent:PDMS) by weight. Polyisobutylene (PIB) (Sigma Aldrich) was dissolved in either hexane or toluene while stirring; this dissolution can take several hours at room temperature. Spot application was performed under a light microscope with a pneumatic micro-injector (Narishge IM 300) and a micro-manipulator arm (Burleigh / ThorLabs). A sample PDMS application test on a standalone FBAR device is shown in Figure 5.9.

Polymer film thickness and spot diameter can be controlled as a function of dilution ratio, solvent selection, and injection pulse. For thinning, PDMS is commonly diluted with hexane, toluene, or tert-butyl alcohol (TBA) [167], all of which have been tested here for use with FBAR devices.

Toluene and hexane have proven very effective for use in the micropipette setup.

Table 5.5: A summary of a polymer spotting tests on standalone FBAR devices.

Polymer	**Diluent**	**Ratio**	**Avg. Δf**	**n**	**σ**	**Thickness**
PDMS	Hexane	1:250	-6.1 MHz	3	1.9 MHz	24.2 nm
PDMS	Hexane	1:500	-3.6 MHz	3	350 kHz	14.3 nm
PIB	Toluene	1:240	-22.8 MHz	3	3.7 MHz	98.5 nm
PIB	Toluene	1:480	-10.2 MHz	3	3.7 MHz	44.0 nm
None			-17 kHz	3	41 kHz	Control

It was found that hexane wets more readily to the chip surface and evaporates quickly, whereas toluene creates smaller-area spots (for a given dilution ratio) and significantly increases PDMS curing time. The use of TBA as a diluent for micropipette application of PDMS yielded poor results; with a melting point near room temperature, very dilute solutions tended to solidify in the capillary and clog the pipette tip.

The thickness of an applied polymer layer is estimated from the frequency shift caused by its addition to an FBAR top surface according to (5.18). The sensitivity constant C_f for a zinc oxide resonator is calculated from material parameters as C_f= -2.61 Hz·cm^2/pg. A selection of spotting tests on standalone FBAR devices are summarized in Table 5.5. The spotting process has a high degree of variation, which is attributed to large variability in the liquid volume dispensed by the micro-injector. A standard micropipette system is usually employed for aqueous solutions. Organic solvents have significantly different wetting properties and lack the strong surface tension of water, which makes droplet formation variable for the dilute polymer solutions.

For the vapor sensing results shown in this section, a hexane-PDMS solution with a 500:1 dilution ratio was applied, yielding polymer spots 200 μm to 600 μm in diameter. For measurement, only spots that allowed access to the GSG electrodes could be characterized, which requires a spot size smaller than 500 μm. Applied polymer films were cured overnight at 100°C. Degradation in quality factor (Q) after application of a thin PDMS layer was small, with a typical resonator showing a decrease from 211 to 171 after spotting.

The micropipette spotting method is applied to integrated FBAR structures on

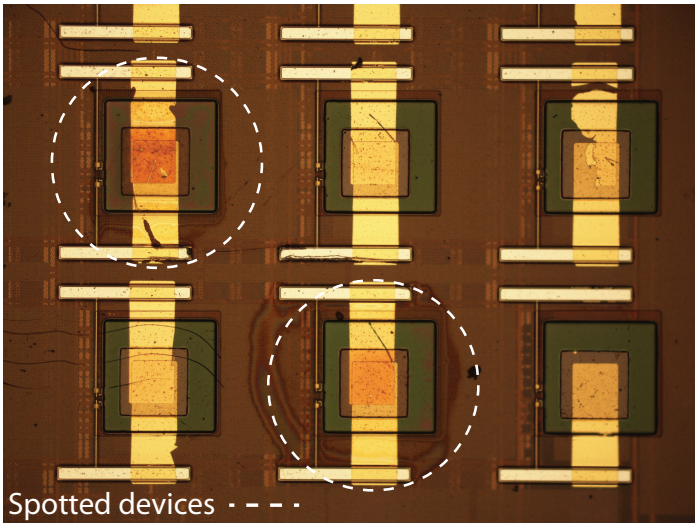

Figure 5.10: Microscope images of an on-chip FBAR array. The two indicated devices have been coated with a thin layer of PDMS from a 500:1 (Hexane:PDMS) solution.

CMOS in an identical manner. In this case, the spot diameter must be kept below 500 μm to avoid covering multiple sensors, but no allowance must be made for keeping contact areas clear. Two functionalized devices in a post-fabricated array are shown in Figure 5.10.

5.4.2 Experimental setup

Dose chamber arrangement

The dose chamber described in Section 5.2 was also used for the FBAR-based vapor sensing experiments. The arrangement was altered from that used for QCM-based sensing, where the sensor was located inside the dose chamber. For the FBAR-based device, this would require enclosing all of the active PCB circuitry within the sealed chamber. This introduces an additional 120 mW of dissipated power, raising the internal chamber temperature by several degrees and requiring several hours to reach thermal equilibrium. To avoid this, the ceramic chip carrier was sealed against an opening of the reaction vessel, as illustrated in Figure 5.11. The PCB was kept external to the chamber, and only the chip power dissipation was introduced into the dose environment. This arrangement was verified by QCM with a toluene series to confirm that sensitivity measured at the chamber port is the

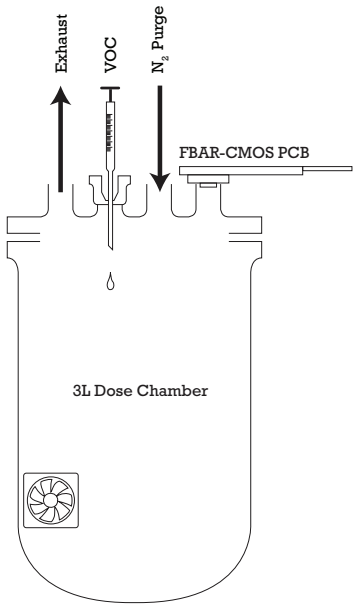

Figure 5.11: The experimental setup is altered to allow the post-fabricated chip to sense ambient vapor concentration through a chamber port. The printed circuit board is kept external to the measurement chamber to mitigate its effect on ambient chamber temperature.

same as that measured within the chamber.

Printed circuit board

The PCB used in Chapter 4 was updated to include temperature measurement capability. A Type K thermocouple is used with an integrated conditioning and digital conversion chip (Maxim MAX6675) for recording temperature at every frequency reading. Two such circuits allow recordings of both internal dose chamber temperature and ambient room temperature. The temperature coefficient of frequency for FBAR devices requires careful temperature control, and post-correction due to temperature drift may be applied.

5.4.3 Experimental results

The experiments described in this section were performed on a post-fabricated FBAR-CMOS array. The eight working oscillators had a nominal frequency of 1.44 GHz, and two of the array sensors were coated with a thin PDMS sensing layer using the micropipette ap-

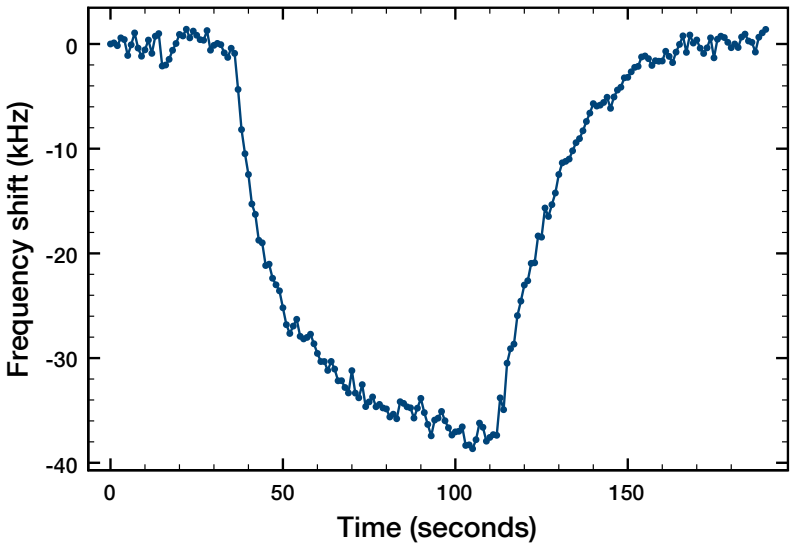

Figure 5.12: Transient response of PDMS-coated FBAR-CMOS sensor to 5200 ppm toluene vapor, as measured with an on-chip frequency counter. Sample injection occurs at 40 seconds, and nitrogen purge occurs at 110 seconds.

plication method. For vapor concentration experiments, reagent-grade toluene and n-octane (Sigma Aldrich) were used, and high purity nitrogen was employed as the carrier and purge gas.

Transient sensor response

A typical sensor response is shown in Figure 5.12, which plots the transient frequency shift of a PDMS-coated sensor after an injection of 5200 ppm toluene into the dose chamber. This measurement comprises frequency recordings at approximately one-second intervals; these were taken with the on-chip digital frequency counter located beneath the sensor. For the concentration shown, the sensor response begins to stabilize after 60 seconds, and recovery occurs on a comparable timescale. During nitrogen purge, the sensor frequency returns to baseline, which demonstrates the reversibility of toluene absorption into the PDMS film. Over a longer period of time, significant drift in the sensor baseline is observed, on the same order of magnitude as the frequency induced by vapor exposure. This behavior will be discussed in detail in Section 5.5.

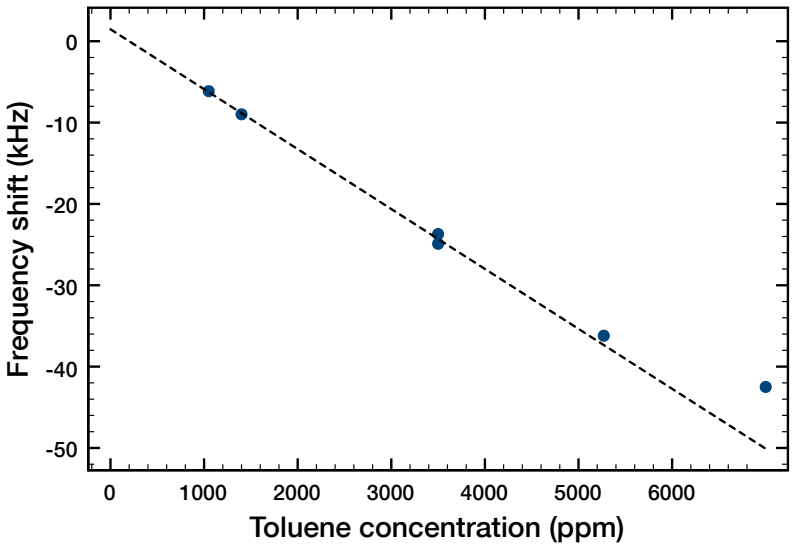

Figure 5.13: Toluene concentration series on integrated 1.44 GHz FBAR-CMOS oscillator coated with 8 nm PDMS sensing layer. This shows sensitivity in the linear region of -7.29 Hz/ppm and a non-linear saturation behavior above 5000 ppm.

Toluene concentration series and nonlinear response

A more extended toluene concentration series is shown in Figure 5.13. The experiments were conducted on a single PDMS-coated sensor, and frequency shifts were extracted from multiple single-dose runs. The process flow for each vapor measurement was identical to that developed for the QCM experiments.

The frequency sensitivity in the linear region is -7.29 Hz/ppm, and a saturation behavior is observed for concentrations above 5000 ppm. This is approximately the same concentration at which the behavior was measured with a QCM in Section 5.3. A more detailed discussion on vapor sensitivity for such devices will be found in Section 5.6.

Comparison of toluene and octane on PDMS

The frequency sensitivity of a polymer-based sensor should depend on the vapor species, as discussed in Section 5.1.4. Concentration experiments were performed for both toluene and octane using a PDMS-coated sensor to quantify this difference. For toluene, the con-

centration series covered a range from 500 ppm to 3000 ppm, and for octane the range was 750 ppm to 4600 ppm; in both cases this represents a solvent injection range of 10 μL to 60 μL. The transient data and extracted frequency shifts are shown in Figure 5.14.

The transient plots shown in Figures 5.14(a) and 5.14(b) are typical for processed data taken during a concentration series. Data processing will be discussed in Section 5.5. The extracted concentration trend in Figure 5.14(c) is linear for both octane and toluene, with a linear fit in both cases exceeding $R^2 = 0.99$. For octane the measured sensitivity is -5.80 Hz/ppm, and for toluene the measured sensitivity is -3.14 Hz/ppm. This frequency sensitivity value for toluene is much less than that shown in Figure 5.13, which stems from a thinner polymer coating.

Comparison of PDMS and PIB for vapor sensitivity

Two different integrated FBAR structures on a post-processed substrate were functionalized to demonstrate its use as a multiplex sensor array. One sensor was spotted with PDMS, and a second sensor was spotted with PIB. The frequency shifts and thicknesses of these applications are summarized in Table 5.6. The PIB coating is nearly twice the thickness of the PDMS coating.

An octane concentration experiment was completed on the functionalized array. The oscillation frequencies of PIB, PDMS, and bare sensors were measured in parallel and recorded at approximately one second intervals. The transient response for these devices to an injection of 100 μL (5000 ppm) octane is plotted in Figure 5.15. The PDMS-coated sensor has a measured sensitivity of -16.5 Hz/ppm, and the baseline drift in the PIB-coated

Table 5.6: A summary of a polymer micropipette application on integrated FBAR devices.

Polymer	**Diluent**	**Ratio**	Δf	**Thickness**
PDMS	Hexane	1:500	-4.25 MHz	16.9 nm
PIB	Toluene	1:480	-8.08 MHz	34.9 nm
None	-	-	-272 kHz	Control

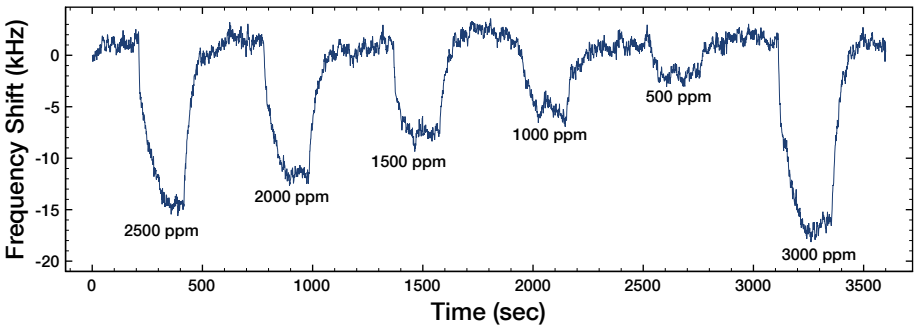

(a)

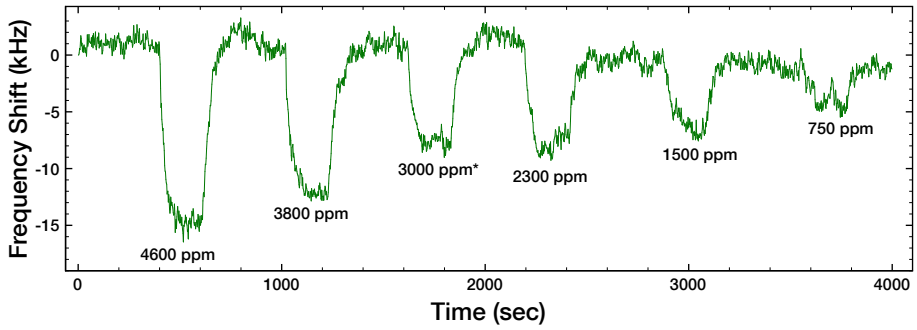

(b)

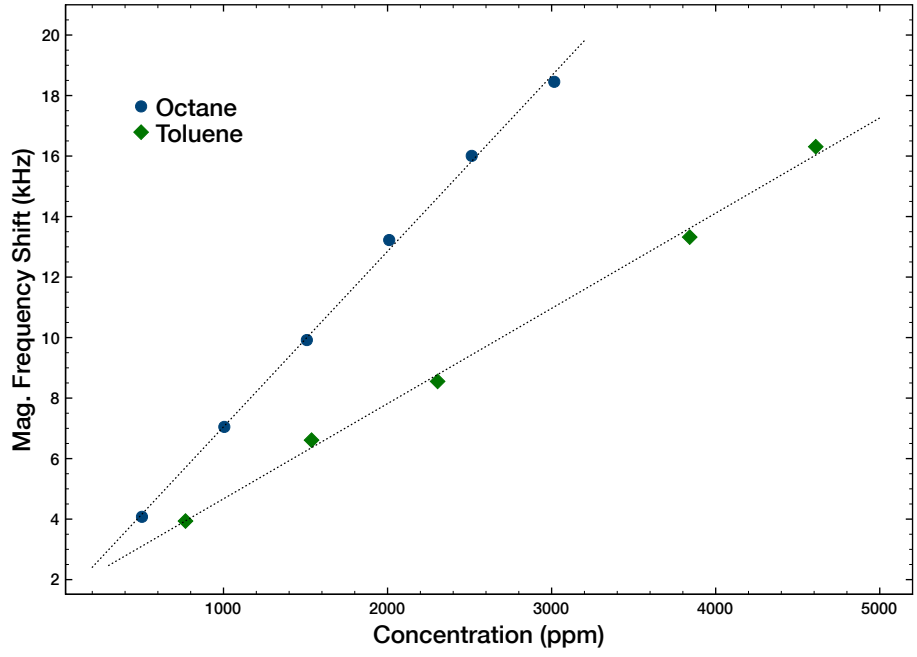

(c)

Figure 5.14: Measured transient data are shown in (a) and (b) for the response of a PDMS-coated integrated FBAR sensor to concentrations of octane and toluene, respectively. The extracted frequency shifts are shown in (c). For the measured device, the octane sensitivity is -5.80 Hz/ppm, and the toluene sensitivity is -3.14 Hz/ppm.

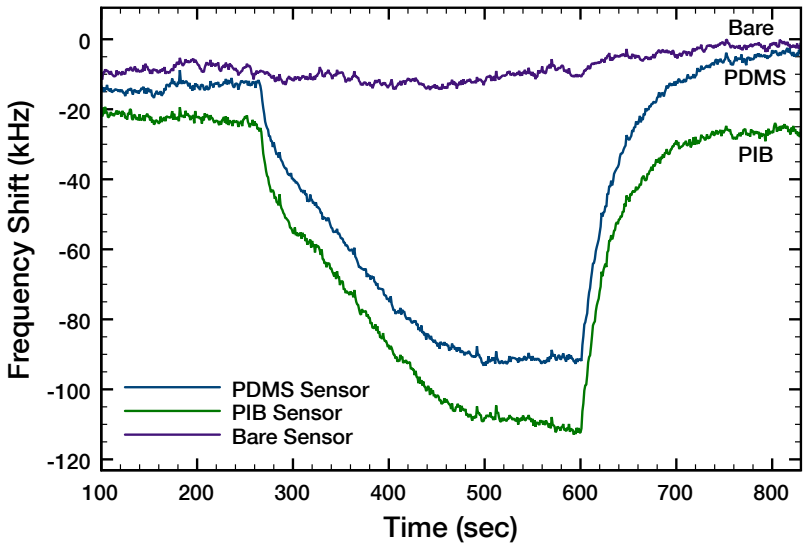

Figure 5.15: Three on-chip FBAR-CMOS oscillators are measured in parallel for their response to an injection of octane. One sensor is coated with PDMS, one with PIB, and one is bare. Octane is injected at 260 seconds, and nitrogen purge begins at 600 seconds.

sensor was too large to accurately extract a sensitivity. From Figure 5.15, it's clear that both PIB and PDMS sensors have a very similar sensitivity. Given the the larger thickness of the PIB layer, this requires a lower partition coefficient for octane-PIB than for octane-PDMS. Using the frequency shifts measured by the transient measurement in Figure 5.15, these partition coefficients can be calculated from (5.7) and (5.15). The octane-PDMS pair has a partition coefficient $\log(K) = 2.88$, and the octane-PIB pair has a partition coefficient of $\log(K) = 2.58$.

5.5 Array-based drift correction in FBAR-CMOS sensors

The frequency sensitivity of FBAR devices to temperature was discussed in Chapter 4, where the temperature coefficient of frequency (TCF) for high-frequency acoustic wave devices is shown to be an order of magnitude worse than is commonly reported for quartz crystals. A large body of work has addressed this issue, including temperature compensation of the device structure and acoustic reflector [146, 148, 149, 168], algorithmic correction of

the known TCF [169], and the use of a dummy delay-line in SAW devices [170]. Even with compensation, tight temperature control to better than ±1 °C is typically required for QCM-competetive measurement resolution in BAW and SAW sensing applications. For FBAR-based measurements, a dense sensor array offers an alternative compensation strategy, in which bare devices are measured alongside functionalized devices, and the differential shift is used as the measurement signal. This mitigates ambient common-mode sources of drift, including changes in temperature and humidity.

An example of this method applied to measured data is shown in Figure 5.16, where two functionalized sensors were compared against a third, bare reference oscillator. All of these devices were on the same CMOS die, were measured in parallel with on-chip counters, and experienced the same ambient chamber environment. In this experiment, an octane concentration series was run, which covered a concentration range from 500 ppm to 5000 ppm. Measurement frequencies have been normalized for each device by subtraction of the nominal frequency, but otherwise plotted data are unfiltered. For the PDMS-coated device in Figure 5.16(a), the coated and bare sensors track very closely. Localized shifts in the bare sensor are attributed to temperature-based shifts corresponding to alternately purging and sealing the dose chamber. The difference between these signals is plotted in Figure 5.16(b), where the baseline drift has been almost entirely removed from the corrected signal. If the overall drift in Figure 5.16(a) is attributed to temperature, the corrected baseline in Figure 5.16(b) represents a compensation yielding a TCF improvement from -38 ppm/°C to -6 ppm/°C.

This correction relies on having one or more bare array devices that track the movement of the functionalized sensor. For the PIB-coated device in Figure 5.16(c), the bare sensor does not track the overall baseline drift, and the corrected signal in Figure 5.16(d) is not useable for quantitative data. It is likely that close tracking is a function of localized heating on the CMOS die, which may be improved through a more dense array (more pairing options) or a more homogenous design of the underlying switching circuits.

It is also possible that the drifts measured in Figure 5.16 are dominated by something

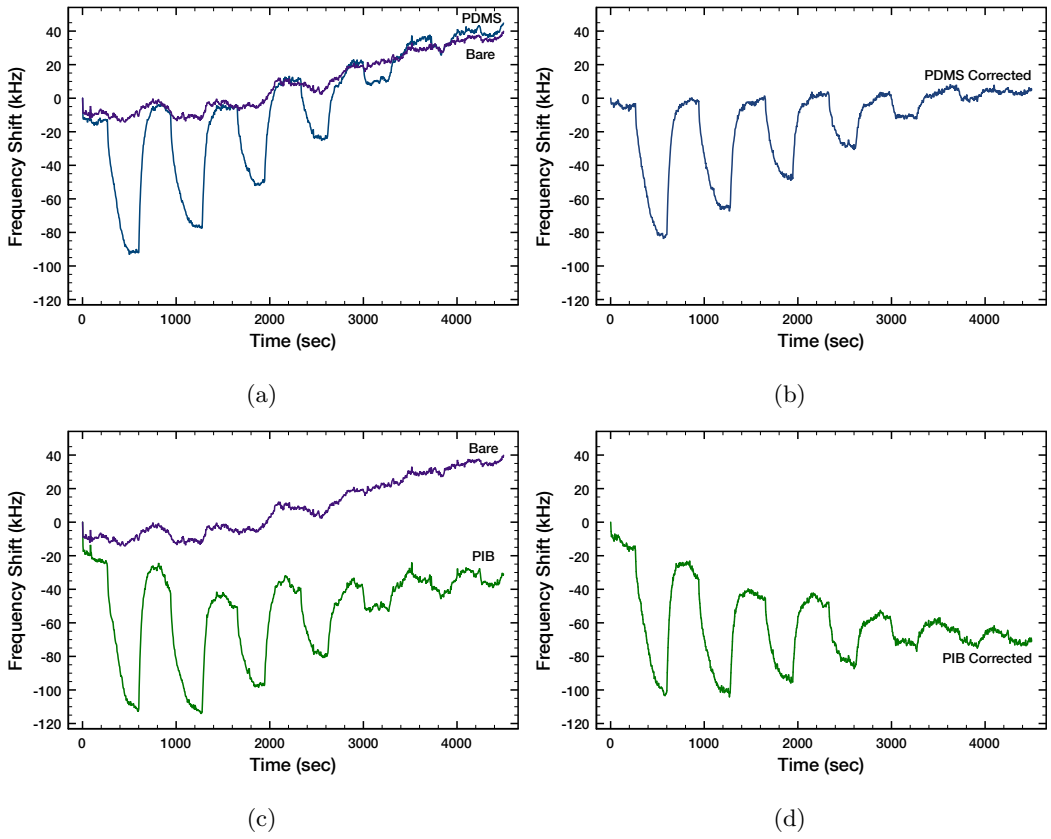

Figure 5.16: A bare FBAR device in the array is used to track baseline frequency drifts. This can be used in some cases for baseline subtraction, as seen in (b) for the correction applied to the data in (a). If a bare device does not track well, the correction method is less successful, as shown in (c) and (d).

other than temperature shifts, and significant additional qualification is needed before this correction method could be reliably applied to a quantitative measurement system. It is intended here as an illustration of the comparative advantage that an array of sensors offers over the few-sensor measurement system, in addition to multiplex detection capability.

5.6 Detection sensitivity and limits of detection

For resonant acoustic sensors, several metrics are typically employed to compare device performance within the space. These are divided into descriptions of sensitivity and resolution, and they are unified in a description of an application-specific limit of detection. This section will discuss each of these comparative metrics.

5.6.1 Frequency sensitivity to mass attachment

Despite the conclusion of Section 4.2.1 that 'gravimetric sensing' is a misleading nomenclature, the comparison of mass sensitivity remains as the only measurement metric that is application independent. Absorbed gas, accreted film deposition, and bound antigen can all be classified by a frequency sensitivity to mass attachment.

The toluene series in Figure 5.13 can be used to to quantify mass sensitivity for a PDMS-coated 1.44 GHz oscillator. For a calculated PDMS layer thickness of 8 nm for the measured sensor, the partition coefficient for PDMS-toluene is used to calculate a sensor sensitivity of 31.3 kHz/pg, which is 313 kHz$\cdot\mu$m^2/fg when normalized to sensor area. As sensitivity scales with the square of resonant frequency, these results are commensurate with other resonant VOC work, as summarized in Table 5.7.

Mass sensitivity numbers should be treated as approximate, as their calculation relies on many simplifying assumptions. For vapor sensing, this includes linearity of the Sauerbrey equation for both polymer addition and vapor absorption, accurate calculation of the partition coefficient, and accuracy of the estimated device area.

Table 5.7: Comparison of frequency sensitivity of mass addition for this work and representative published examples. Devices include thin-film bulk acoustic resonator (FBAR) and contour mode resonators (CMR). Detection methods include polymer-based VOC detection, thin-film deposition, VOC adsorption to single-stranded DNA (ssDNA), and VOC adsorption to a self-assembled monolayer (SAM).

Device	**Frequency**	Sensing	**Mass Sensitivity**	**Reference**
FBAR	1.44 GHz	VOC/Polymer	313 kHz·μm^2/fg	This work (Fig. 5.13)
FBAR	850 MHz	Thin-film	32.8 kHz·μm^2/fg	This work (Fig. 4.31)
CMR	220 MHz	VOC/ss-DNA	41.6 kHz·μm^2/fg	[53]
FBAR	8 GHz	VOC/SAM	10 MHz·μm^2/fg	[171]

5.6.2 Allan deviation

The performance of an acoustic resonator sensor will depend on the resolution with which the resonant frequency can be measured. For an FBAR-based oscillator, this resolution can be characterized by the Allan variance, which is commonly employed to quantify the frequency stability of clock reference oscillators [172]. This method is effectively a time-domain characterization of the oscillator phase noise that can be applied to a set of discrete frequency measurements. The Allan variance is calculated as a normalized average of the frequency shift between adjacent frequency measurements. This is described as

$$\sigma_y^2 = \frac{1}{2M}\sum_{i=1}^{M}(\Delta y_i)^2 \tag{5.20}$$

where Δy_i is the normalized fractional frequency difference $\Delta y_i = (f_{i+1} - f_i)/f_\circ$ and M is the total number of difference samples [173]. The measurement is normalized to make the measured variance independent of nominal oscillation frequency, just at ppm is used for the TCF metric. Additionally, the Allan variance can be measured for different sampling rates or at different spacings in a discrete time series. This is described by the substitution $\Delta y_i = (f_{i+\tau} - f_i)/f_\circ$ and the designation $\sigma_y^2(\tau)$, where τ is the time between adjacent measurements. In most cases, there will be an optimal τ that minimizes the variance [173]. The Allan deviation σ_y, which is simply the square root of (5.20), is used to calculate the minimum frequency resolution that can be measured from an oscillator as

$$\Delta f_{\min} = \sigma_y \cdot f_\circ \tag{5.21}$$

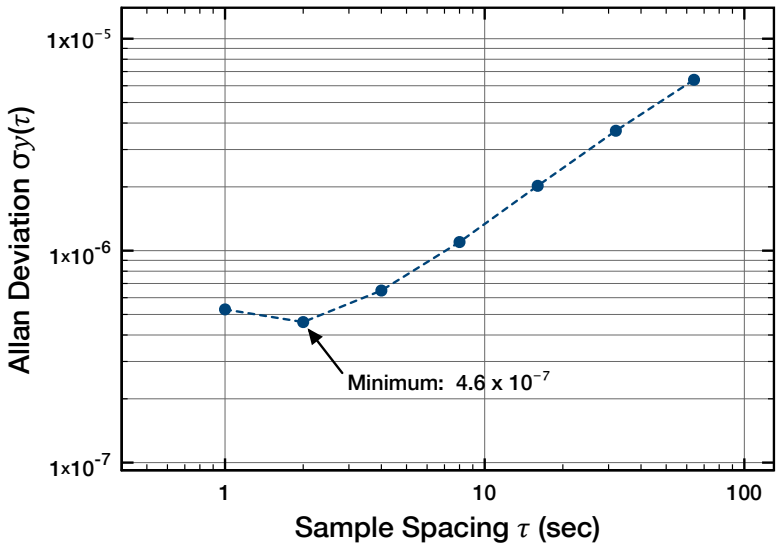

Figure 5.17: The Allan variance is calculated for increasing values of τ on a set of 4500 frequency measurements. A PDMS-coated device was used for this characterization, and a minimum deviation of $\sigma_y = 4.6 \times 10^{-7}$ is calculated.

where $f_\circ$ is the nominal oscillation frequency of the measured oscillator.

A typical Allan deviation calculation is shown in Figure 5.17 for 4500 frequency measurements taken on a PDMS-coated 1.44 GHz FBAR-CMOS oscillator at approximately 1 Hz sampling rate. This relationship shows a minimum deviation of $\sigma_{y\ \mathrm{min}} = 4.6 \times 10^{-7}$ at a sample spacing of two seconds. The increasing deviation with increasing time is attributed to the influence of frequency drift. As the spacing between samples gets further apart in time, the variance captures a longer integration of this slow drift. The average Allan deviation for measured runs is $3.13{\times}10^{-7}$ with a standard deviation of $9.2{\times}10^{-8}$, which corresponds to a minimum frequency resolution calculated from (5.21) as $\Delta f_{\mathrm{min}} = 450 \pm 130$ Hz for the PDMS-coated FBAR sensor. This is significantly higher than a the minimum resolution of 0.1-3 Hz reported for a typical QCM [12, 174], but it is commensurate with reported values for gigahertz acoustic wave sensors [33].

In some cases, however, high-frequency acoustic wave devices have been demonstrated to have much better resolution. For example, Rinaldi *et al.* report a frequency-equivalent Allan deviation as low as $f_{\mathrm{min}} = 0.9$ Hz for a 186 MHz contour mode res-

onator [175]. These off-chip devices have a high quality factor (Q≈1000), and the minimum demonstrated resolvable frequency shift is 300 Hz.

5.6.3 Limit of detection for vapor sensing array

The frequency sensitivity S_f and minimum frequency resolution $\Delta f_{\min}$ are used to calculate the limit of detection (LOD) for a sensor system. This is described as

$$\text{LOD} = \frac{\Delta f_{\min}}{S_f} \tag{5.22}$$

where S_f can refer to an application-specific frequency sensitivity or the equivalent extracted mass sensitivity [33]. For the 1.44 GHz integrated FBAR sensors characterized in this section, a mass sensitivity of $S_f = 313$ kHz·μm^2/fg and frequency resolution of $\Delta f_{\min} = 450$ Hz yields an average mass-based detection limit of LOD=1.44 ag/um^2. For the best measured Allan deviation of σ_y=1.43×10^{-7}, this corresponds to a detection limit of 658 zg/um^2.

For a specific application, the detection limit is more directly characterized by the frequency sensitivity in response to a particular analyte. For the toluene concentration series in Figure 5.13, the frequency sensitivity in the linear range was reported as $S_f = -7.29$ Hz/ppm. For an average frequency resolution $\Delta f_{\min} = 450$ Hz, this corresponds to detection limit of LOD = 62 ppm for toluene. For a given frequency resolution, this detection limit will be a function of the polymer layer thickness and the solvent-polymer partition coefficient. (In practice, these cannot be entirely decoupled, as a thicker polymer layer degrades FBAR quality factor and increases measured Allan deviation.) For the octane sensitivity demonstrated by the PDMS-coated device in Section 5.4.3 of $S_f = -16.5$ Hz/ppm, the calculated detection limit is 27 ppm octane.

Calculated theoretical detection limits will in practice be limited by noise sources not captured by the Allan variance. These include environment variables of temperature and humidity, noise inherent to the attachment mechanisms, and fluctuations in reference frequency, supply voltages, and quantization. For a real measurement setup, a detection limit must be characterized by demonstrable, resolvable frequency shifts that are repeatable

and distinguishable from noise and drift. For the sensors characterized in this section, the minimum demonstrated resolved concentration was 250 ppm octane.

5.7 Handheld prototype unit

The integration of FBAR resonators with CMOS oscillators and frequency counters removes the need for external measurement equipment, which has historically been a significant drawback of high-frequency resonant sensors. This was demonstrated by the design and implementation of a handheld measurement system, which is shown in Figure 5.18. This device measures less than 7" in its longest dimension and is powered from the on-board USB port. The entire array of FBAR-CMOS oscillators can be driven and measured in parallel, and recorded alongside ambient temperature, without any additional hardware. The pictured printed circuit board was used for all measurements reported in this chapter.

(a) (b)

Figure 5.18: A handheld prototype was built to illustrate the system portability enabled by the integration of FBAR sensors directly with a CMOS substrate. This unit is less than 7" long and can be powered from a USB port. No additional hardware is required to operate the complete sensor array.

5.8 Chapter Summary

This chapter has demonstrated the successful integration of the FBAR devices from Chapter 3 and the CMOS substrate from Chapter 4 for application to sensing of volatile organic compounds. Both single and parallel frequency measurement of on-chip FBAR-CMOS oscillators were characterized, and multiple polymers and multiple vapor species have been tested. The highest observed frequency sensitivity to vapor concentration was -16.5 Hz/ppm for octane absorption into a PDMS sensing layer, and the average minimum frequency resolution of experimental measurements is 450 Hz. The limit of detection calculated for the best measured Allan deviation corresponds to a mass limit of 658 zg/um^2.

The frequency sensitivity, frequency resolution, and limit of detection for 1.44 GHz FBAR-CMOS sensors have been demonstrated in this section to be comparable to published measurements. The characterized sensors are not yet best in class. This is limited inherently by the additional challenges of building high-Q resonant structures monolithically on a CMOS substrate, and by the thermal fluctuations introduced by the underlying circuitry. Future work may narrow these performance gaps, with improved device fabrication and improved circuit compensation techniques. However, the application advantages gained by the ability to integrate a dense array of sensors directly with measurement electronics may prove to be well worth the performance tradeoffs over the individual acoustic sensor.

Chapter 6

Conclusions

6.1 Summary of contributions

This dissertation describes a body of work conducted to integrate an array of real-time, label-free sensors with an active CMOS substrate. The goal was to overcome the measurement complexity and equipment cost normally required for detection with acoustic resonators, and to enable their use in a dense array. A custom CMOS substrate was designed and fabricated to support oscillation and frequency measurement for each of 24 on-chip sensor sites. The fabrication of FBAR devices has been validated for both off-chip and monolithic on-chip devices. The integrated sensor system was characterized for sensitivity and limit of detection. The sensing performance is limited by the frequency sensitivity to temperature, which is an inherent challenge in all piezoelectric resonator applications. A method has been proposed which leverages the array format for compensation of this effect. On-chip parallel measurement of multiple sensors in real time was demonstrated for a quantitative vapor sensing application.

This work has made several original contributions to the development of acoustic resonators, CMOS-integrated electronics, and portable sensor systems:

- The first monolithically integrated FBAR devices on CMOS with demonstrated mass sensitivity. The integrated system is demonstrated experimentally through the addi-

tion of successive thin-film oxide depositions.

- A method for the fabrication of solidly-mounted FBAR structures monolithically on a fabricated CMOS chip. This includes device structures for quarter- and half-wavelength resonators and the development of two- and three-layer photoresist processes for smooth lift-off patterning of 1-3 μm films on a diced CMOS chip.

- A method for the application of thin polymer films to individual sites in a dense sensor array. This method was used to functionalize integrated FBAR sensors with PDMS and PIB for semi-selective vapor absorption.

- The first demonstration of monolithic FBAR devices on CMOS for organic vapor detection and quantification. Vapor absorption into a thin polymer layer was measured in real time and at multiple sites within the sensor array.

- A method for temperature and drift correction in an array of resonant sensors. By functionalizing some sensors and leaving other sensors bare, the difference in their frequency shifts can provide measurement signal that is less sensitive to frequency drift than the individual sensors.

These contributions have resulted in the following peer-reviewed publications:

- M. L. Johnston, I. Kymissis, and K. L. Shepard, "FBAR-CMOS Oscillator Array for Mass-Sensing Applications," *Sensors Journal, IEEE*, vol. 10 (6), pp. 1042-1047, 2010.

- M. L. Johnston, H. Edrees, I. Kymissis, and K. L. Shepard,"Integrated VOC Vapor Sensing on FBAR-CMOS Array," *The 25th International Conference on Micro Electro Mechanical Systems (IEEE MEMS 2012)*, January 2012.

- M. L. Johnston, I. Kymissis, and K. L. Shepard,"An array of monolithic FBAR-CMOS oscillators for mass-Sensing applications," *Proc. of 15th International Conference on Solid-State Sensors, Actuators & Microsystems (Transducers '09)*, June 2009.

6.2 Future work

This work can be improved and extended in many ways and many directions. For improved performance and broadened application space, the following categories of design and development may prove useful:

Aqueous operation

Application to medical and biological applications requires, with few exceptions, sensors that operate in liquid. For FBAR devices, this can be accomplished through the fabrication of shear mode resonators; a body of work toward this end exists and is evolving [24,92,176]. Adapting such methods to integrated CMOS resonators will enable sensing in a liquid environmental without a significant reduction in detection resolution, enabling label-free quantification of proteins and nucleic acids. As a related aim, packaging techniques must be devised for fluidic sample delivery.

Temperature compensation

The frequency sensitivity to temperature for FBAR devices continues to limit their performance. A variety of structural and circuit-based compensation techniques have been proposed that will mitigate this effect [149, 177]. Additionally, many of the temperature compensation techniques historically applied to quartz crystal oscillators might be adapted for use in FBAR-based sensor systems.

Oscillator design

The design of low phase noise oscillators is an expertise all its own, and significant improvement in oscillator performance can likely be brought to bare through an improved design of the FBAR-based integrated oscillator. The current implementation was built around modeled devices, whereas future oscillators can be designed in conjunction with measured device data.

Resonator quality factor

The theoretically attainable mass resolution is inversely proportional to the resonator quality factor Q. Planarization of the CMOS substrate prior to monolithic fabrication and other fabrication improvements will directly improve resonator Q and system-level detection performance.

Array density

The substrate presented here supports an array of 24 integrated sensors, but a much denser array could be implemented with similar circuitry and similar structures. There is a lot of open space. Further scaling will result from reduction of FBAR size, which is limited only as spurious plate modes start to degrade performance or as the dedicated circuitry can no longer fit beneath.

6.3 Final thoughts

The FBAR-CMOS sensor platform I have presented here has demonstrated viability for real sensing applications. Improving the performance and broadening the scope of addressable applications may be achieved by the avenues described above or by as-yet unidentified methods. I hope that this will enable real-world applications of the presented technology, and that those applications will be useful and helpful to people.

Bibliography

[1] G. E. Moore, "Cramming more components onto integrated circuits, Reprinted from Electronics, volume 38, number 8, April 19, 1965, pp.114 ff." *IEEE Solid-State Circuits Newsletter*, vol. 20, no. 3, pp. 33–35, 2006.

[2] J. M. Rothberg *et al.*, "An integrated semiconductor device enabling non-optical genome sequencing," *Nature*, vol. 475, no. 7356, pp. 348–352, Jul. 2011.

[3] G. A. Posthuma-Trumpie, J. Korf, and A. Amerongen, "Lateral flow (immuno)assay: its strengths, weaknesses, opportunities and threats. A literature survey," *Analytical and Bioanalytical Chemistry*, vol. 393, no. 2, pp. 569–582, Aug. 2008.

[4] G. Shan, *Immunoassays in Agricultural Biotechnology.* John Wiley and Sons, Inc., 2011.

[5] S. K. Brown, M. R. Sim, M. J. Abramson, and C. N. Gray, "Concentrations of Volatile Organic Compounds in Indoor Air - A Review," *Indoor Air*, vol. 4, no. 2, pp. 123–134, Jun. 1994.

[6] OSHA. OSHA Technical Manual (OTM) - Section II: Chapter 1 - Personal Sampling for Air Contaminants. [Online]. Available: http://www.osha.gov/dts/osta/otm/otm_ii/otm_ii_1.html

[7] J. Lodge, *Methods of air sampling and analysis* , 3rd ed., J. Lodge, Ed. CRC Press LLC, 1988.

[8] "Gas Sniper Portable Gas Detector," Matheson Trigas.

[9] G. Sauerbrey, "Verwendung von Schwingquarzen zur Wägung dünner Schichten und zur Mikrowägung," *Zeitschrift für Physik A Hadrons and Nuclei*, 1959.

[10] M. E. Brown and P. K. Gallagher, *Handbook of Thermal Analysis and Calorimetry*, ser. Recent Advances, Techniques and Applications. Elsevier Science, Dec. 2007.

[11] W. H. King, "Piezoelectric Sorption Detector." *Analytical Chemistry*, vol. 36, no. 9, pp. 1735–1739, Aug. 1964.

[12] S.-H. Lee, D. D. Stubbs, J. Cairney, and W. D. Hunt, "Rapid detection of bacterial spores using a quartz crystal microbalance (QCM) immunoassay," *IEEE Sensors Journal*, vol. 5, no. 4, pp. 737–743.

[13] T. Hunter and G. Price, "Selective piezoelectric sensors using polymer reagents," *Analyst*, vol. 120, Jan. 1995.

[14] M. Muratsugu, F. Ohta, Y. Miya, T. Hosokawa, S. Kurosawa, N. Kamo, and H. Ikeda, "Quartz crystal microbalance for the detection of microgram quantities of human serum albumin: relationship between the frequency change and the mass of protein adsorbed," *Analytical Chemistry*, vol. 65, no. 20, pp. 2933–2937, 1993.

[15] M. Janghorbani and H. Freund, "Application of a piezoelectric quartz crystal as a partition detector. Development of a digital sensor," *Analytical Chemistry*, vol. 45, no. 2, pp. 325–332, Feb. 1973.

[16] E. Benes, "Improved quartz crystal microbalance technique," *Journal of Applied Physics*, vol. 56, no. 3, p. 608, 1984.

[17] S. D. Carrigan, G. Scott, and M. Tabrizian, "Real-Time QCM-D Immunoassay through Oriented Antibody Immobilization Using Cross-Linked Hydrogel Biointerfaces," *Langmuir*, vol. 21, no. 13, pp. 5966–5973, Jun. 2005.

[18] S. Arshad, M. Salleh, and M. Yahaya, "Performance of Quartz Crystal Microbalance Gas Sensors Using Thin Films of Titanium Dioxide, Porphyrin and Titanium Dioxide Coated with Dye Porphyrin," *Sains Malaysiana*, vol. 37, no. 3, pp. 271–275, 2008.

[19] E. Milyutin and P. Muralt, "Thin Film Bulk Acoustic Wave Resonators for Gravimetric Sensing," *Nanosystems Design and Technology*, pp. 103–116, 2009.

[20] N. Kim, D.-K. Kim, and Y.-J. Cho, "Development of indirect-competitive quartz crystal microbalance immunosensor for C-reactive protein," *Sensors & Actuators: B. Chemical*, vol. 143, no. 1, pp. 444–448, Dec. 2009.

[21] Z. Pei, X. Ma, P. Ding, W. Zhang, Z. Luo, and G. Li, "Study of a QCM Dimethyl Methylphosphonate Sensor Based on a ZnO-Modified Nanowire-Structured Manganese Dioxide Film," *Sensors*, vol. 10, no. 9, pp. 8275–8290, Sep. 2010.

[22] R. Gabl, H. Feucht, H. Zeininger, G. Eckstein, M. Schreiter, R. Primig, D. Pitzer, and W. Wersing, "First results on label-free detection of DNA and protein molecules using a novel integrated sensor technology based on gravimetric detection principles," *Biosensors and Bioelectronics*, vol. 19, no. 6, pp. 615–620, 2004.

[23] R. Gabl, E. Green, M. Schreiter, H. Feucht, H. Zeininger, R. Primig, D. Pitzer, G. Eckstein, and W. Wersing, "Novel integrated FBAR sensors: a universal technology platform for bio-and gas-detection," *Sensors, 2003. Proceedings of IEEE*, vol. 2, pp. 1184–1188 Vol. 2, 2003.

[24] J. Weber, W. Albers, J. Tuppurainen, M. Link, R. Gabl, W. Wersing, and M. Schreiter, "Shear mode FBARs as highly sensitive liquid biosensors," *Sensors & Actuators: A. Physical*, vol. 128, no. 1, pp. 84–88, 2006.

[25] M. Nirschl, A. Blüher, C. Erler, B. Katzschner, I. Vikholm-Lundin, S. Auer, J. Vörös, W. Pompe, M. Schreiter, and M. Mertig, "Film bulk acoustic resonators for DNA and protein detection and investigation of in vitro bacterial S-layer formation," *Sensors & Actuators: A. Physical*, vol. 156, no. 1, pp. 180–184, Nov. 2009.

[26] M. Link, J. Weber, M. Schreiter, W. Wersing, O. Elmazria, and P. Alnot, "Sensing characteristics of high-frequency shear mode resonators in glycerol solutions," *Sensors & Actuators: B. Chemical*, vol. 121, no. 2, pp. 372–378, 2007.

[27] W. Reichl, J. Runck, M. Schreiter, E. Greert, and R. Gabl, "Novel gas sensors based on thin film bulk acoustic resonators," *Sensors, 2004. Proceedings of IEEE*, pp. 1504–1505 vol. 3, 2004.

[28] M. Nirschl, A. Rantala, K. Tukkiniemi, S. Auer, A. Hellgren, D. Pitzer, M. Schreiter, and I. Vikholm-Lundin, "CMOS-integrated film bulk acoustic resonators for label-free biosensing," *Sensors*, vol. 10, no. 5, pp. 4180–4193, 2010.

[29] S. Auer, M. Nirschl, M. Schreiter, and I. Vikholm-Lundin, "Detection of DNA hybridisation in a diluted serum matrix by surface plasmon resonance and film bulk acoustic resonators." *Analytical and Bioanalytical Chemistry*, vol. 400, no. 5, pp. 1387–1396, May 2011.

[30] H. Zhang and E. S. Kim, "Micromachined acoustic resonant mass sensor," *Journal of Microelectromechanical Systems*, vol. 14, no. 4, pp. 699–706, Aug. 2005.

[31] H. Zhang, W. Pang, M. S. Marma, C.-Y. Lee, S. Kamal-Bahl, E. S. Kim, and C. E. McKenna, "Label-free detection of protein-ligand interactions in real time using micromachined bulk acoustic resonators," *Applied Physics Letters*, vol. 96, no. 12, pp. 123 702–123 702, 2010.

[32] W. Xu, X. Zhang, S. Choi, and J. Chae, "A High-Quality-Factor Film Bulk Acoustic Resonator in Liquid for Biosensing Applications," *Journal of Microelectromechanical Systems*, vol. 20, no. 1, pp. 213–220.

[33] S. Fanget, S. Hentz, P. Puget, and J. Arcamone, "Gas sensors based on gravimetric detection-A Review," *Sensors and Actuators B ...*, vol. 160, pp. 804–821, 2011.

[34] H. Campanella, *Acoustic wave and electromechanical resonators.* Artech House Publishers, Feb. 2010.

[35] W. Buff, "SAW sensors," *Sensors & Actuators: A. Physical*, vol. 30, no. 1-2, pp. 117–121, Jan. 1992.

[36] E. J. Staples, J. S. Schoenwald, R. C. Rosenfeld, and C. S. Hartmann, "1974 Ultrasonics Symposium," in *1974 Ultrasonics Symposium.* IEEE, 1974, pp. 245–252.

[37] R. M. White and F. W. Voltmer, "Direct piezoelectric coupling to surface elastic waves," *Applied Physics Letters*, vol. 7, no. 12, p. 314, 1965.

[38] T. M. Reeder, D. E. Cullen, and M. Gilden, "1975 Ultrasonics Symposium," in *1975 Ultrasonics Symposium.* IEEE, 1975, pp. 264–268.

[39] X. Bao, W. Burkhard, V. Varadan, and V. Varadan, "SAW Temperature Sensor and Remote Reading System," *IEEE 1987 Ultrasonics Symposium*, pp. 583–586, 1987.

[40] A. Pohl, G. Ostermayer, L. Reindl, and F. Seifert, "1997 IEEE Ultrasonics Symposium Proceedings. An International Symposium (Cat. No.97CH36118)," in *1997 IEEE Ultrasonics Symposium An International Symposium.* IEEE, 1997, pp. 471–474.

[41] C. T. Chuang, R. M. White, and J. J. Bernstein, "A thin-membrane surface-acoustic-wave vapor-sensing device," *IEEE Electron Device Letters*, vol. 3, no. 6, pp. 145–148, Jun. 1982.

[42] M. Rapp, J. Reibel, A. Voigt, M. Balzer, and O. Bülow, "New miniaturized SAW-sensor array for organic gas detection driven by multiplexed oscillators," *Sensors & Actuators: B. Chemical*, vol. 65, no. 1-3, pp. 169–172, Jun. 2000.

[43] J. Reibel, U. Stahl, T. Wessa, and M. Rapp, "Gas analysis with SAW sensor systems," *Sensors & Actuators: B. Chemical*, vol. 65, no. 1-3, pp. 173–175, Jun. 2000.

[44] K. Länge, G. Blaess, A. Voigt, R. Götzen, and M. Rapp, "Integration of a surface acoustic wave biosensor in a microfluidic polymer chip," *Biosensors and Bioelectronics*, vol. 22, no. 2, pp. 227–232, Aug. 2006.

[45] K. Länge, S. Grimm, and M. Rapp, "Chemical modification of parylene C coatings for SAW biosensors," *Sensors & Actuators: B. Chemical*, vol. 125, no. 2, pp. 441–446, Aug. 2007.

[46] D. Powell, K. Kalantar-zadeh, S. Ippolito, and W. Wlodarski, "A layered SAW device based on ZnO/LiTaO3 for liquid media sensing applications," in *Ultrasonics Symposium, 2002. Proceedings. 2002 IEEE*, 2002, pp. 493–496.

[47] K. Kalantar-Zadeh, W. Wlodarski, Y. Y. Chen, B. N. Fry, and K. Galatsis, "Novel Love mode surface acoustic wave based immunosensors," *Sensors & Actuators: B. Chemical*, vol. 91, no. 1-3, pp. 143–147, Jun. 2003.

[48] Y. Hur, J. Han, J. Seon, and Y. Pak, "Development of an SH-SAW sensor for the detection of DNA hybridization," *Sensors & Actuators: A. Physical*, 2005.

[49] R. Lanz and P. Muralt, "Solidly mounted BAW filters for 8 GHz based on AlN thin films," *Ultrasonics, 2003 IEEE Symposium on*, vol. 1, pp. 178–181 Vol.1, 2003.

[50] M. Aissi, E. Tournier, M. Dubois, C. Billard, H. Ziad, and R. Plana, "A 5 GHz above-IC FBAR low phase noise balanced oscillator," *Radio Frequency Integrated Circuits (RFIC) Symposium, 2006 IEEE*, p. 4, 2006.

[51] G. Piazza and A. Pisano, "Two-port stacked piezoelectric aluminum nitride contour-mode resonant MEMS," *Sensors & Actuators: A. Physical*, vol. 136, no. 2, pp. 638–645, 2007.

[52] M. Rinaldi, C. Zuniga, N. Sinha, M. Taheri, G. Piazza, S. Khamis, and A. Johnson, "Gravimetric chemical sensor based on the direct integration of SWNTS on ALN Contour-Mode MEMS resonators," *Frequency Control Symposium, 2008 IEEE International*, pp. 443–448, 2008.

[53] M. Rinaldi, B. Duick, C. Zuniga, C. Zuo, and G. Piazza, "SS-DNA functionalized ultra-thin-film ALN Contour-mode Resonators with self-sustained oscillator for volatile organic chemical detection," in *Micro Electro Mechanical Systems (MEMS), 2010 IEEE 23rd International Conference on*, 2010, pp. 132–135.

[54] M. Rinaldi, C. Zuniga, C. Zuo, and G. Piazza, "Super-high-frequency two-port AlN contour-mode resonators for RF applications," *Ultrasonics, Ferroelectrics and Frequency Control, IEEE Transactions on*, vol. 57, no. 1, pp. 38–45, 2010.

[55] M. Li, H. X. Tang, and M. L. Roukes, "Ultra-sensitive NEMS-based cantilevers for sensing, scanned probe and very high-frequency applications," *Nature Publishing Group*, vol. 2, no. 2, pp. 114–120, Jan. 2007.

[56] K. S. Hwang, J. H. Lee, J. Park, D. S. Yoon, J. H. Park, and T. S. Kim, "In-situ quantitative analysis of a prostate-specific antigen (PSA) using a nanomechanical PZT cantilever," *Lab on a Chip*, vol. 4, no. 6, pp. 547–552, 2004.

[57] C. Hagleitner, D. Lange, A. Hierlemann, O. Brand, and H. Baltes, "CMOS single-chip gas detection system comprising capacitive, calorimetric and mass-sensitive microsensors," *IEEE Journal of Solid-State Circuits*, vol. 37, no. 12, pp. 1867–1878, Dec. 2002.

[58] F. Ricci and K. W. Plaxco, "E-DNA sensors for convenient, label-free electrochemical detection of hybridization," *Microchimica Acta*, vol. 163, no. 3-4, pp. 149–155, Apr. 2008.

[59] M. Vestergaard, K. Kerman, and E. Tamiya, "An Overview of Label-free Electrochemical Protein Sensors," *Sensors*, vol. 7, no. 12, pp. 3442–3458, Dec. 2007.

[60] K. J. Odenthal and J. J. Gooding, "An introduction to electrochemical DNA biosensors," *Analyst*, vol. 132, no. 7, pp. 603–610, 2007.

[61] P. Levine, P. Gong, R. Levicky, and K. Shepard, "Real-time, multiplexed electrochemical DNA detection using an active complementary metal-oxide-semiconductor biosensor array with integrated sensor electronics," *Biosensors and Bioelectronics*, vol. 24, pp. 1995–2001, 2009.

[62] C. Nylander, B. Liedberg, and T. Lind, "Gas detection by means of surface plasmon resonance," *Sensors and Actuators*, vol. 3, pp. 79–88, 1982.

[63] M. Malmqvist, "Surface plasmon resonance for detection and measurement of antibody-antigen affinity and kinetics," *Current opinion in immunology*, vol. 5, no. 2, pp. 282–286, 1993.

[64] J. Homola, "Present and future of surface plasmon resonance biosensors," *Analytical and Bioanalytical Chemistry*, vol. 377, pp. 528–539, 2003.

[65] M. Malmqvist, "BIACORE: an affinity biosensor system for characterization of biomolecular interactions," *Biochemical society transactions*, 1999.

[66] S. Sorgenfrei, C.-y. Chiu, R. L. Gonzalez, Y.-J. Yu, P. Kim, C. Nuckolls, and K. L. Shepard, "Label-free single-molecule detection of DNA-hybridization kinetics with a carbon nanotube field-effect transistor," *Nature Publishing Group*, vol. 6, no. 2, pp. 126–132, Jan. 2011.

[67] J. L. Arlett, E. B. Myers, and M. L. Roukes, "Comparative advantages of mechanical biosensors," *Nature Publishing Group*, vol. 6, no. 4, pp. 203–215, Mar. 2011.

[68] D. Erickson, S. Mandal, A. H. J. Yang, and B. Cordovez, "Nanobiosensors: optofluidic, electrical and mechanical approaches to biomolecular detection at the nanoscale," *Microfluidics and Nanofluidics*, vol. 4, no. 1-2, pp. 33–52, Aug. 2007.

[69] J. Rickert and A. Brecht, "QCM operation in liquids: constant sensitivity during formation of extended protein multilayers by affinity," *Analytical Chemistry*, vol. 69, pp. 1441–1448, 1997.

[70] W. Wang, S. He, S. Li, and Y. Pan, "High frequency stability oscillator for surface acoustic wave-based gas sensor," *Smart Materials and Structures*, vol. 15, no. 6, pp. 1525–1530, Sep. 2006.

[71] X. Su, Y. Wu, and W. Knoll, "Comparison of surface plasmon resonance spectroscopy and quartz crystal microbalance techniques for studying DNA assembly and hybridization," *Biosensors and Bioelectronics*, vol. 21, no. 5, pp. 719–726, 2005.

[72] K. Lakin, "Thin film resonators and filters," *Ultrasonics Symposium*, 1999.

[73] B. Otis and J. Rabaey, "A 300-W 1.9-GHz CMOS oscillator utilizing micromachined resonators," *IEEE Journal of Solid-State Circuits*, vol. 38, no. 7, pp. 1271–1274, 2003.

[74] Y. Chee, A. Niknejad, and J. Rabaey, "A sub-100 /spl mu/W 1.9-GHz CMOS oscillator using FBAR resonator," *Radio Frequency integrated Circuits (RFIC) Symposium, 2005. Digest of Papers. 2005 IEEE*, pp. 123–126, May 2005.

[75] S. Rai and B. Otis, "A 1V 600W 2.1GHz Quadrature VCO Using BAW Resonators," in *Solid-State Circuits Conference, 2007. ISSCC 2007. Digest of Technical Papers. IEEE International*, 2007, pp. 576–623.

[76] J. Hu, L. Callaghan, R. Ruby, and B. Otis, "A 50ppm 600MHz frequency reference utilizing the series resonance of an FBAR," *Radio Frequency Integrated Circuits Symposium (RFIC), 2010 IEEE*, pp. 325–328, 2010.

[77] S. Dossou, N. Abele, E. Cesar, P. Ancey, J.-F. Carpentier, P. Vincent, and J.-M. Fournier, "60W SMR BAW oscillator designed in 65nm CMOS technology," *Circuits and Systems, 2008. ISCAS 2008. IEEE International Symposium on*, pp. 1456–1459, 2008.

[78] M. Åberg, M. Ylimaula, M. Ylilammi, T. Pensala, and A. Rantala, "A low noise 0.9 GHz FBAR clock," *Analog Integrated Circuits and Signal Processing*, vol. 50, no. 1, pp. 29–37, 2007.

[79] S. Rai, Y. Su, W. Pang, R. Ruby, and B. Otis, "A digitally compensated 1.5 GHz CMOS/FBAR frequency reference," *IEEE Transactions on Ultrasonics, Ferroelectrics and Frequency Control*, vol. 57, no. 3, pp. 552–561.

[80] J. Chabloz, C. Muller, F. Pengg, A. Pezous, C. Enz, and M. Dubois, "A Low-Power 2.4GHz CMOS Receiver Front-End Using BAW Resonators," *Solid-State Circuits, 2006 IEEE International Conference Digest of Technical Papers*, pp. 1244–1253, 2006.

[81] M. Rinaldi, C. Zuo, J. Van der Spiegel, and G. Piazza, "Reconfigurable CMOS Oscillator Based on Multifrequency AlN Contour-Mode MEMS Resonators," *IEEE Transactions on Electron Devices*, vol. 58, no. 5, pp. 1281–1286, 2011.

[82] M. Augustyniak *et al.*, "An Integrated Gravimetric FBAR Circuit for Operation in Liquids Using a Flip-Chip Extended 0.13m CMOS Technology," in *Solid-State Circuits Conference, 2007. ISSCC 2007. Digest of Technical Papers. IEEE International*, 2007, pp. 392–610.

[83] H. Campanella, E. Cabruja, J. Montserrat, A. Uranga, N. Barniol, and J. Esteve, "Thin-Film Bulk Acoustic Wave Resonator Floating Above CMOS Substrate," *Electron Device Letters, IEEE*, vol. 29, no. 1, pp. 28–30, 2008.

[84] M. Dubois, C. Billard, C. Muller, G. Parat, and P. Vincent, "Integration of high-Q BAW resonators and filters above IC," *Solid-State Circuits Conference, 2005. Digest of Technical Papers. ISSCC. 2005 IEEE International*, pp. 392–606 Vol. 1, Jan. 2005.

[85] B. A. Auld, *Acoustic Fields and Waves in Solids*, 2nd ed. Krieger Pub Co, Feb. 1990.

[86] T. H. Lee, "It's about Time: A Brief Chronology of Chronometry," *Solid-State Circuits Newsletter, IEEE*, vol. 13, no. 3, pp. 42–49, 2008.

[87] R. Ruby, P. Bradley, Y. Oshmyansky, A. Chien, and J. I. Larson, "Thin film bulk wave acoustic resonators (FBAR) for wireless applications," *Ultrasonics Symposium, 2001 IEEE*, vol. 1, pp. 813–821, 2001.

[88] J. Rosenbaum, *Bulk Acoustic Wave Theory and Devices.* Artech House, Inc., 1988.

[89] T. Fay and S. D. Graham, "Coupled spring equations," *International Journal of Mathematical Education in Science and Technology*, vol. 34, no. 1, pp. 65–79, Jan. 2003.

[90] K. Hashimoto, *RF Bulk acoustic wave filters for communications.* Artech House Publishers, May 2009.

[91] J. Bjurstrom, G. Wingqvist, and I. Katardjiev, "Synthesis of textured thin piezoelectric AlN films with a nonzero C-axis mean tilt for the fabrication of shear mode resonators," *IEEE Transactions on Ultrasonics, Ferroelectrics and Frequency Control*, vol. 53, no. 11, pp. 2095–2100.

[92] Morisato, N. Takayanagi, S. Yanagitani, T. Matsukawa, M. Watanabe, and Yoshiaki, "Multilayer Shear Wave Resonator Consisting of C-Axis Tilted ZnO Films," pp. 1–4, Sep. 2009.

[93] A. Dickherber, C. Corso, and W. D. Hunt, "Optimization and characterization of a ZnO biosensor array," *Sensors & Actuators: A. Physical*, vol. 144, no. 1, pp. 7–12, 2008.

[94] S. Tadigadapa and K. Mateti, "Piezoelectric MEMS sensors: state-of-the-art and perspectives," *Measurement Science and Technology*, vol. 20, no. 9, p. 092001, Jul. 2009.

[95] T. Meeker, "IEEE Standard on Piezoelectricity," *ANSI/IEEE Std 176-1987*, 1988.

[96] K. Nakamura and H. Kanbara, "Theoretical analysis of a piezoelectric thin film resonator with acoustic quarter-wave multilayers," *Frequency Control Symposium, 1998. Proceedings of the 1998 IEEE International*, pp. 876–881, Apr. 1998.

[97] T. H. Lee, *The Design of Cmos Radio-Frequency Integrated Circuits. 2004 Edition. 2nd Edition.* Cambridge Univ Pr, 2004.

[98] J. Du, J. Hu, and K. Tseng, "High-power, multioutput piezoelectric transformers operating at the thickness-shear vibration mode," *IEEE Transactions on Ultrasonics, Ferroelectrics and Frequency Control*, vol. 51, no. 5, pp. 502–509, 2004.

[99] J. Dargahi, M. Parameswaran, and S. Payandeh, "A micromachined piezoelectric tactile sensor for an endoscopic grasper-theory, fabrication and experiments," *Journal of Microelectromechanical Systems*, vol. 9, no. 3, pp. 329–335, 2000.

[100] C. F. Klingshirn, B. K. Meyer, A. Waag, A. Hoffmann, and J. M. M. Geurts, *Zinc Oxide*, ser. From Fundamental Properties Towards Novel Applications. Springer Verlag, Aug. 2010.

[101] R. Hanson, "Jmol – a paradigm shift in crystallographic visualization," *Journal of Applied Crystallography*, vol. 43, no. 5, pp. 1250–1260, Oct. 2010.

[102] J. E. Mahan, *Physical vapor deposition of thin films*. Wiley-Interscience, 2000.

[103] P. H. Carr, "Measurement of the Piezoelectric Constant of Quartz at Gigacycle Frequencies," *The Journal of the Acoustical Society of America*, vol. 41, no. 1, p. 75, 1967.

[104] D. Royer and V. Kmetik, "Measurement of piezoelectric constants using an optical heterodyne interferometer," *Electronics Letters*, vol. 28, no. 19, pp. 1828–1830, 1992.

[105] E. Cattan, T. Haccart, and D. Rémiens, "e[sub 31] piezoelectric constant measurement of lead zirconate titanate thin films," *Journal of Applied Physics*, vol. 86, no. 12, p. 7017, 1999.

[106] C. Hammond, *The basics of crystallography and diffraction*, ser. a textbook for materials science. Basics. Oxford University Press, USA, Jun. 2009.

[107] J. Molarius, J. Kaitila, T. Pensala, and M. Ylilammi, "Piezoelectric ZnO films by rf sputtering," *Journal of Materials Science: Materials in Electronics*, 2003.

[108] B. Girault, P. Villain, E. Le Bourhis, P. Goudeau, and P. Renault, "X-ray diffraction analysis of the structure and residual stresses of W/Cu multilayers," *Surface and Coatings Technology*, vol. 201, no. 7, pp. 4372–4376, 2006.

[109] Y. S. Chang and J.-M. Ting, "Characteristics of zinc oxide deposited on copper metallized Si substrates," *Journal of Vacuum Science & Technology A: Vacuum, Surfaces, and Films*, vol. 19, no. 5, p. 2142, 2001.

[110] M. Dubois, J. Carpentier, P. Vincent, C. Billard, G. Parat, C. Muller, P. Ancey, and P. Conti, "Monolithic above-IC resonator technology for integrated architectures in mobile and wireless communication," *Solid-State Circuits, IEEE Journal of*, vol. 41, no. 1, pp. 7–16, 2006.

[111] R. Aigner, "Volume manufacturing of BAW-filters in a CMOS fab," *Acoustic Wave Device Symposium*, pp. 129–134, 2004.

[112] K. Lakin, K. McCarron, and R. Rose, "Solidly mounted resonators and filters," *Ultrasonics Symposium, 1995. Proceedings., 1995 IEEE*, vol. 2, pp. 905–908 vol.2, Oct. 1995.

[113] S. Marksteiner, J. Kaitila, G. Fattinger, and R. Aigner, "Optimization of acoustic mirrors for solidly mounted BAW resonators," *Ultrasonics Symposium, 2005 IEEE*, vol. 1, pp. 329–332, Aug. 2005.

[114] W. Newell, "Face-mounted piezoelectric resonators," *Proceedings of the IEEE*, vol. 53, no. 6, pp. 575–581, Jun. 1965.

[115] A. Ballato, "Bulk and Surface Acoustic Wave Excitation and Network Representation," *28th Annual Symposium on Frequency Control. 1974*, pp. 270–279, 1974.

[116] K. Lakin, G. Kline, and K. McCarron, "Development of miniature filters for wireless applications," *Microwave Theory and Techniques, IEEE Transactions on*, vol. 43, no. 12, Part 2, pp. 2933–2939, Dec. 1995.

[117] S. Salgar, G. Kim, D. Han, and B. Kim, "Modeling and simulation of the thin film bulk acoustic resonator," *Frequency Control Symposium and PDA Exhibition, 2002. IEEE International*, pp. 40–44, 2002.

[118] S. Jose, R. Hueting, and A. Jansman, "Modelling of bulk acoustic wave resonators for microwave filters," *11th Annual Workshop on Semiconductor Advances for Future Electronics and Sensors*, 2008.

[119] D. M. Pozar, *Microwave engineering*. John Wiley & Sons Inc, 1997.

[120] J. Kaitila, M. Ylilammi, J. Ella, and R. Aigner, "Spurious resonance free bulk acoustic wave resonators," *Ultrasonics, 2003 IEEE Symposium on*, vol. 1, pp. 84–87 Vol. 1, 2003.

[121] H. Kanbara, H. Kobayashi, and K. Nakamura, "Analysis of Piezoelectric Thin Film Resonators with Acoustic Quarter-Wave Multilayers," *Japanese Journal of Applied Physics*, vol. 39, no. Part 1, No. 5B, pp. 3049–3053, May 2000.

[122] H. Zhang, M. Marma, E. Kim, C. McKenna, and M. Thompson, "A film bulk acoustic resonator in liquid environments," *Journal of Micromechanics and Microengineering*, vol. 15, p. 1911, 2005.

[123] J. W. Grate, A. Snow, D. S. Ballantine, H. Wohltjen, M. H. Abraham, R. A. McGill, and P. Sasson, "Determination of partition coefficients from surface acoustic wave vapor sensor responses and correlation with gas-liquid chromatographic partition coefficients," *Analytical Chemistry*, vol. 60, no. 9, pp. 869–875, May 1988.

[124] Su, "Thin-film bulk acoustic resonators and filters using ZnO and lead-zirconium-titanate thin films," *Microwave Theory and Techniques, IEEE Transactions on*, vol. 49, no. 4, pp. 769–778, 2001.

[125] A. Arnau, Y. Jiménez, and T. Sogorb, "An extended Butterworth Van Dyke model for quartz crystal microbalance applications in viscoelastic fluid media," *Ultrasonics, Ferroelectrics and Frequency Control, IEEE Transactions on*, vol. 48, no. 5, pp. 1367–1382, 2001.

[126] J. I. Larson, P. Bradley, S. Wartenberg, and R. Ruby, "Modified Butterworth-Van Dyke circuit for FBAR resonators and automated measurement system," *Ultrasonics Symposium, 2000 IEEE*, vol. 1, pp. 863–868, 2000.

[127] A. Arnau, Y. Jiménez, and T. Sogorb, "Thickness-shear mode quartz crystal resonators in viscoelastic fluid media," *Journal of Applied Physics*, vol. 88, p. 4498, 2000.

[128] K. Lakin, G. Kline, R. Ketcham, J. Martin, and K. McCarron, "Stacked crystal filters implemented with thin films," *Frequency Control, 1989., Proceedings of the 43rd Annual Symposium on*, pp. 536–543, 1989.

[129] V. Singh, "Discussion on Barkhausen and Nyquist stability criteria," *Analog Integrated Circuits and Signal Processing*, vol. 62, no. 3, pp. 327–332, Aug. 2009.

[130] ——, "Failure of Barkhausen oscillation building up criterion," *Analog Integrated Circuits and Signal Processing*, vol. 50, pp. 127–132, 2007.

[131] F. He, R. Ribas, C. Lahuec, and M. Jézéquel, "Discussion on the general oscillation startup condition and the Barkhausen criterion," *Analog Integrated Circuits and Signal Processing*, vol. 59, no. 2, pp. 215–221, Dec. 2008.

[132] I. M. Filanovsky, C. J. M. Verhoeven, and M. Reja, "Remarks on Analysis, Design and Amplitude Stability of MOS Colpitts Oscillator," *IEEE Transactions on Circuits and Systems II: Express Briefs*, vol. 54, no. 9, pp. 800–804, 2007.

[133] G. Pierce, "Piezoelectric crystal resonators and crystal oscillators applied to the precision calibration of wavemeters," *Proceedings of the American Academy of Arts and Sciences*, vol. 59, no. 4, pp. 81–106, 1923.

[134] B. Otis and J. Rabaey, "A 300-/spl mu/W 1.9-GHz CMOS oscillator utilizing micromachined resonators," *Solid-State Circuits, IEEE Journal of*, vol. 38, no. 7, pp. 1271–1274, Jul. 2003.

[135] K. Williams, K. Gupta, and M. Wasilik, "Etch rates for micromachining processing-Part II," *Microelectromechanical Systems, Journal of*, vol. 12, no. 6, pp. 761–778, 2003.

[136] A. Vorobiev, J. Berge, S. Gevorgian, M. Löffler, and E. Olsson, "Effect of interface roughness on acoustic loss in tunable thin film bulk acoustic wave resonators," *Journal of Applied Physics*, vol. 110, p. 024116, 2011.

[137] K. Telschow, V. Deason, D. Cottle, and J. Larson III, "Full-field imaging of gigahertz film bulk acoustic resonator motion," *IEEE Transactions on Ultrasonics, Ferroelectrics and Frequency Control*, vol. 50, no. 10, pp. 1279–1285, 2003.

[138] D. Young and B. Boser, "A micromachine-based RF low-noise voltage-controlled oscillator," in *Custom Integrated Circuits Conference, 1997., Proceedings of the IEEE 1997*, 1997, pp. 431–434.

[139] R. Ruby, J. Larson, C. Feng, and S. Fazzio, "The effect of perimeter geometry on FBAR resonator electrical performance," *Microwave Symposium Digest, 2005 IEEE MTT-S International*, 2005.

[140] T. Pensala, T. Makkonen, J. Vartiainen, J. Knuuttila, J. Kaitila, O. Holmgren, and M. M. Salomaa, "2002 IEEE Ultrasonics Symposium, 2002. Proceedings." in *2002 IEEE International Ultrasonics Symposium.* IEEE, 2002, pp. 977–980.

[141] K. M. Lakin, "1993 IEEE International Frequency Control Symposium," in *1993 IEEE International Frequency Control Symposium*. IEEE, 1993, pp. 502–508.

[142] D. Nakamura, Y. Yoshino, Y. Gotoh, T. Nomura, M. Takeuchi, and K. Uesaka, "Piezoelectric resonator, piezoelectric filter, duplexer, communication appartus," Mar. 2005.

[143] D. Leeson, "A simple model of feedback oscillator noise spectrum," *Proceedings of the IEEE*, vol. 54, no. 2, pp. 329–330, Feb. 1966.

[144] T. Lee and A. Hajimiri, "Oscillator phase noise: a tutorial," *Solid-State Circuits, IEEE Journal of*, vol. 35, no. 3, pp. 326–336, 2000.

[145] M. Rinaldi, C. Zuniga, and G. Piazza, "Ss-DNA functionalized array of ALN Contour-Mode NEMS Resonant Sensors with single CMOS multiplexed oscillator for sub-ppb detection of volatile organic chemicals," in *Micro Electro Mechanical Systems (MEMS), 2011 IEEE 24th International Conference on*, 2011, pp. 976–979.

[146] Ohta, "Temperature characteristics of solidly mounted piezoelectric thin film resonators," *Ultrasonics, 2003 IEEE Symposium on*, vol. 2, pp. 2011–2015, 2003.

[147] D. Petit, B. Gautier, D. Albertini, E. Defay, J. Verdier, D. Barbier, and J.-F. Carpentier, "Determination of the temperature coefficient piezoelectric constant TCe33 to improve thermal 1D acoustic tool for BAW resonator design," *Ultrasonics Symposium (IUS), 2009 IEEE International*, pp. 2016–2019, 2009.

[148] J. Bjurström, G. Wingqvist, V. Yantchev, and I. Katardjiev, "Temperature compensation of liquid FBAR sensors," *Journal of Micromechanics and Microengineering*, vol. 17, p. 651, 2007.

[149] K. Lakin, K. McCarron, and J. McDonald, "Temperature compensated bulk acoustic thin film resonators," *Ultrasonics Symposium, 2000 IEEE*, vol. 1, pp. 855–858 vol. 1, 2000.

[150] X. Zhang, W. Xu, and J. Chae, "Temperature effects on a high Q FBAR in liquid," *Sensors & Actuators: A. Physical*, vol. 166, no. 2, pp. 264–268, Apr. 2011.

[151] S. D. Piccot, J. J. Watson, and J. W. Jones, "A Global Inventory of Volatile Organic Compound Emissions From Anthropogenic Sources," *Journal of Geophysical Research*, vol. 97, no. D9, pp. 9897–9912, Jan. 1992.

[152] C. Gray, R. Monson, and N. Fierer, "Emissions of volatile organic compounds during the decomposition of plant litter," *Journal of Geophysical Research*, vol. 115, no. G3, p. G03015, 2010.

[153] K. Schierbaum, A. Hierlemann, and W. Göpel, "Modified polymers for reliable detection of organic solvents: thermodynamically controlled selectivities and sensitivities," *Sensors & Actuators: B. Chemical*, vol. 19, no. 1-3, pp. 448–452, 1994.

[154] W. H. King, "Piezoelectric Sorption Detector." *Analytical Chemistry*, vol. 36, no. 9, pp. 1735–1739, Aug. 1964.

[155] K. Bodenhöfer, A. Hierlemann, G. Noetzel, U. Weimar, and W. Göpel, "Performances of Mass-Sensitive Devices for Gas Sensing: Thickness Shear Mode and Surface Acoustic Wave Transducers," *Analytical Chemistry*, vol. 68, no. 13, pp. 2210–2218, Jan. 1996.

[156] M. Horrillo, M. Fernández, J. Fontecha, I. Sayago, M. Garca, M. Aleixandre, J. Santos, L. Arés, J. Gutiérrez, and I. Gracia, "Detection of volatile organic compounds using surface acoustic wave sensors with different polymer coatings," *Thin Solid Films*, vol. 467, no. 1, pp. 234–238, 2004.

[157] J. W. Grate, "Acoustic Wave Microsensor Arrays for Vapor Sensing," *Chemical Reviews*, vol. 100, no. 7, pp. 2627–2648, Jul. 2000.

[158] W. Carey, K. Beebe, and B. Kowalski, "Multicomponent analysis using an array of piezoelectric crystal sensors," *Analytical Chemistry*, vol. 59, no. 11, pp. 1529–1534, 1987.

[159] P. Si, J. Mortensen, A. Komolov, J. Denborg, and P. Moller, "Polymer coated quartz crystal microbalance sensors for detection of volatile organic compounds in gas mixtures," *Analytica Chimica Acta*, vol. 597, no. 2, pp. 223–230, 2007.

[160] J. W. Grate, S. J. Patrash, S. N. Kaganove, and B. M. Wise, "Hydrogen Bond Acidic Polymers for Surface Acoustic Wave Vapor Sensors and Arrays," *Analytical Chemistry*, vol. 71, no. 5, pp. 1033–1040, Mar. 1999.

[161] T. C. Pearce, S. S. Schiffman, H. T. Nagle, and J. W. Gardner, *Handbook of Machine Olfaction: Electronic Nose Technology*. Wiley-VCH, Mar. 2003.

[162] H. J. McDermott, *Air Monitoring for Toxic Exposures, Second Edition: Including Emergency Response and Terrorism*. Wiley, John & Sons, Incorporated, 2004.

[163] Z. Ying, Y. Jiang, X. Du, G. Xie, J. Yu, and H. Wang, "PVDF coated quartz crystal microbalance sensor for DMMP vapor detection," *Sensors & Actuators: B. Chemical*, vol. 125, no. 1, pp. 167–172, Jul. 2007.

[164] K. Choonee, R. R. A. Syms, M. M. Ahmad, and H. Zou, "Post processing of microstructures by PDMS spray deposition," *Sensors & Actuators: A. Physical*, vol. 155, no. 2, pp. 253–262, Oct. 2009.

[165] E. Castro, E. Gonzo, and J. Gottifredi, "Thermodynamics of the absorption of hydrocarbon vapors in polyethylene films," *Journal of membrane science*, vol. 31, no. 2-3, pp. 235–248, 1987.

[166] J. Chang, "A new technique for beveling the tips of glass capillary micropipettes and microelectrodes," *Comparative Biochemistry and Physiology Part A: Physiology*, vol. 52, no. 3, pp. 567–570, 1975.

[167] J. H. Koschwanez, R. H. Carlson, and D. R. Meldrum, "Thin PDMS Films Using Long Spin Times or Tert-Butyl Alcohol as a Solvent," *PLoS ONE*, vol. 4, no. 2, p. e4572, Feb. 2009.

[168] W. Pang, R. Ruby, R. Parker, P. Fisher, M. Unkrich, and J. Larson, "A Temperature-Stable Film Bulk Acoustic Wave Oscillator," *Electron Device Letters, IEEE*, vol. 29, no. 4, pp. 315–318, 2008.

[169] A. Rahtu and M. Ritala, "Compensation of temperature effects in quartz crystal microbalance measurements," *Applied Physics Letters*, vol. 80, no. 3, p. 521, 2002.

[170] Z. Li, Y. Jones, J. Hossenlopp, R. Cernosek, and F. Josse, "Design considerations for high sensitivity guided SH-SAW chemical sensor for detection in aqueous environments," in *Frequency Control Symposium and Exposition, 2004. Proceedings of the 2004 IEEE International*, 2004, pp. 185–192.

[171] S. Rey-Mermet, R. Lanz, and P. Muralt, "Bulk acoustic wave resonator operating at 8GHz for gravimetric sensing of organic films," *Sensors & Actuators: B. Chemical*, vol. 114, no. 2, pp. 681–686, Apr. 2006.

[172] D. W. Allan, "Time and Frequency (Time-Domain) Characterization, Estimation, and Prediction of Precision Clocks and Oscillators," *IEEE Transactions on Ultrasonics, Ferroelectrics and Frequency Control*, vol. 34, no. 6, pp. 647–654, Nov. 1987.

[173] D. Allan, "A method for estimating the frequency stability of an individual oscillator," *Proc 8th Ann Symp on Frequency Control*, 1974.

[174] T. Schneider, G. Frye-Mason, S. Martin, J. Spates, T. Bohuszewicz, G. Osbourn, and J. Bartholomew, "Chemically selective coated quartz-crystal-microbalance (QCM) array for detection of volatile organic chemicals," *Proceedings of SPIE*, vol. 3539, p. 85, 1998.

[175] M. Rinaldi, C. Zuniga, B. Duick, and G. Piazza, "Use of a single multiplexed CMOS oscillator as direct frequency read-out for an array of eight AlN Contour-Mode NEMS Resonant Sensors," *Sensors, 2010 IEEE*, pp. 2666–2670, 2010.

[176] M. Link, M. Schreiter, J. Weber, R. Gabl, D. Pitzer, R. Primig, W. Wersing, M. Assouar, and O. Elmazria, "c-axis inclined ZnO films for shear-wave transducers deposited by reactive sputtering using an additional blind," *Journal of Vacuum Science & Technology A: Vacuum, Surfaces, and Films*, vol. 24, p. 218, 2006.

[177] Y. Yoshino, M. Takeuchi, K. Inoue, T. Makino, S. Arai, and T. Hata, "Control of temperature coefficient of frequency in zinc oxide thin film bulk acoustic wave resonators at various frequency ranges," *Vacuum*, vol. 66, no. 3-4, pp. 467–472, 2002.